No. 2 of 10

FINAL REPORT ON PROJECT

"Fatigue Crack Initiation and Propagation in Steels Exposed to Inert and Corrosive Environments"

Worked performed at the University of California, Berkeley, and Lawrence Livermore Laboratory, Purchase Order No. 2801103 during the period 5/1/77 to 12/31/77

by

K. Youseffi
I. Finnie

Berkeley Feb. 1978

Fatigue Crack Initiation and Propagation in Steels Exposed to Inert and Corrosive Environments

ABSTRACT

The useful life of structural components subjected to cyclic loads is limited by fatigue. In general, a fatigue failure involves three phases; crack initiation, crack propagation, and final failure. Most investigations of fatigue have been confined to either the initiation or the propagation aspects of the problem. However, for accurate predictions of life, methods are needed for predicting both the number of cycles to initiate a crack as well as the number of cycles to propagate it to some critical length.

In the present study, the fatigue crack initiation life of AISI 1018 steel was investigated using compact tension specimens having sharp notch root radii. The data were analyzed using two methods for predicting initiation in strain cycling experiments. Also, another approach in which initiation is related to the stress intensity factor was developed. The results showed that the number of cycles to initiate a crack from a notched component can be predicted quite accurately. The results also showed that the number

of cycles required to initiate a fatigue crack, N_i, is related to the stress intensity factor range, ΔK, and the notch radius, ρ, by a power law, $N_i = \beta(\Delta K/\sqrt{\rho})^{-\alpha}$. Expressions were obtained to estimate the material constants β and α from the yield strength of a steel.

The next phase, that of propagation, was studied using AISI 1018 steel and a new high strength steel HY-180. The crack propagation data obtained for both steels tested in air can be described accurately by the power law first suggested by Paris, $da/dN = C(\Delta K)^n$, where a is the crack length, N the number of cycles, and C and n are material constants. However, the exponent n was found to be two times larger for AISI 1018 steel than HY-180 steel. This was later attributed to the lower fracture toughness associated with AISI 1018 steel. It was interesting to observe that the crack propagation rate of the low yield strength 1018 steel was lower than that of HY-180 steel for ΔK values less than 30 ksi-in$^{\frac{1}{2}}$. At the test temperature of 185°F, the crack propagation rate of AISI 1018 steel decreased significantly compared to room temperature values. These observations indicate that one should be cautious in using the common generalization that crack propagation data (da/dN versus ΔK) for all steels fall in a narrow band. It appears that this generalization will only apply to steels with plane-strain fracture toughness values (K_{Ic}) greater than 50-60

ksi-in$^{\frac{1}{2}}$.

The effects of cyclic frequency and mean stress on crack propagation rate were negligible for all tests carried out in air.

In order to design marine structures, an understanding of the fatigue behavior of steels in a corrosive environment (salt water) is needed. Therefore, in this investigation the fatigue crack propagation behavior of AISI 1018 and HY-180 steels in 3% NaCl solution was studied. The investigation included the influence of cyclic load frequency and applied mean stress on the crack propagation rate. In general, the crack propagation rate in salt water was found to be higher than that in air with the increase depending on the cyclic frequency and the applied mean stress. As the frequency increased, the effect of the salt water on the crack propagation rate decreased. Also, as the mean stress increased, so did the crack propagation rate.

Cathodic protection is a traditional procedure for corrosion protection of steel structures in salt water. In some cases, it restores the fatigue crack initiation properties in salt water to the values found in air and this assumption is made by many designers. In the present work the influence of cathodic protection on crack propagation rate was studied for the two steels. Test results showed an adverse effect of cathodic protection on crack propagation rate. It

is concluded that a high negative potential can cause significant increase in crack propagation rate. Hence, the minimum potential adequate for corrosion protection is desirable if fatigue crack propagation is a design consideration.

TABLE OF CONTENTS

I - INTRODUCTION

Fatigue can be defined as progressive failure of a component under cyclic stresses or strains. Failure occurs even when the applied stress or strain is well below the value corresponding to failure under monotonic loading. Since most engineering structures are exposed to fluctuating loads, fatigue is the largest single source of failure of metals in service. Fatigue failure can be divided into three stages - 1) crack initiation, 2) crack propagation, and 3) final failure. Many mechanisms have been proposed to describe fatigue crack initiation and these are reviewed in Chapter II.

A major motivation for the study of fatigue came in the mid-nineteenth century when railway axles in Europe failed during service. As early as 1860, Wöhler in Germany and Fairbairn in Britain had conducted extensive laboratory experiments and presented their results as graphs of applied stress (S) vs. number of cycles to failure (N). Their S-N curves were obtained by loading rotating bar specimens with a fixed moment (rotating bending). Ever since, similar S-N curves have been used to design parts to avoid fatigue failures. This traditional approach involves applications,

such as axles, where many millions of load cycles may be imposed. By contrast in recent years for applications such as nuclear reactors and pressure vessels, "low-cycle" fatigue has become of interest. Work on both high and low-cycle fatigue is reviewed in Chapter III. An essential point, which is often overlooked, is that these fatigue studies are concerned with crack initiation. In high-cycle fatigue testing of smooth parts the crack initiation process consumes the vast majority of life. In low-cycle fatigue, failure is usually defined as the initiation of a crack of a prescribed length.

The crack initiation approach to fatigue design becomes increasingly unrealistic when the majority of life is spent in propagating rather than initiating a crack. This is true, for example, in notched members. Although smooth bar crack initiation data are used conventionally to predict the life of notched members by incorporating a variety of correction factors, such an approach can only be empirical. In situations such as large field-welded structures which inevitably contain initial flaws or cracks the initiation aspects of fatigue are of little interest and life is determined by the rate of crack propagation. For this reason, in recent years many investigators have focused their attention on fatigue crack propagation rather than the crack initiation phase. Many empirical laws have been proposed to relate crack

growth rates to stress levels and crack lengths. The development of linear elastic fracture mechanics helped greatly in understanding and unifying these propagation laws. In this approach, the crack growth rate is related to the stress intensity factor which, in turn, depends on the applied loading, the crack length, and the geometry of the part. The stress analysis aspects of crack propagation are reviewed at the end of Chapter III and a detailed treatment of this topic is given in Chapter IV.

In many cases, it is difficult to avoid some form of stress raisers (notches) in designing a component. Therefore both fatigue initiation and propagation lives should be considered ideally when a component with a notch is designed against fatigue failure. As it stands now, the classical S-N curve approach gives no information about the crack propagation behavior of a material. On the other hand, crack propagation laws do not include any information about crack initiation. Since different material properties are of importance in the high-cycle and low-cycle ranges for crack initiation while completely different properties govern crack propagation, a unified approach to design against fatigue presents major problems.

With this motivation, in the present work, a series of tests was made on sharply notched steel specimens to measure both the initiation and propagation stages of fatigue.

Another factor which may strongly influence fatigue behavior is the presence of a corrosive environment. The one that arises the most often in practice is that which covers nearly three-quarters of the earth's surface - salt water. Initiation and propagation of fatigue cracks can both be influenced by salt water. A common technique to control corrosion in salt water is cathodic protection. However, the influence of this variable on fatigue has been inadequately studied. Particularly for the crack propagation stage, conflicting results have been reported in the literature. With this in mind a series of tests was made to study the effect of salt water and of cathodic protection on the crack propagation rate in two steels. The experimental variables include the effect of the ratio R of minimum to maximum load and the frequency of loading.

Two widely different steels were selected for the experiments. One is a conventional low carbon (1018) steel with a yield strength of about 40,000 psi. The other is the recently developed HY-180 steel with a yield strength of about 180,000 psi. This material has a high fracture toughness as well as a high yield strength and is known to be less susceptible to degradation of fracture toughness in salt water than other high strength steels - such as maraging steels. In this sense, the two steels represent the ordinary and the optimum available at the present time. The

experimental work is described in Chapter V.

As in other areas of mechanical behavior, in fatigue we try to predict behavior based on simple tests such as uniaxial tension and empirical correlations. Several different approaches are discussed for crack initiation and compared with experimental results in Chapter VI. For crack propagation some generalizations can be offered. However, from the present work it appears that too simplified a picture has been presented in the literature for crack propagation. At the present time it seems desirable to obtain crack propagation data for the material of interest for the environment and cyclic loading speeed expected in practice. This work is also treated in Chapter VI which concludes with a discussion of some of the problems of combining initiation and propagation into a single model. Some possible approaches to this problem are presented.

Finally Chapter VII summarizes the present work and attempts to draw some general conclusions for the design of steel members against fatigue in a corrosive environment.

II - FATIGUE CRACK INITIATION

Fatigue failure of materials is basically divided into three stages: a) crack nucleation, b) crack propagation, and c) final failure. In this chapter, fatigue crack nucleation in inert and aggressive environments will be discussed.

A - Mechanisms of Fatigue Crack Nucleation

With few exceptions, in high-cycle life testing fatigue cracks nucleate at the surface. However, when a strong surface film is present cracks tend to nucleate at subsurface flaws of unusual severity. In instances where subsurface crack nucleation was observed the life of the part was still governed by cracks that originated at the surface (1).

1 - The Persistent Slip Band

Slip occurring in a plastically deformed grain having a free surface results in surface steps of varying height which, if the surface is suitably prepared metallurgically, are visible as lines when viewed under a microscope.

Slip-line development on the surface of a fatigue specimen has been studied by many investigators. As early

as 1903, Ewing and Humphrey (2) tested iron specimens in rotating bending at stress levels above the endurance limit. The test was stopped frequently to examine the surface of the specimens. At the early stages of the test they observed few slip lines but, as the experiment proceeded, new slip lines formed close to existing ones producing bands of slip. These bands grew wider and more dense as the test proceeded. About fifty years later, Thompson, Wadsworth, and Louat (3) tested high-purity copper specimens in alternating stress with zero mean. They also removed the specimens periodically and examined them. Slip bands formed early in the test and became more numerous as the test progressed. The roughness associated with slip bands was removed periodically by electropolishing and most of the slip bands disappeared. However, a few of the slip bands became accentuated and were called "persistent slip bands" and fatigue cracks grew eventually from these bands. The persistent slip bands most often start at grain boundaries and develop in a transgranular manner as shown in Figure 2.1.

2 - The Formation of Intrusions and Extrusions

Many slip mechanisms have been proposed to explain the occurrence of intrusions and extrusions on the surface of a material. Some of these mechanisms will be discussed briefly here.

All of the crack nucleation mechanisms described below require some localized plastic deformation. Mott (4) proposed a slip mechanism that requires for its operation a screw dislocation terminating in the surface at one end. This process is shown schematically in Figure 2.2. Under cyclic loading, the screw dislocation AA' completes a closed circuit by cross slipping from one plane to another, extruding the material within the circuit by one Burgers vector in each cycle. In this mechanism it is not easy to see why the dislocation does not simply oscillate back and forth. To overcome this criticism, Kennedy (5) proposed what he called a "gating" mechanism (Figure 2.3). In this model, a group of screw dislocations glide on a plane intersected by another plane containing a similar group of edge dislocations. The force resulting from the intersection of dislocations is such that the edge dislocations and the associated Lomer-Cottrell barrier are moved out of the path of the screw dislocations, so that they glide past. In the negative half cycle of stress, edge dislocations of opposite signs are generated, the Lomer-Cottrell barrier is translated into the path of negative screw dislocations, and the screw dislocations then cross slip to avoid the barrier, thus providing the essential elements for extrusion-intrusion formation. This model allows for the large number of dislocations required to form extrusions and intrusions as fast as they are observed. Kennedy suggests that it is

not necessary that the same dislocations should go around a closed path, but merely that there should exist path discrimination between positive and negative dislocation. Another attractive feature about this model is that it does not require internal voids as does Mott's model.

Another mechanism proposed is by Cottrell and Hull (6). They suggested a simple duplex slip mechanism involving sequential slipping from two sources S1 and S2 shown in Figure 2.4. It results in a large separation of the intrusion and extrusion. This mechanism was later discounted since it could not explain the formation of extrusion-intrusion pairs when only one family of slip planes is operating.

The intrusion-extrusion model by McEvily and Machlin (7) involves two screw dislocations terminating in the surface (Figure 2.5) with a subsurface node where dislocations meet. Under a cyclic stress, the screw dislocation pair is shifted around a circuit, if cross slip is possible, and a collinear extrusion-intrusion pair forms in the slip band. This model does not account for the observed rapid formation of extrusions.

Thompson (8) suggests yet another extrusion-intrusion model. This mechanism depends on the simple traverse of edge dislocations across slip planes penetrated by screw dislocations (Figure 2.6). During the tension part of the cycle, the edge dislocations interact with the forest

dislocations causing a slip step. If, in the compressive part of the cycle, edge dislocations of opposite sign executed the same motion with the forest dislocations in the same position, the slip step would unslip and the original surface would be restored. However, if the forest dislocations move, and there is a good chance that they would, exact unslipping would not happen and extrusion and intrusion would form. This model seems to be most realistic for wavy slip materials; it could be expected to operate at both high and low strains, and also at grain boundaries.

3 - Low Strain, Long Life Crack Nucleation

The intrusion-extrusion mechanisms described in the preceding section could be taken as the crack nucleation mechanisms. But, intrusion-extrusion formation is not the only mechanism for initiation. It seems that persistent slip bands are more important since intrusion and extrusion depend on persistent slip bands. Therefore, a more general mechanism of crack nucleation based on persistent slip bands is needed. Again there have been a number of proposals and some of them will be discussed briefly.

Vacancies can coalesce to form voids thus nucleating a crack. It is well known that fatigue cycling produces dislocation interactions which in turn create vacancies. This void mechanism can be criticized since it could hardly take place at low or ambient temperatures because the process

depends on diffusion. However, at high temperatures, where creep phenomena begin to play a role, a fatigue crack nucleation mechanism based on vacancy condensation may be valid.

Fujita (9) showed theoretically that it might be possible for dislocation dipoles to nucleate cracks. Therefore, it is reasonable to suggest that the accumulation of defects may destroy crystal coherency across a slip plane and lead to cracking. Grosskreutz (10) observed that in aluminum, under low amplitude cycling, large numbers of dipoles accumulated near the surface where they tend to be stranded because of the weak dipole-surface interaction (11). It was then concluded that such an accumulation of edge dislocation dipoles might form a crack nucleus.

Wood (12) proposed a mechanism based on the fact that if forward and reverse stressing result in different amounts of net slip on different planes, then a general roughening of the surface would occur. Therefore, the valleys formed in such a manner act as stress raisers and promote further slip. This mechanism was criticized by Kennedy (5), since under cyclic stress it is not clear why the slip should continue to deepen the valley. Later on, May (13) developed a statistical formulation showing that, with continued cycling, progressively deeper valleys would result from random slip.

Neuman (14) proposed a model in which cracks are formed by coarse slip on alternating parallel slip planes. He states that when crack initiation develops from a coarse slip step produced in tension (Figure 2.7), excess dislocations of one sign remain on the activated slip plane 1 shown in Figure 2.7. On compression, the situation in (a) is reversed to a compressive slip step. The two dashed lines in (a) represent the planes through the root of the step with maximum shear stress. So, if the stress is high enough a second glide system 2 will be activated with results shown in (b). At each step the height of the step is limited by the work hardening of the activated slip plane. During the next compression, the excess dislocations on 1 and 2 run back causing configuration (c), essentially a crack nucleus, and the matrix of the surfaces at A hinders slip so that no compressive slip steps are formed. It is reasonable to expect that the surfaces at A can be separated again without effort. In the next tension stage, slip is also activated on the unhardened plane 3, and the process of forming a new increment of crack surface is repeated until a substantial microcrack is produced.

4 - High Strain Crack Nucleation

In the presence of high strain, crack initiation mechanisms differ from what was discussed in Section 3. Wood and Bendler (15) investigated the surface damage in

copper and observed that the "notch and peak" effects associated with long life fatigue did not develop in the high strain range. This was later confirmed by Kemsley (16) who found that persistent slip bands did not occur at high stresses.

Most investigators (16,17) found that the cracks mainly nucleated at grain boundaries. It seems that grain boundary nucleation takes place in the absence of any inherent grain boundary weakness. This mechanism appears to be purely geometrical. In high strain fatigue the surface becomes severely rumpled and the surface displacements are large. The constraints at grain boundaries cause mid-grain areas to bulge outwards during the compression part of the cycle and this process forms a notch. Laird (18) has also shown theoretically that the degree of plastic folding could increase as the grain size of the material increases. Pure aluminum specimens were tested and it was found that the number of cycles to nucleate a crack increased as the grain size decreased.

The fact still remains that due to the complicated nature of fatigue crack initiation, it is hard to make a definite statement on a mechanism that describes the initiation process for all materials. But it appears that most of the observations point to Wood or Neuman type mechanisms.

B - Role of Aqueous Environment in Crack Initiation

Aqueous environments are known to influence the fatigue crack nucleation process. The theories pertaining to the role of aqueous environment in the nucleation process will be discussed in this section.

1 - Protective Film Destruction

The most common film observed on metal surface is an oxide film. The thickness of the oxide film is usually greater than 10Å. Aluminum, when exposed to dry air, obtains an oxide film of thickness 100Å as compared to stainless steel value of 10-20Å. This oxide film is cathodic to the metal matrix. Some investigators have suggested that the fatigue slip steps break through this oxide film, thus exposing small anodic regions to the large cathodic film (Figure 2.8). This results in electrochemical cells which in turn cause a rapid dissolution of the metal in the vicinity of the emerging slip step and prematurely initiate fatigue cracking. This mechanism was proposed as early as 1933 (19). It was also shown that lowering the frequency would increase the initiation period presumably because lowering the frequency would allow the oxide film to repair itself and reduce anodic dissolution of newly emerging metal. Simnad and Evans (20) agreed that a mechanism such as described above could take place, but they pointed out that in acid solutions, where oxide films are soluble, a

mechanism of this type can not be accepted. Therefore, it can be concluded that even when an oxide film is present, either the cyclic stresses are not high enough to rupture the cathodic film or the stresses happen at a low enough rate so that film repair occurs more rapidly than does significant corrosion damage due to the formation of electrochemical cells.

2 - Pitting

The mechanism of pit formation is not well understood. Most of the proposed mechanisms suggest either an activated ion, such as chloride, penetrating the passive film and destroying it locally (21) or the activating ion being preferentially absorbed at the metal solution interface displacing the absorbed passive layer and thus destroying passivity (22). But once these pits are formed they act as local electrochemical cells. The bottom of the pit is the anode and the surrounding walls of the pit and the surface of the metal are the cathode. The high ratio of cathodic to anodic area contributes to the high rate of pit growth. McAdam (23) suggested that corrosion-induced pits on the surface act as stress concentrators and reduce the fatigue life of a metal.

It is true that pit formation does lead to reduction of fatigue life. However, it should be mentioned that the corrosion fatigue phenomenon also occurs in environments where

pitting does not occur. This was shown by Simnad and Evans (24) and also confirmed by Duquette and Uhlig (25). They tested low carbon steel in the presence of acid solution and no pits were observed. Conversely, fatigue tests performed in 3% NaCl + NaOH solution of pH12, where only a few randomly distributed pits were observed, showed fatigue limits identical to those found in air.

The results of this nature are not altogether unexpected since corrosion-induced pits tend to be hemispherical and the stress concentration factor associated with surface-connected hemispherical defects is not large (26). It is possible that pits observed at failure are not the cause of corrosion fatigue but rather the result. That is, corrosion fatigue cracks are initiated and are then extended by the corrosive environment to produce evidence of pits.

3 - Preferential Dissolution of Deformation-Induced Anodic Material

The deformed areas in metals and alloys, areas of intense slip, are anodic to undeformed areas. Investigators suggest that cyclic deformation of alloys induces slip band precipitation of impurities which then increase electrochemical reactivity (27). To support this deformed-undeformed metal galvanic couple theory, many observers have shown a shift in electrochemical corrosion potentials in the active direction during early stages of corrosion fatigue tests.

Simnad and Evans (20) have related this potential shift with one or more of three possibilities (Figure 2.9): (a) depolarization of cathodic and anodic areas, anodic depolarization being more dominant; (b) a reduction in resistance of the electrolyte path between local anodes and cathodes; and (c) a shift of the open circuit potential of local anodic areas in the active direction due to the energy increase of plastic deformation.

Duquette and Uhlig (25), in order to examine the effect of dynamically imposed deformation on corrosion behavior, applied cathodic potentials to low carbon steel specimens under high cycle fatigue tests. In both neutral solution and acid solutions of pH 2, 3, 4, polarization of the steel to its calculated open circuit potential resulted in obtaining the fatigue curve determined in air. This is a contradiction to the mechanism proposed by Evans and Simnad. If deformed metal in fatigue generated slip bands were more anodic than undeformed metal, a more active cathodic potential would have to be applied in order to prevent environment-induced crack initiation. This also points towards the fact that cathodic protection may be used to increase the crack initiation life in corrosive environment.

It seems that the effect of plastic deformation on corrosion behavior of metals is still a poorly understood subject.

4 - Surface Energy Reduction by Absorbing Species in the Aqueous Environment

Corrosive environment (liquids), absorbing on solids, may lower the surface energy and therefore favor slip step formation. This mechanism was proposed by Rebinder and co-workers (28). They found that surface active compounds caused the reduction of resolved shear stress of several metals, and also caused the reduction of the fatigue life of steel. Benedicks (29) also arrived at the same conclusion. He suggested that the wetting of metal surfaces by liquid environments could be responsible for some of the environment sensitive mechanical properties, such as corrosion fatigue, the reduction in surface energy of the metal leading to a dilation of surface atomic bonds thus facilitating the slip process. He also stated in his paper that the effect should increase with decreasing surface tension of the liquid.

C - Role of Gaseous Environments in Crack Nucleation

It appears that the opinion of investigators on the effect of gaseous environments on fatigue crack initiation is divided into two opposing points of view. Some suggest that the gaseous environments play no role in crack initiation and others propose that the gaseous environment has a strong effect on the nucleation process.

Thompson (30) suggested that slip bands produced in cyclic fatigue in air become regions of high oxygen concentration due to strain induced vacancy generation. Dissolved oxygen then serves to prevent the rewelding of developing cracks and speeds up the transition from slip band to microcrack (Figure 2.10).

Shen and co-workers (31) expressed the opinion that the surface of a metal cyclically stressed in air is strengthened with an oxide film. Therefore, dislocations are accumulated in surface regions and the formation of voids and cavities is enhanced, leading to premature crack formation (Figure 2.11).

It has also been shown that water vapor is important in the nucleation process in age hardened aluminum alloys. The water vapor either dissociates to form hydrogen which embrittles the alloy and causes early cracking or accelerates the oxidation of emerging slip steps thus blocking reverse slip (32,33).

Some investigators disagree that gaseous environments affect the crack nucleation process. Wadsworth and Hutchings (34) showed that the appearance of microcracks, intrusions and extrusions was similar in air and in vacuum for the same number of cycles. Hordon (35), testing fatigue behavior of aluminum in vacuum, also suggested that not only initiation, but the very early stage of propagation is

unaffected by environment. He then states that the absorption of oxygen at the tip of a growing crack increases the propagation rate and thus decreases fatigue life.

It seems that more critical experiments are needed to understand the effect of gaseous environments on fatigue crack nucleation. However, from available data, the effect of gaseous environments (if any) on crack initiation is very small compared to the effect on crack propagation.

D - Remarks

It has become evident from experimental observations discussed in this section that no one mechanism either in the presence or absence of corrosive environment can explain the crack nucleation process. This is mainly true because the initiation process does not occur by the same mechanism for different materials. On the other hand, it could be stated with some degree of certainty, that fatigue failure in many alloys usually nucleates at some weakly constrained interface or because of stress concentration associated with discontinuities in the structure. And also at high applied stresses, fatigue crack initiation occurs at grain boundaries by means of the plastic folding process.

It can also be concluded that aqueous environments have a more drastic effect on crack initiation than gaseous

environments. Therefore, it appears that the exact mechanism of fatigue crack nucleation in the presence or absence of corrosive environments remains unknown and more elaborate experiments are required before a satisfactory model can be developed. Thus, for the present we still have to rely on experimental results to evaluate the fatigue crack initiation and propagation behavior of a given material in inert or corrosive environments.

III - STRESS ANALYSIS ASPECTS OF FATIGUE

A - Classical Fatigue

1 - S-N Curve

Wöhler (36), between 1858 and 1870, carried out the first comprehensive investigation of the fatigue of metals and ever since his S-N curves have been the major representation of fatigue data. S denotes the stress amplitude or the maximum cycle stress and N denotes the number of stress cycles needed for a complete fracture.

The most widely used fatigue testing machine is the Moore high speed rotating beam machine which subjects the specimen to pure bending by means of weights. The standard specimen used is shown in Figure 3.1. The specimen is carefully machined and polished in an axial direction to avoid circumferential scratches. The outer surface of the specimen is subjected to an alternating stress $\sigma_a = \pm \frac{MC}{I}$ where M is the bending moment, C is the radius and I is the section modulus ($\frac{\pi r^4}{4}$). The number of cycles to failure at a particular stress is recorded. This information is then plotted on log-log paper as shown in Figure 3.2. The ordinate of the S-N curve is called the fatigue strength corresponding

to the number of cycles needed for failure. In the case of steel (in the absence of corrosion or localized loading) this curve becomes horizontal indicating that failure does not occur if the applied stress is below this value. The strength represented by the horizontal line is called the fatigue limit or endurance limit (S_e). It is interesting to note that an endurance limit may not exist for nonferrous metals and alloys.

Several attempts have been made to find a mathematical model for the S-N curve. Weibull (37) proposed an equation in the form of

$$(S - S_e)(N + B)^a = b \tag{3.1}$$

where S_e is the endurance limit and a, b and B are constants. Valluri (38) has also proposed an equation:

$$N = -\frac{2 \ln(\sigma_u/\sigma) \ln[(\sigma-\sigma_i)/k]}{c\,[(\sigma-\sigma_i)/E]^2\,[(\sigma-\sigma')/\sigma_i]^2} \tag{3.2}$$

where σ and σ' are maximum and minimum cyclic stress respectively, σ_u is ultimate tensile strength, σ_i is approximately equal to the endurance limit, and k and c are material constants.

In the case of steel it has been shown that the S-N curve on log-log paper is a straight line between 10^3 and 10^6 cycles. And from experimental data it has been observed that the endurance limit S_e' coincides with 10^6 cycle strength and its value is about $.5S_u$ (for polished specimens). The 10^3 cycle strength is seen to be approximately $.9S_u$. Therefore, from observations one can obtain an equation for the straight line and solve for S_N, the strength for N cycles.

$$S_N = S_e\left(\frac{N}{10^6}\right)^{\frac{1}{3}\log(S_e/.9S_u)} \qquad \text{for } 10^3 < N < 10^6 \qquad (3.3)$$

From a great number of rotating-beam test results it has become more or less standard practice, when test results are not available, to estimate the endurance limit for steels as

$S_e' = .5S_u$ for $S_u \leq 200{,}000$ psi

$S_e' = 100{,}000$ psi for $S_u \geq 200{,}000$ psi

This estimation is different for other materials. For example, $S_e' = .4S_u$ for cast iron but for aluminum and magnesium alloys S_e' is equal to $.3S_u$ to $.4S_u$ based on 10^8 or 5×10^8 cycles. Titanium and titanium alloys tend to show a true endurance limit in the range of 10^6 to 10^7 cycles, S_e' is usually equal to .45 to .65 of the ultimate strength.

? - Endurance Limit Modifying Factors

The endurance limit (S_e') found as a result of tests using a standard specimen and rotating-beam machine may be considerably bigger than the endurance limit of an actual part. There are many reasons for this difference. For example, several points of stress concentration may exist, the operating temperature may be high, or the surface may not have been polished. Therefore, the endurance limit S_e' has to be modified to account for these factors. So:

$$S_e = k_a k_b k_c k_d k_e k_i S_e' \tag{3.4}$$

where

S_e = endurance limit of part

S_e' = endurance limit of standard specimen

k_a = surface factor

k_b = size factor

k_c = reliability factor

k_d = temperature factor

k_e = modifying factor for stress concentration

k_i = miscellaneous effects factor

The surface finish, at least for steel, has been shown to have a significant effect on the endurance limit. Figure 3.3 shows a plot of k_a vs. tensile strength for steels. The data gathered are for hot-rolled and as-forged parts. The surface factor for magnesium and aluminum alloys can be

taken as unity since the endurance limits given by manufacturers include the effect of the surface finish.

Experimental data show a reduction in fatigue endurance limit for larger diameter parts. The rule-of-thumb to follow for steel is

$$k_b \equiv \begin{cases} 1 & \text{for } d \leq .3" \\ .85 & \text{for } .3" < d \leq 2" \\ .75 & \text{for } d > 2" \end{cases}$$

k_b may be taken as unity for completely reversed axial loading.

The endurance limit should also be modified by the reliability factor k_c. When many specimens are tested at several stress levels, the points will scatter in a band. The S-N curve is usually drawn as the mean curve which represents a 50 per cent probability of survival. k_c is taken as unity for 50 per cent survival rate. It is possible to achieve a greater survival rate at a somewhat lower stress level by introducing the k_c factor. Stulen et al (39) propose that the distribution of fatigue strength is normal for a fixed number of cycles and furthermore that the standard deviation is 8 per cent of the endurance limit when test values are not available. Table 3.1 shows tabulated values of k_c for different survival rates. It is important to note here that individual cases should be analyzed carefully in order to select the proper survival rate.

In general, as temperature increases the fatigue strength of a part decreases. The temperature factor k_d is equal to unity for room temperature. For higher temperatures when creep phenomenon also play a role in failure, experimental data should be used to obtain k_d.

A measure of severity of stress concentration is given by the stress concentration factor K_t, which is defined as the ratio of the maximum stress at a discontinuity to the nominal stress. K_t values for different shapes are given in the literature in the form of tables and charts (40). Although fatigue strength is considerably reduced by the geometrical stress concentration factor (K_t), the reduction is often less than the stress concentration factor. For this reason a fatigue stress concentration factor K_f is introduced. K_f is defined as the ratio of the fatigue strength of a notch-free specimen to the fatigue strength of a notched specimen. K_t and K_f are related by the notch sensitivity factor q, which was first defined by Peterson (40):

$$q = \frac{K_f - 1}{K_t - 1}$$

Therefore, the fatigue stress concentration factor is

$$K_f = 1 + q(K_t - 1) \qquad (3.5)$$

and the modifying factor for stress concentration is

$$k_e = \frac{1}{K_f}$$

Figure 3.4 shows the values of q for given notch radius and tensile strength of a material.

The miscellaneous factor k_i is introduced to account for other factors that effect the fatigue strength of a material. These factors include corrosion, residual stresses, surface treatment (case hardening or plating), internal defects (inclusions), among others. The effect of these factors on fatigue strength is usually determined experimentally.

3 - Mean Stress Effect on Fatigue Life

The stresses produced in the laboratory for fatigue study usually vary sinusoidal about a zero mean stress. The stresses are usually expressed in terms of a pair of variables, such as the mean stress σ_m and the alternating or stress amplitude σ_a, as shown in Figure 3.5. From Figure 3.5 we can write

$$\sigma_m = \frac{\sigma_{max} + \sigma_{min}}{2}$$

$$\sigma_a = \frac{\sigma_{max} - \sigma_{min}}{2}$$

The values of σ_a and σ_m corresponding to failure are denoted by S_a and S_m. The value of S_a corresponding to endurance is denoted by S_e, and often the notation S_N is used interchangably with S_a to denote failure in N cycles. Numerous curves of S_m vs. S_a have been proposed to predict fatigue life when both S_m and S_a are varied. The three common curves are shown in Figure 3.6. The straight line joining the alternating fatigue strength to the tensile strength is the modified Goodman law. Goodman's original law included the assumption that the alternating fatigue limit was equal to one-third of the tensile strength which has since been modified. Gerber observed that the experimental data obtained by Wöhler fitted closely to a parabolic relation and this is known as Gerber's parabola. The third relation, known as Soderberg's law, is given by a straight line from the alternating fatigue strength to the static yield strength. Soderberg's line is a very conservative approximation and is not recommended for general use. The modified Goodman diagram is most widely used in the United States and elsewhere. The relationships may be written mathematically as follows:

$$\text{Modified Goodman Law} \qquad \sigma_a = S_e\left(1 - \frac{\sigma_m}{S_u}\right)$$

$$\text{Gerber's Law} \qquad \sigma_a = S_e\left(1 - \left(\frac{\sigma_m}{S_u}\right)^2\right) \tag{3.6}$$

$$\text{Soderberg's Law} \qquad \sigma_a = S_e\left(1 - \frac{\sigma_m}{S_y}\right)$$

where σ_a and σ_m are alternating and mean stress respectively, S_u the tensile strength, S_y the yield strength and S_e the endurance limit.

The curves described above are for a tensile mean stress. One might expect same strengthing for compressive mean stresses. However, it is usually assumed based on data such as shown in Figure 3.7 that mean compressive stress has no effect on the endurance limit. Therefore for design purposes, it is recommended that line AF in Figure 3.7 be used. One can combine Figures 3.6 and 3.7 and also include a factor of safety on the strength properties to obtain the design diagram shown in Figure 3.8.

It was not the purpose of this section to cover the entire classical fatigue approach, but to describe briefly the "backbone" of classical fatigue. No attempt was made to describe many complicated subjects related to this approach. For example, in the case of combined loading where both torsion and bending or tension stresses fluctuate, the failure

criterion becomes different and more complicated. Or, in structures, most often a random loading is encountered instead of sinusoidal loading. Many accumulative fatigue damage rules have been proposed to deal with this situation (41,42).

B - Low Cycle Fatigue

The S-N curve may be divided into two portions, the low-cycle range and the high-cycle range. There is no definite dividing line between the two. A good assumption might be that the low-cycle range is between 0 to about 10^3 or 10^4 cycles and the high cycle range is about 10^3 or 10^4 cycles to 10^7 or higher. Low-cycle fatigue gained attention after World War II. It was realized that for some pressure vessels, landing gears, pressurized fuselages, spaceship launching equipment, etc., only a short fatigue life was required.

In most cases of low-cycle fatigue, parts are subjected to cyclic strains rather than cyclic stresses. The distinction between strain cycling and stress cycling is important when plastic deformation is involved. Low (43) showed that within the range 10^3 to 10^4 cycles, the fatigue life in reversed bending for different ductile materials depends on the range of strain only. Kooistra (44), testing steels, found that for a fatigue life of less than $5x10^3$ cycles the

resistance to alternating strain correlated best with the ductility of the steel, as determined by the elongation in a static tensile test. He also observed that for fatigue life between $5x10^3$ to $2x10^4$ cycles the resistance to alternating strain was almost independent of the tensile properties, while above $2x10^4$ cycles the resistance was more closely proportional to tensile strength. This implies that the fatigue life of a material when cyclic plastic strain is involved depends on its ductility. On the other hand, when cyclic elastic strain is involved, the fatigue life primarily depends on the tensile strength of the material. Therefore, the fatigue life for total alternating strain depends primarily on ductility at high stresses when plastic strain predominates and primarily on strength at low stresses when elastic strain predominates.

The importance of the plastic strain range, $\Delta\varepsilon_p$, on low-cycle fatigue of a smooth specimen is demonstrated by the empirical Coffin-Manson Law (45,46). In its general form, the relationship is given by:

$$\Delta\varepsilon_p N^{C_1} = C_2 \qquad (3.7)$$

where $\Delta\varepsilon_p$ is the plastic strain range, N is the number of cycles to failure, and C_1 and C_2 are constants. The value of C_1 is very close to 1/2 for a wide variety of materials

(Figure 3.9).

Coffin made the empirical observation that the constant C_2 could be determined by taking the plastic strain range for 1/4 cycle as the true strain at fracture, ε_t, obtained in a tension test. Therefore, for $C_1 = 1/2$

$$C_2 = (\frac{1}{4})^{\frac{1}{2}} \varepsilon_t = \frac{1}{2} \varepsilon_t$$

and

$$\varepsilon_t = \ln(\frac{A_o}{A})$$

where A_o is the original area, and A is the area of fracture. There have been other proposals made to relate $\Delta\varepsilon_p$ to ε_t, such as $\Delta\varepsilon_p = 2\varepsilon_t$ or $\Delta\varepsilon_p = 1.6\varepsilon_t^{1.75}$, but Coffin's approach is simple and conservative.

For application in design, the plastic strain range is converted to total strain range. The difference between the total and plastic strain range is the elastic strain range, $\Delta\varepsilon_e$, which can be approximated by the expression $2S_y/E$, where S_y is the yield stress. Since it is customary to use 0.2 per cent offset yield strength, and this value is usually greater than the endurance limit, the fatigue curve obtained using $2S_y/E$ for elastic strain range becomes unconservative in low stress-high cycle range. Therefore, it has

been suggested that a better result can be obtained if the elastic strain range is taken as $2S_e/E$, where S_e is the endurance limit and E is the modulus of elasticity. Combining these expressions, one can write

$$E\varepsilon_a = \frac{E\Delta\varepsilon_p}{2} + \frac{E\Delta\varepsilon_e}{2} \qquad \text{since} \quad \Delta\varepsilon_{total} = 2\varepsilon_a$$

$$E\varepsilon_a = \frac{E}{2}\left[\frac{\varepsilon_f}{2N^{\frac{1}{2}}}\right] + \frac{E}{2}\left[2\frac{S_e}{E}\right]$$

$$E\varepsilon_a = \frac{E\varepsilon_f}{4N^{\frac{1}{2}}} + S_e \tag{3.8}$$

A rule of thumb established by Peterson is that at $\pm 1\%$ strain ($\Delta\varepsilon = .02$) the failure occurs at about 1000 cycles.

The influence of unknown mean stress, such as residual stress, has to be considered in design. It is understood that at the high cycle end of the curve, the addition of a mean stress decreases the endurance limit. The amount of reduction can be determined from the Goodman diagram. But it is not easy to evaluate the mean stress accurately since mean stresses could be produced by welding or an accidental overload. Therefore, it would be advisable to adjust the fatigue curve downward at the high cycle end to allow for the maximum possible effect of mean stress. The Goodman

diagram with the yield line drawn is shown in Figure 3.10. As the mean stress increases along OA' the allowable value of alternating stress decreases along the line $S_e S_u$. If the mean stress is increased beyond A' yielding occurs. Since we cannot allow failure by gross yielding, then A' represents the highest value of mean stress that has any effect on fatigue life. This approach to fatigue design is a conservative one since the actual value of the mean stress in a specific case might well be considerably lower than the value given by point A'. S''_e is the alternating stress required to produce failure when the mean stress is equal to A'. Therefore S''_e is the value at which the high cycle end of the curve (stress or strain vs number of cycles to failure) has to be reduced in order to safely ignore the effect of mean stress. From Figure 3.10 we can write

$$S''_e = S_e \left[\frac{S_u - S_y}{S_u - S_e}\right] \qquad \text{for } S_a < S_y$$

and, for a finite number of cycles:

$$S''_a = S_a \left[\frac{S_u - S_y}{S_u - S_a}\right] \qquad \text{for } S_a < S_y$$

No correction will be necessary if $S_a > S_y$ since the yield line then lies inside the Goodman line.

The notch effect is different in high cycle fatigue than in low cycle fatigue. In low cycle fatigue the stress and strain concentration factors are no longer the same ($K_\sigma < K_\varepsilon$). Two approximate methods are in common use to account for notch effect. They are

$$K_t^2 = K_\sigma K_\varepsilon \tag{3.9}$$

$$K_\sigma = 1 + (K_t - 1)\frac{\sigma_d/\varepsilon_d}{E} \tag{3.10}$$

σ_d and ε_d represent stress and strain at the notch. These approximations agree reasonably well with experimental data.

K_ε can be estimated by using either approach and a stress-strain curve. But this method leads to a very conservative life prediction because it ignores the fact that after initiation in notched parts much of life is spent in crack propagation. So it has been a common practice to apply K_t over the whole range of N to strain cycling data. This would eliminate the need to apply K_f to the high cycle end of the curve and K_ε to the low cycle end of the curve. Therefore, the Coffin-Manson Law (eq. 3.8) becomes

$$K_t\varepsilon_a = \frac{\varepsilon_f}{4N^{\frac{1}{2}}} + \frac{S_e}{E} \tag{3.11}$$

The correction for the unknown mean stress is the same as before.

C - Fatigue Crack Propagation Behavior

The traditional approach in design against fatigue failure was described in the previous sections. The definition of the crack length that initiates the transition from the nucleation stage to the propagation stage is still a controversial subject. But the fact still remains that 80 to 90% of the fatigue life of a smooth part consists of nucleation when the total life is between 10^4 to 10^6 cycle. On the other hand the nucleation life is about 30 to 60% of total life when the smooth part fails between 10^2 to 10^3 cycles.

Until recently little attempt had been made to determine the laws governing the rate of growth of a fatigue crack. This was mainly due to the fact that most investigators based their design on endurance limits of materials obtained from smooth laboratory specimens. Naturally the purpose was to prevent the initiation of any cracks under cyclic loading by keeping the design stresses below some critical value. However, it has been realized that situations may exist where fatigue stresses operate on structures containing large stress concentration. These may be defects in welds or structural design features. Therefore, more attention is now being paid to crack propagation phenomena

rather than crack initiation. Many apparently different empirical laws have been proposed to relate crack growth rate to stress levels and crack length. Recent developments of linear elastic fracture mechanics have improved the understanding of crack propagation behavior. For this reason a brief review of this topic will be presented.

1 - Linear Elastic Fracture Mechanics - A Brief Review

1.1 - Griffith Energy Concept

Griffith (47) used an energy concept in dealing with infinite stresses at the tip of a crack. He supposed that a test sample might contain small flaws which then would enable the stress to be concentrated sufficiently for the theoretical strength to be attained locally at a relatively low overall stress. Griffith then stated that for this pre-existing crack to grow, the work done by external forces less the increase in strain energy has to be greater than the energy required to create fresh surface. Using Inglis' (48) solution for an elliptical crack and assuming a center crack of length 2a situated in an infinite plate of unit thickness Griffith's energy criteria can be mathematically formulated:

$\frac{\pi a^2 \sigma^2}{E'}$ strain energy increase due to the introduction of a crack of length 2a.

$\frac{2\pi a^2 \sigma^2}{E'}$ work done by external load when crack is introduced under load.

$4a\gamma$ corresponding increase in surface energy.

Therefore the Griffith's criterion is:

$$\frac{\partial}{\partial a}\left[\frac{\pi\sigma^2 a^2}{E'} - 4a\gamma\right] = 0$$

and for the critical stress, σ_c , we have

$$\sigma_c = \sqrt{\frac{2E'\gamma}{\pi a}} \qquad (3.12)$$

where $E'=E$, for plane stress and $E'=E/(1-\nu^2)$, for plane strain.

The difficulty with Griffith's criteron is the term γ. The surface energy, γ, is a thermodynamic value that can be measured by a variety of tests unrelated to fracture. For most materials the values of surface energy found from fracture tests are much greater than the thermodynamic values. This discrepancy is due to the fact that localized plastic deformation occurs during fracture testing. Later on, Irwin (49) modified Griffith's theory by suggesting that a surface energy characteristic of fracture can be measured in a fracture test. He defined G_c as the work required to create a unit increase in the crack area by fracture. G_c then could

be compared to the energy released by unit crack extension, G, (i.e. work done by external forces - increase in strain energy) G, to reach a conclusion as to the behavior of the crack. If $G<G_c$ the crack is stable, if $G>G_c$ the crack is unstable and should propagate, and if $G=G_c$ the crack is in metastable equilibrium.

G can be determined experimentally by what is commonly known as the compliance method. By referring to Figure 3.11 one can obtain the expression for the energy released by an increase in crack length δa.

$$G \cdot B \cdot \delta a = (P + \frac{\Delta P}{2}) \delta u - \Delta W_e \qquad (3.13)$$

where B is the thickness of the plate and ΔW_e is the elastic energy due to crack length increase of δa. The compliance is defined as the reciprocal of the slope of the load-deflection curve ($C = \frac{u}{P}$). The elastic strain energy is given by $W_e = \frac{CP^2}{2}$. In the limit, equation (3.13) becomes

$$G \cdot B = P\frac{du}{da} - \frac{dW_e}{da}$$

Substituting for u and W_e their corresponding values in terms of C and P we have:

$$G \cdot B = P\frac{d(CP)}{da} - \frac{d(CP^2)}{2da}$$

That is,

$$G = \frac{P^2}{2B} \frac{dC}{da} \tag{3.14}$$

Therefore the problem is reduced to measuring the compliance of the specimen as a function of crack length and obtaining the quantity dC/da.

1.2 - Stress Intensity Factor

The surfaces of cracks are stress free boundaries adjacent to the crack tip and therefore dominate the distribution of stresses in that area. The stress field distribution depends on the mode of crack surface displacement. There are basically three different modes of crack surface displacement (Figure 3.12). The opening mode I is characterized by the crack surfaces moving directly apart. The edge sliding mode II is characterized by the crack surfaces moving normal to the crack front and remaining in the crack plane as opposed to the shear mode III where the crack surfaces move parallel to the crack front in the crack plane. The magnitude and distribution of the stress field near a fatigue crack tip can be related to the nominal stress applied, to the geometry and crack length, and to the

material properties by using the concepts of linear elastic fracture mechanics (LEFM). This approach to fracture makes use of elastic solutions for stresses near sharp cracks. These solutions are only valid if the plastic zone in the crack tip region is of limited size. The elastic-stress field, for mode I deformation, near a sharp crack (that is, tip radius, ρ, approaches zero) is represented by the following equations (50).

$$\sigma_x = \frac{K_I}{(2\pi r)^{\frac{1}{2}}} \cos\frac{\theta}{2}\left[1 - \sin\frac{\theta}{2}\sin\frac{3\theta}{2}\right] \tag{3.15}$$

$$\sigma_y = \frac{K_I}{(2\pi r)^{\frac{1}{2}}} \cos\frac{\theta}{2}\left[1 + \sin\frac{\theta}{2}\sin\frac{3\theta}{2}\right]$$

$$\tau_{xy} = \frac{K_I}{(2\pi r)^{\frac{1}{2}}} \sin\frac{\theta}{2}\cos\frac{\theta}{2}\cos\frac{3\theta}{2}$$

$$\sigma_z = \tau_{xz} = \tau_{yz} = 0$$

where the stress components and the coordinates r and θ are as shown in Figure 3.13. It should be noted that these equations apply to plane stress conditions. For plane strain conditions one has to set σ_z equal to Poisson's ratio times the sum of σ_x and σ_y.

The elastic-stress field near a sharp elliptical or hyperbolic notch is different from that of a sharp crack. For mode I and plane stress condition we can write (51):

$$\sigma_x = \frac{K_I}{(2\pi r)^{\frac{1}{2}}} \cos\frac{\theta}{2}\left[1 - \sin\frac{\theta}{2}\sin\frac{3\theta}{2}\right] - \frac{K_I}{(2\pi r)^{\frac{1}{2}}}\frac{\rho}{2}r\cos\frac{3\theta}{2}$$

$$\sigma_y = \frac{K_I}{(2\pi r)^{\frac{1}{2}}} \cos\frac{\theta}{2}\left[1 + \sin\frac{\theta}{2}\sin\frac{3\theta}{2}\right] + \frac{K_I}{(2\pi r)^{\frac{1}{2}}}\frac{\rho}{2}r\cos\frac{3\theta}{2} \qquad (3.16)$$

$$\tau_{xy} = \frac{K_I}{(2\pi r)^{\frac{1}{2}}} \sin\frac{\theta}{2}\cos\frac{\theta}{2}\cos\frac{3\theta}{2} - \frac{K_I}{(2\pi r)^{\frac{1}{2}}}\frac{\rho}{2}r\sin\frac{3\theta}{2}$$

where the stress components, coordinates r, θ, and ρ are defined in Figure 3.14. In these equations the second term represents the effect of notch radius, ρ, on the stresses around the notch. Similar equations for stresses near the crack tip can be written for mode II and mode III.

These equations show that the stresses near the crack tip can be described by a single parameter K_I called the stress intensity factor. Relationships between the stress intensity factor and various body configurations, crack sizes, and loading conditions have been documerted in the literature (52).

For example, for a compact tension specimen (see appendix) K_I can be determined using the boundary collocation

method and is found to be

$$K_I = \frac{P\sqrt{a}}{BW}\left[29.6-185.5\left(\frac{a}{W}\right)+655.7\left(\frac{a}{W}\right)^2-1017.0\left(\frac{a}{W}\right)^3+638.9\left(\frac{a}{W}\right)^4\right]$$

where P is the applied load, B is the thickness of the specimen, and a and W are the crack length and width of the specimen measured from the location of the applied load as shown in Figure A.1.

As was mentioned above, many solutions for the stress intensity factor, K_I, at the tip of the crack exist. However, it is important to note that most K_I equations relate to the 'long crack' or 'pure crack' cases. It is assumed that the crack has propagated away from the crack starter making it unnecessary to regard the influence of such a crack starter on K_I. Therefore, in dealing with short crack problems one has to know the depth beyond which a notch (crack starter) with an emanating crack can be treated as a crack of equivalent length. Novak and Barsom (53) studied the brittle fracture behavior of cracks starting from notches. They concluded that the geometry of the starter notch could be neglected when the crack had grown a distance Δa_F given by

$$\frac{\Delta a_F}{\sqrt{a_N \rho}} = \frac{1}{4}$$

where a_N and ρ are the length and radius of a notch respectively.

Since the stress intensity factor approach to fracture deals with the conditions at the crack tip, it is expected that fracture will occur when K reaches a critical value, K_c. This is considered a material property and is obtained in a laboratory test.

The validity of this approach depends on the plastic zone size, as compared to the crack length and the geometry of the specimen. Therefore, it is important to estimate the size of the plastic zone. Conventionally, the expressions used are:

$$r_y = \frac{1}{2\pi} \left(\frac{K_I}{\sigma_{ys}} \right)^2 \qquad \text{for plane stress} \qquad (3.17)$$

$$r_y = \frac{1}{6\pi} \left(\frac{K_I}{\sigma_{ys}} \right)^2 \qquad \text{for plane strain} \qquad (3.18)$$

where σ_{ys} is the yield strength of the material.

It is interesting to note that the energy concept and stress intensity approach to fracture can be related. Irwin (50), using virtual work arguments, unified these two

approaches and showed that:

$$G = \frac{K_I^2}{E'}$$

where $E'=E$ for plane stress and $E' = E/(1-\nu^2)$ for plane strain.

The outline of LEFM which has been presented is a highly simplified one but should be adequate for the subsequent discussion. It should be mentioned that K_c and G_c are functions of thickness. The values they approach for large thicknesses are referred to as the "plane strain fracture toughness".

IV - FATIGUE CRACK PROPAGATION

A - Mechanisms of Crack Propagation

1 - Introduction

It is now known that crack propagation in fatigue takes place in two stages (Figure 4.1). Stage I is characterized by propagation of the crack on a plane oriented at approximately 45 degrees to the tensile stress axis. In stage II propagation, the plane of crack propagation shifts to 90 degrees to the axis and the fracture surface is often covered by striations running parallel to the crack propagation front. Failure in high strain fatigue takes place mainly in stage II propagation, whereas, at lower strains, at least 90% of the fatigue life of an unnotched specimen is spent in stage I propagation (54). Rates of crack propagation in stage I are of the order of angstroms per cycle which makes this stage very difficult to study. On the other hand, crack propagation rates in stage II can reach values of microns per cycles and the phenomena associated with growth mechanisms are fairly large and relatively easy to observe. Crack propagation in stage II appears to take place by a plastic blunting mechanism.

2 - Plastic Blunting Process of Crack Growth

The plastic blunting mechanism was first proposed by Laird and Smith (55). The process involves shear decohesion of material at the tip of the crack during tensile loading. The amount of decohesion is actually the amount of new crack surface created at each cycle. The mechanism is shown schematically in Figure 4.2. As the stress is increased from maximum compression, flow bands extend in the maximum shear directions at the tip of the crack to relax the high stress concentration developed. As the tensile stress approaches the maximum value, the flow band width increases and shear decohesion occurs at the inner edge of the flow band and therefore creates new crack surface. Under high plastic strain, the flow bands can spread inwards leading to a crack tip of the form shown in Figure 4.2 (f).

Although this mechanism has been described for tension-compression loading, crack propagation by shear decohesion could obviously take place under other modes of applied stress such as tension-tension and alternating shear.

In stage I crack propagation illustrated in Figure 4.3, the increase in crack length per cycle is achieved by spreading of the crack tip width of the slip zone (b). Presumably, the required component of deformation normal to the slip band can occur by duplex slip within the band, rather than by operation of a second slip band, as is the

case in stage II crack propagation. There have been other mechanisms proposed for stage I crack propagation. However, all of these mechanisms involve crack growth by localized deformation, therefore they are basically the plastic blunting process. The main difference between stage I and II of crack propagation lies in the different types of dislocation motion in the two cases.

The appearance of striations on the fracture surface is attributed to the plastic blunting process. However it is possible for the fatigue failure to occur in the absence of striations on the fracture surface. The work hardening characteristics of a material appear to dictate the clarity of the striations. This is consistent with the observation that striations are very clear in Aluminum alloys and low strength steels as opposed to high strength steels.

3 - Growth by Non-Striation Mechanisms

Lindley, Richards and Ritchie (56) proposed that the mechanism of fatigue crack propagation could include contribution from fracture modes ("static" modes) other than striation formation. These "static" fracture modes may include cleavage, microvoid coalescence and intergranular cracking. Richards (57), testing silicon-iron, observed that fatigue crack propagation occurred by combined striation formation and cleavage cracking. Microcleavage may also occur during fatigue crack growth in a material containing brittle second

phase particles.

A void coalescence mechanism for fatigue crack propagation has been proposed by Ryder and Forsyth (58). In this mechanism, voids form ahead of the crack and eventually coalesce during the cyclic loading. However, it appears that this mode of growth is only significant when propagation rates are high and the specimen is approaching final failure.

An intergranular mode of fatigue crack propagation has been observed for quenched and tempered high strength steels where fatigue cracks tend to follow prior austenite grain boundaries. Again, the intergranular mode of propagation is usually accompanied by higher growth rates (59,60).

4 - Effect of Testing Variables on Fatigue Crack Propagation

Ritchie and Knott (59) studied the effect of mean stress on crack propagation rate in stage II crack growth. An unembrittled low alloy steel (En 30A) was tested at stress ratios, $R = \frac{\sigma_{min}}{\sigma_{max}}$, between .05 to .6. They showed clearly that when the striation mechanism of fatigue is involved, the influence of mean stress is negligible. On the other hand, in the presence of "static" fracture modes, we might expect a strong dependence of the propagation rate on mean stress.

Cooke and colleagues (61) have shown noticeable accelerated crack propagation in a medium carbon steel as the stress ratio, R, is increased from .1 to .72, causing increasing amounts of cleavage cracking to occur during the striation growth. On the other hand, crack growth rate was observed to be independent of stress ratio in a similar steel when cleavage cracking did not occur. Microcleavage of particles also plays an important role on the effectiveness of mean stress on crack propagation rate. It has been observed in high strength aluminum alloys (62) that the increase in crack growth rates with an increase in mean stress were the result of microcleavage of particles. Pearson (63) has shown that the mean stress dependence is removed in lower strength aluminum alloys where such fractures cannot occur.

In general, this sensitivity of crack propagation rate to mean stress seems to be almost entirely due to a change in mechanism from purely striation formation to striation and "static" modes of fatigue failure. Therefore, by changing the microstructure to prevent the occurrence of "static" modes of fracture during striation growth, the dependence of fatigue crack propagation rate on mean stress can be greatly minimized.

The influence of specimen thickness on fatigue crack propagation by the striation mechanism appears to be small.

A slight variation in crack growth rates between thin and thick specimens can occur from a difference in specimen geometry and the accompanying displacement restraints. For example, the propagation rate has been found to be faster in thick specimens tested in bending, whereas, the reverse has been observed when the same material is tested in tension (64,65). However, it has been stated that the fatigue crack propagation rate is higher in thin specimens as compared to a thick specimen due to the earlier onset of general yielding in thinner test specimens (66).

The "static" mode of fracture has an influence on the effect of thickness on crack propagation rate. Richards and Lindley (67) observed that an increase in thickness caused a marked increase in crack growth rate which was in contrast to the result for striation mechanisms. They proposed that the increase in growth rate was caused by the occurrence of microcleavage in the mechanism of growth.

Faster crack propagation rates with increasing thickness have also been observed in a coarse grained high nitrogen mild steel (64,65) where cleavage cracking added to the striation mechanism of growth. Garrett (68) observed that the growth rates in aluminum alloys were faster in 13mm thick specimens than in 2.5mm thick, but only when K_{max} approaches the value for final failure. Under these conditions, the failure mechanisms in such materials become

dependent on void coalescence and hence on the triaxiality of stress.

From available data it appears that the cyclic stress frequency has little effect on crack propagation rate. It is also well understood that the shape of the waveform (i.e., sinusoidal, triangular, square, etc.) does not influence the crack propagation rate (69) in an inert environment.

B - Crack Propagation Laws

In the early years of crack growth studies, crack propagation laws proposed usually related the crack length, a, to the number of cycles of load applied, N, the stress range, σ, and a material constant, C. Therefore, in general one can write:

$$\frac{da}{dN} = f(\sigma,a,C)$$

The first crack propagation law that attracted some attention was given by Head (70). After extensive calculations based on rather idealized assumptions about material behavior, Head's law can be written:

$$\frac{da}{dN} = \frac{C_1\sigma^3 a^{3/2}}{(\sigma_y-\sigma)w^{\frac{1}{2}}} \qquad (4.1)$$

where C_1 depends on the modulus of elasticity, the fracture

stress and yield stress, σ_y, of the material, and the strain-hardening modulus. w is defined as the plastic zone size ahead of the crack tip, remaining constant during crack propagation. However, Frost and Dugdale (71) observed that the plastic zone size did not stay constant during crack propagation but actually increased in direct proportion to crack length. Later on Irwin (72) pointed out from analytical considerations that:

$$w = c^2 a \tag{4.2}$$

Therefore, Head's law can be modified by introducing equation (4.2) into (4.1):

$$\frac{da}{dN} = \frac{C_2 \sigma^2 a}{(\sigma_y - \sigma)} \tag{4.3}$$

Frost and Dugdale (71) suggested a new approach to crack propagation. They agreed with equation (4.3) that the growth rate depends linearly on the crack length. But they also showed, by dimensional analysis, that da/dN should be directly proportional to the crack length a, therefore:

$$\frac{da}{dN} = Ba \tag{4.4}$$

where B is a function of applied stress. Later on, to fit their experimental data they obtained:

$$B = \frac{\sigma^3}{C_3}$$

and

$$\frac{da}{dN} = \frac{\sigma^3 a}{C_3} \qquad \text{(Frost and Dugdale's Law)} \qquad (4.5)$$

Liu (73) using a model of crack extension employing an idealized elastic-plastic strain-stress diagram and a concept of total hysteresis energy absorption to failure obtained different results for the function B.

$$B(\sigma) = C_4\sigma^2$$

and

$$\frac{da}{dN} = C_4\sigma^2 a \qquad \text{(Liu's Law)} \qquad (4.6)$$

Many crack propagation laws of this form have been proposed and they all can be generalized in the form of:

$$\frac{da}{dN} = (\text{CONSTANT})\sigma^m a^n$$

The discrepancy here appears to arise from the fact that the investigators have compared predictions with experiments over a small range of variables.

The stress intensity factor combines the effect of applied stress, crack length, and the specimen geometry into a single parameter K. Therefore, it is reasonable to suggest that the stress intensity factor should control the

rate of crack propagation. That is:

$$\frac{da}{dN} = f(\Delta K) \tag{4.7}$$

where $\Delta K = K_{max} - K_{min}$ is the range of the stress intensity factor. Moreover, this stress intensity factor approach allows the convenience of representing crack propagation rates for various types of specimen geometry on a single graph.

Equation 4.7 was first suggested by Paris (74) who chose a specific form. Paris' Law in a general form can be written:

$$\frac{da}{dN} = C(\Delta K)^n \tag{4.8}$$

where c and n are material constants. Generally, ΔK is taken as K_{max} when K_{min} is negative since crack growth would not be expected if the crack faces are touching. However, in welded construction with residual stresses present ΔK is usually taken as $K_{max}-K_{min}$ even when K_{min} is negative.

Crack propagation rate da/dN vs. ΔK , where a is the crack length, N is the number of cycles and ΔK is the range of the stress intensity factor is best presented on a log-log plot by separating it into three parts (Figure 4.4). Part A exhibits a ΔK -threshold value (ΔK_{th} ranging from 2-7 ksi-in$^{\frac{1}{2}}$), below which crack propagation does not occur. Part B is usually a straight line and is governed by Paris'

law $da/dN = C(\Delta K)^n$, where C and n are material properties (n ranging from 2-6). In Part C, where K_{max} is approaching the fracture toughness K_c, crack propagation accelerates greatly. Figure 4.4 also shows a summary of the effect of mean stress, microstructure and thickness on different stages of crack propagation.

Numerous experiments have been performed on different materials to evaluate the values of C and n. For example, Barsom (75) as a result of extensive studies proposed two forms of equation 4.8 for steels. For tempered-martensite steels equation 4.8 becomes:

$$\frac{da}{dN} = 0.66\times10^{-8}(\Delta K)^{2.25}$$

For ferrite-pearlite steels equation 4.8 takes the form of:

$$\frac{da}{dN} = 3.6\times10^{-10}(\Delta K)^{3}$$

where da/dN is in inches per cycle and ΔK is in ksi-$in^{\frac{1}{2}}$.

Frost and Dixon (76) stated that the geometry of the crack tip profile could be determined to a first approximation by the elastic opening of the crack. They proposed that under cyclic stress a crack in an elastic sheet opens up into an ellipse and the stress distribution around this ellipse can be calculated using the elastic solution for an elliptical hole. Later on, Frost and Pook (77) re-expressed this theory and proposed that the crack tip opens up into a

parabola. It was also assumed that the part of the crack tip which is subjected to a tensile stress greater then yield stress retains its length when the load is removed. Their results, for high fracture toughness materials, can be written:

$$\frac{da}{dN} = C(\frac{\Delta K}{E})^2 \qquad (4.9)$$

On this basis the crack propagation rate for typical values of E/S_y, can be generalized as follows:

$$\frac{da}{dN} = \frac{9}{\pi}(\frac{\Delta K}{E})^2 \qquad \text{(for plane stress)}$$

and

$$\frac{da}{dN} = \frac{7}{\pi}(\frac{\Delta K}{E})^2 \qquad \text{(for plane strain)}$$

Paris' law has been modified to include the effect of test variables, such as mean stress and complex load sequence. For example, Forman et al (78) developed an equation providing a means for comparing crack growth data obtained at different stress range ratios. The relationship has the form:

$$\frac{da}{dN} = \frac{C(\Delta K)^n}{(1-R)K_c - \Delta K} \qquad (4.10)$$

where R is the ratio of minimum to maximum stress and K_c is the critical stress intensity factor in plane stress. Forman's equation, while accurate for 2024-T3 aluminum

alloy, is unsuccessful in predicting the effect of R on the crack propagation rate for titanium alloys.

In order to study the effect of random loading on crack propagation rate Barsom (79) performed experiments on various bridge steels and arrived at the following equation:

$$\frac{da}{dN} = C(\Delta K_{rms})^n \tag{4.11}$$

where ΔK_{rms} is the root-mean-square stress intensity factor.

Paris' law basically describes the crack propagation behavior in region B. This law has to be modified to account for the very low and very high rates of crack propagation which occur in region A and C respectively. Heald et al (80) have proposed an expression for region C where crack growth enhancement is associated with a non-striation mechanism:

$$\frac{da}{dN} = A\left[\frac{\Delta K^4}{\sigma_1^2(K_c^2-K_{max}^2)}\right]^n \tag{4.12}$$

where A is a material constant, K_{max} the maximum stress intensity factor, K_c the fracture toughness of the material, and σ_1 a strength parameter.

It appears now that a crack will not grow under cyclic loading unless the range of stress intensity factor during a fatigue cycle ΔK exceeds a critical value (region A in Figure 4.4). This critical value is known as ΔK-threshold.

The values of ΔK_{th} for a wide range of materials have been obtained experimentally. The values of ΔK_{th} decrease as the mean stress is increased and are approximately proportional to $(\frac{\sigma_a}{\sigma_m})^{\frac{1}{3}}$. In general, environment has a greater effect on ΔK_{th} than on the crack propagation rate. More work is necessary to obtain a satisfactory crack propagation law describing region A.

C - Role of Environment in Crack Propagation

A corrosive environment has an influence on both the fatigue crack propagation rate and crack initiation. The magnitude of the effect in either case depends on many factors such as the nature of the environment, the type of material used and the testing variables (frequency, stress, geometry, etc.).

1 - Aqueous Environment

The effect of aqueous environment on the crack growth rate has been the subject of many studies and a number of mechanisms have been proposed to explain the increase in crack growth rate in the presence of a corrosive environment. These include anodic dissolution, hydrogen embrittlement and surface layer stresses, among others.

Once a crack has been nucleated, the region in the tip

of the crack becomes highly anodic, due to plastic deformation at the tip, compared to the remaining cathodic region. Thus, a rapid dissolution of the crack tip takes place. Hoar and West (81) confirmed this model by observing the dissolution effects during plastic deformation of stainless steel.

Hydrogen induced cracking of steel in an aqueous environment is believed to be caused by absorption of hydrogen atoms formed on the surface of the steel. These combine to the molecular form which builds up pressure in microcracks and leads to embrittlement. When a sharp crack is already present, such as a fatigue crack, the hydrogen cracking may initiate at the tip of the pre-existing crack. Hydrogen embrittlement effects on steels decrease as the strength level of the steel decreases.

Kramer (82,83) suggests that the surface layer which is formed as a result of plastic deformation exerts a major influence on the fatigue crack initiation and propagation. He further proposes that the surface layer stress, which he defines as the additional resistance to deformation imposed by the presence of the surface layer, is affected by the environment. The experimental results show that crack growth rate is higher in a hostile environment as compared to air. Correspondingly, the surface layer strength decreases for specimens tested in air and increases for

specimens tested in a corrosive environment. Therefore, the increase in crack propagation rate in corrosion fatigue may be explained in terms of the increase in the surface layer stress.

2 - Gaseous Environment

Early work by Wadsworth and Hutchings (84) showed that the fatigue life of 2024-T3 aluminum alloy in a vacuum of 10^{-5} Torr was about 5 times the life in air. They suggested that crack initiation occurred after about the same number of cycles in air and in vacuum and that the effect of the moisture in air was to accelerate propagation. Dahlberg (85) reported that the rate of fatigue crack propagation of 4340 steel was increased by an order of magnitude when water vapor was added to dry air. Mantel et al (86) observed that the fatigue life of steel in hardened condition was almost ten times longer in dry argon than in moist argon.

The effect of hydrogen on corrosion fatigue has been studied by Spitzig and co-workers (87). They tested 18Ni maraging steel in both dry hydrogen and hydrogen saturated with moisture. A dramatic reduction in the crack propagation rate was observed when moisture was added.

From the experimental results presented in the literature, it appears that hydrogen has a severe effect on the fatigue crack propagation of many alloys used in structures.

These include nickel and titanium based alloys and ordinary steels. On the other hand, the fatigue life of aluminum and copper based alloys and austenite steels seems to be unaffected by hydrogen.

It is important to point out that striations are not formed in most fatigue tests performed in vacuum, whereas very distinct striations are formed in air. Pelloux points out that this observation of the fracture surface shows the inadequacy of the plastic blunting theory to explain the formation of striations. He suggests that the freshly exposed crack surface is immediately oxidized in air and therefore limits the amount of reversibility of deformation at the crack tip.

D - Corrosion Fatigue

Corrosion fatigue is the combined action of cyclic stress and a corrosive environment. Usually, an aggressive environment has a great effect on the fatigue life of a material. It causes a part to fail in fewer stress cycles than would be required in an inert environment. The microscopic process by which crack initiation and propagation are affected by the environment is not completely understood. As has been discussed in Chapter II and previous sections, many mechanisms have been proposed to explain the microscopic behavior of corrosion fatigue. No single model can

explain all of the fractographic observations that have been made in different combinations of material and environment. On the other hand, the behavior patterns of the crack growth in the presence of a corrosive environment can be generalized.

The environment enhanced fatigue crack propagation response of high strength metals could be generalized into the three categories shown in Figure 4.5. The first type of behavior (a) represents the material-environment systems where the synergistic actions of fatigue and corrosion take place, resulting in an acceleration of the crack growth rate. The best example for this type of behavior is when water reacts with aluminum (88) - the threshold for crack growth is reduced and the environmental influence is diminished as K approaches K_{Ic} or K_c.

The second type of behavior (b) represents a typical effect of hydrogen on steel. The environmental effects are strong above some threshold for stress corrosion cracking (K_{Iscc}) and are negligible below this level. K_{Iscc} is defined as the highest stress intensity factor value at which crack growth does not occur in a material loaded statically in a corrosive environment. A broad range of material-environment systems show a behavior that falls between these two extremes (c).

Test frequency plays an important role in the effectiveness of the environment on corrosion fatigue crack growth. The data available to date suggest that the effect of the environment on crack propagation is reduced as the frequency of applied cyclic stress is increased. This could be attributed to the fact that at higher frequencies there is not enough time for the environment to attack the crack tip.

The wave form of the applied cyclic stress may also have an effect on corrosion fatigue crack growth. Barsom (69) tested 12Ni-5C-3Mo steel in room temperature and 3% sodium chloride under sinusoidal, triangular, and square loading at 6 cpm. He observed that the increase in crack growth rate due to salt water under sinusoidal and triangular stress fluctuations were almost identical. But the corrosion fatigue crack growth rate under square wave loading was very close to that in air. On the other hand, experiments by Bradshaw et al (89) on an aluminum alloy, using different wave forms, indicates no effect of wave form. Therefore it appears that the effect of wave form depends on the material-environment system.

The effect of mean stress is not the same for different material-environment systems. For type (a), the influence of stress ratio on crack growth in an aggressive environment is comparable with that of an inert environment. On the

other hand, for types (b) and (c), the effect of the stress ratio can be large since it affects the period for which K is above some threshold level during a given load cycle.

Gallagher (90) suggest that the corrosion fatigue behavior of steels falls into two categories: above K_{Iscc} and below K_{Iscc}. The corrosion fatigue crack growth rates in steels tested with K_{max} above K_{Iscc} have been observed to be governed either by fatigue cracking mechanisms, the environmental cracking mechanism, or by a combination of these two mechanisms. At low frequencies, the crack propagation mechanism is the environmental cracking mechanism while at high frequency, the fatigue cracking mechanism seems to play a dominant role. In steels tested with K_{max} below K_{Iscc} the fatigue cracking mechanism is the controlling mechanism. The environment appears to enhance the fatigue cracking rate only when the fresh surfaces generated by the fatigue mechanism are produced slowly. To explain this behavior it has been suggested that the fatigue crack advances during the loading part of the cycle and the environmental attack process requires a sufficient amount of time to act.

E - Cathodic Protection

In an aqueous environment, corrosion usually takes place by an electrochemical mechanism. In this type of

attack, numerous local galvanic couples form on the surface of a corroding metal in which the metal is spontaneously oxidized and some substance is reduced. Each couple acts as a simple cell (battery) and the corrosion reaction proceeds with current flowing from the anodic to the cathodic regions on the metal.

At the anodes on a corroding surface, metal is oxidized to positive ions. In the case of iron we have

$$Fe \rightarrow Fe^{++} + 2e^{-} \quad \text{(electrons)}$$

Away from the surface, the metal ions react with hydroxyl ions in the surrounding electrolyte to form precipitates of corrosion products. With iron the reaction is

$$Fe^{++} + 2OH^{-} \rightarrow Fe(OH)_2 + 2e^{-} \qquad (1)$$

Depending on exposure conditions, the precipitate is slowly oxidized to ferric hydroxide and eventually dehydrated to the iron oxides commonly observed in rust.

At the cathode, the reduction reactions that occur depend on the environmental conditions. In the absence of air, hydrogen generation takes place. This attack, known as hydrogen-type corrosion, occurs by one of these reactions:

$$2H^{+} + 2e^{-} \rightarrow H_2(g) \qquad (2)$$

$$2H_2O + 2e^{-} \rightarrow H_2(g) + 2OH^{-} \qquad (3)$$

In acid media, reaction (2) dominates.

In the presence of air, the reduction of oxygen is more spontaneous than hydrogen evolution. Several reactions are

possible:

$$O_2 + 4H^+ + 4e \longrightarrow 2H_2O \qquad (4)$$

$$O_2 + 2H_2O + 4e \longrightarrow 4OH^- \qquad (5)$$

$$O_2 + 2H_2O + 2e \longrightarrow H_2O_2 + 2OH^- \qquad (6)$$

Reaction (6) usually does not occur to any appreciable extent. Under acid conditions, reaction (4) is dominant and in neutral or alkaline environments, reaction (5) predominates.

To prevent corrosion there must be no anodic reaction; that is the anodic current should be zero or negative. The anodic current can be reduced to zero or negative by externally impressed current. To achieve this, the positive terminal of the source of direct current is connected to the auxiliary electrode (anode) and the negative terminal to the metal to be protected (cathode). Current then flows from the electrode through electrolyte to the metal. The cathode of the cell still acts as a normal cell cathode though with an increased reaction rate. This means that the former anodic area is now itself acting as a cathode and no corrosion will occur. This method of corrosion control is known as cathodic protection.

In applying cathodic protection, it is essential to determine the current requirement established by the properties of the surface to be protected and the environment. Table 4.1 shows the approximate protective currents for

steel in various environments. As a general rule, a shift of 150 to 200 millivolts in surface potential is desired for safe protection.

V - EXPERIMENTAL WORK

The experimental work was performed using two types of steels - 1018 and HY-180 steel. The experiments carried out included testing both steels in air and salt water environments. Different frequencies and load ratios (P_{min}/P_{max}) were employed to study the crack propagation behavior of the steels mentioned above. In addition to crack propagation, crack initiation was also studied using 1018 steel specimens. Cathodic protection was imposed on some of the specimens during the corrosion testing to observe its effect on the crack propagation rate.

A - Materials

The materials involved in this investigation were 1018 steel with yield strength of 40 ksi and HY-180 steel with yield strength of 180 ksi. The 1018 steel was supplied as 0.5 inch by 6.0 inch by 10 foot long hot-rolled plate. The 1018 specimens were machined from the as-received stock with no heat treatment involved. The HY-180 specimens were obtained from 0.5 inch thick plate stock and were machined before any heat treatment. The HY-180 specimens were then austenitized at 1500°F and quenched and aged at 950°F for 5

hours. The chemical compositions and mechanical properties of 1018 and HY-180 steels are summarized in Tables 5.1 and 5.2 respectively.

B - Specimens

All of the fatigue initiation and propagation testing involved in this investigation was performed using 1/4 inch-thick compact tension specimens. The standard compact tension specimen was modified for crack initiation studies. Instead of precracking the specimen, a single notch of a certain radius was machined at the end of the slot. Since the number of cycles required to initiate a fatigue crack was determined by examination of the notch radius on the surface of the specimen the thickness of the specimen was chosen as 1/4 inch. In this way, the crack will propagate rapidly to the side of the specimen once it has initiated inside the notch. The geometry of the specimens involved in this investigation included a notch with a radius of 0.015 inch for 1018 steel and 0.04 to 0.05 inch for HY-180 steel. A drawing of the compact tension specimen is shown in Figure 5.1. Note that the total notch depth is measured from the centerline of loading to the notch tip and is 1.0 inch. The compact tension specimens with a notch were used to develop both crack initiation and propagation data. The appendix shows the procedure to follow for calculating the stress

intensity factor for a compact tension specimen.

C - Equipment and Testing Apparatus

1 - Equipment

Most of the fatigue crack initiation and propagation testing was conducted on a closed loop hydraulic fatigue machine (MTS) with load capacity of 50,000 lbs. An oscilloscope was used to monitor the load variations during testing. A few experiments were carried out on an Instron fatigue machine (20,000 lbs) due to the unavailability of the MTS machine at the start of this investigation.

2 - Loading Assembly

A specific fixture was designed so that the compact tension specimen could be mounted on both the Instron and MTS fatigue machines. Figure 5.2 shows a sketch of the fixture used in this investigation. The fixture was designed in such a way that it would not interfere with the mounting of the corrosion chamber on the specimen. The fixture is made of heat treated 4340 steel and is designed to withstand an infinite number of cycles. To complete the loading assembly, a 2 1/2 inch long threaded bar is used to attach the fixture to the existing setup on the fatigue testing machines.

3 - Corrosion Chamber

The corrosion chamber used consists of two identical units made of stainless steel. Figure 5.3 shows the drawing for each unit. The units were mounted on both sides of the specimen covering the notch and the crack propagation path. The two units were fastened together (with the specimen in between) by two bolts on the outside of the specimen and a third bolt passing through the slot of the compact tension specimen. Figure 5.4 shows a photograph of the corrosion chamber mounted on the compact tension specimen. A window was cut in each unit and a clear plastic sheet glued to the window so that the crack would be visible through the salt water solution. In order to avoid leakage, an O-ring was used between each unit and the specimen. To further guard against leaks, a silicone sealing compound was used around the corrosion chamber and inside the specimen slot.

D - Crack Detection Method - Visual Technique

The visual technique of crack detection and growth was used in this investigation due to its simplicity and low cost. The technique used consisted of printing prepared lines photographically on the surface of the specimen perpendicular to the cracking direction and spaced at 0.02 inch (Figure 5.5). This technique involves applying a photographic emulsion to the surface of the specimen, exposing the emulsion through a negative with carefully prepared

lines, and rinsing off the unexposed emulsion with water leaving only the lines on the specimen. Then a 20 power microscope can be used to view these lines. For best results, the surface of the specimen should be polished and a strobe light used for viewing the crack as it propagates through the grid lines. An advantage of this method is that the experiment does not have to be stopped to record measurements. Moreover, viewing the cracks against the grid lines on the surface of the specimen is sufficiently easy through water, salt water and clear oil, as well as air, without having to account for optical distortion, since the crack is referenced against the grid lines. For more accurate results in detecting the crack initiation length on the side of the specimen, the test should be performed at a relatively high ΔK_I level so that the number of cycles required for the first crack, initiated inside the notch, to grow to the surface is relatively small.

E - Experimental Procedure and Results

1 - Air Environment Tests

The 1018 steel specimens were tested to generate crack initiation and propagation data, whereas the HY-180 specimens were used to obtain only propagation data. All of the crack initiation and propagation testing conducted on the fatigue machines was performed under constant amplitude

sinusoidal tension-tension loading corditions. The testing apparatus used in this investigation is shown in Figure 5.6.

Table 5.3 presents the crack initiation data obtained for 1018 steel. The number of cycles to initiate a crack was obtained assuming a .01 inch crack length measured on the side of the specimen. The applied stress was varied from 15,000 to 32,000 psi. All of the initiation tests were carried out at the frequency of 2 HZ. It is interesting to note that crack initiation is dependent on the applied mean stress. As the mean stress increases, the number of cycles to initiate a crack decreases. The crack initiation data will be used in the next chapter to examine the accuracy of methods for predicting the number of cycles needed to initiate a crack from a notch.

Figures 5.7 and 5.8 show the experimental results of the crack propagation for the 1018 and HY-180 steels respectively. Figure 5.7 presents the plot of the crack growth rate (da/dN) versus the stress intensity factor range (ΔK) on log-log paper for 1018 steel. The data were obtained using a load ratio of 0.1 (R = min load/max load) and a frequency of 20 HZ. A similar plot was also obtained for the HY-180 steel (Figure 5.8). The load ratio and frequency used to determine the da/dN vs. ΔK curve for the HY-180 steel were 0.1 and 10 HZ. The $\Delta a/\Delta N$ values were obtained by dividing the grid line spacing (0.02 inch) by the number of

cycles required to propagate the crack 0.02 inch. The corresponding ΔK values were calculated using the average crack length in equation A.1 (see appendix). From Figures 5.7 and 5.8, Paris' expression describing crack propagation behavior for stage B can be obtained for both 1018 and HY-180 steels.

$$\frac{da}{dN} = 2.31\times10^{-12}\,(\Delta K)^{4.45} \qquad \text{for 1018 steel}$$

$$\frac{da}{dN} = 9.8\times10^{-9}(\Delta K)^{2} \qquad \text{for HY-180 steel}$$

where da/dN is in inches per cycle and ΔK in ksi-in$^{\frac{1}{2}}$.

It is interesting to compare the above expressions for crack propagation rate to Barsom's results given in Chapter IV. For convenience, Barsom's generalized equations for crack propagation rates in steels are given below

$$\frac{da}{dn} = 6.6\times10^{-9}(\Delta K)^{2.25} \qquad \text{for tempered-martensite steels}$$

$$\frac{da}{dn} = 3.6\times10^{-10}(\Delta K)^{3} \qquad \text{for ferrite-pearlite steels}$$

Note that the crack propagation rate of HY-180 steel agrees reasonably well with the results obtained by Barsom for tempered-martensite steels. However, the crack propagation rate of 1018 steel obtained in this investigation is not in agreement with his results for ferrite-pearlite steels. Therefore, one should be cautioned against such generalizations of crack propagation rates given in the literature,

especially in dealing with low strength steels.

For comparison purposes, Figures 5.7 and 5.8 were superimposed and this is shown in Figure 5.9. It appears that the crack growth rate is higher in the higher strength steel (HY-180) than in lower strength steel (1018) when the ΔK values fall below 30 ksi-in$^{\frac{1}{2}}$. On the other hand, as the value of ΔK exceeds 30 ksi-in$^{\frac{1}{2}}$, the situation is reversed. It is unexpected and one of the interesting aspects of crack propagation that a material with about four and a half times the yield strength of ordinary steel (1018) shows higher crack propagation rates for the low range of ΔK values.

As pointed out by Lindley et al (56), the exponent n decreases as the fracture toughness increases. Figure 5.10 shows the results from several authors on the variation of n with K_{Ic} in different materials. Note that the exponent n is approximately constant (n = 2) for materials with fracture toughness higher than 100 MNm$^{-3/2}$ (91 ksi-in$^{\frac{1}{2}}$). The steep slopes (n > 3) occur in materials with low fracture toughness ($K_{Ic} \leq 50$ MNm$^{-3/2}$).

It is understood that as the temperature increases, so does the ability of a material to absorb energy (impact Charpy energy), which in turn results in higher K_{Ic} values. Therefore, to further study the variation of n with K_{Ic}, an experiment was conducted on 1018 steel at a temperature higher than room temperature. The high test temperature was

achieved by mounting a heat lamp close to the specimen. The temperature measured on the surface varied by 20°F from one side to the other. A test temperature of 185°F was considered as the average temperature. Figure 5.11 shows the effect of temperature on the crack growth rate of 1018 steel with applied load ratio of 0.1 and cyclic frequency of 120 cpm. The power law for the crack growth rate can be written:

$$\frac{da}{dN} = 1.88\times10^{-10}(\Delta K)^{2.93}$$

The crack growth rate is lower at 185°F temperature than at room temperature for 1018 steel. Also, note that the exponent n has dropped from 4.45 at room temperature to 2.93 at 185°F temperature. The improvement of the crack propagation rate of 1018 steel at 185°F temperature can be attributed partially to the reduction of moisture due to the high temperature. However, the increase in fracture toughness should be considered as the main factor in decreasing the crack propagation rate. This confirms Lindley and coworkers' conclusion that the exponent n decreases as the fracture toughness increases. It is interesting to note that the crack propagation rate obtained at 185°F for 1018 steel agrees reasonably well with Barsom's results for ferrite-pearlite steels. This leads one to believe that the generalization of crack propagation rate offered by Barsom holds true for steels with relatively high fracture

toughness ($K_{Ic} > 50\ MNm^{-3/2}$).

Scanning electron microscopy (SEM) was used to examine the fracture surfaces of 1018 steel at different test temperatures (70°F and 185°F) and HY-180 steel at room temperature. The photographs of the fracture surfaces for 1018 steel are shown in Figures 5.12 and 5.13. Examination of the fracture surfaces of the 1018 steel specimen tested at room temperature (Figure 5.12) and 185°F temperature (Figure 5.13) revealed regions of ductile striation growth during fatigue. However, it was not possible to determine the fraction of the surface over which striations occurred. The change in the crack growth rates of 1018 steel at room temperature and 185°F may be due to the increase in fracture toughness with temperature with a consequent decrease in static fracture modes.

Figure 5.14 shows photographs of the fracture surface of HY-180 steel. The striation patterns are not easily visible. However, at higher magnification, local regions of striations are observed (Figure 5.14b).

To study the effect of the applied load frequency, tests were conducted at different cyclic frequencies with the same load ratio. Figure 5.15a shows the plot of the crack propagation rate vs. the stress intensity factor range for 1018 steel obtained using three different frequencies of 10, 120 and 1200 cycles per minute (cpm) with the applied

load ratio kept constant (0.1) for the three tests. Figure 5.15b shows the same plot for HY-180 steel at cyclic frequencies of 15, 60 and 600 cpm with an applied load ratio of 0.2. It appears from Figure 5.15 that the cyclic frequency has little effect on the crack propagation rate of the steels used in this investigation. In fact, other investigators have also shown this ineffectiveness of cyclic frequency variation on growth rate for numerous steels. The fact that the experimental results show that the cyclic frequency has little effect on crack growth rate is not surprising since at low and high frequencies the crack tip opening for a given external load is the same. In other words, the length of the fresh surface created at each cycle is the same assuming that the environment is non-corrosive. And, since the crack propagation mechanism involves shear decohesion of the material at the tip of the crack during the tension part of the cycle (Chapter III), which depends on the amount of fresh surface created at each cycle, one should expect little effect of frequency on crack growth rate.

The effect of mean stress on the fatigue crack propagation rate was also studied. Figures 5.16a and b show the experimental results obtained using different mean stresses for 1018 and HY-180 steels respectively. The tests were performed using both 1018 and HY-180 specimens, with applied

load ratio of 0.1, 0.2, and 0.4. The test results for both steels fall within a very small scatter band, thus indicating that the effect of mean stress on crack propagation can be considered negligible in an air environment. The results could be attributed to the fact that the mechanism of crack propagation was governed only by the striation mode of fatigue failure. In other words, there was no contribution from the static modes of fatigue failure (cleavage, intergranular, etc.).

2 - Salt Water Environment Tests

For the corrosion fatigue experiments a solution of 3% NaCl dissolved in distilled water was used. A rotary pump was used to circulate the salt water solution around the crack. During the experiments the corrosive solution was periodically circulated through the chamber from a 1.5 gallon reservoir in order to minimize the variation in test conditions. As was the case in the air environment experiments, the corrosion tests were performed under a constant amplitude load of sinusoidal shape in tension-tension conditions. No difficulty was encountered in observing the crack and grid lines through the salt water solution.

Figures 5.17a and b present the experimental results of crack growth rate in corrosive environment applying different cyclic frequencies. Figure 5.17a shows the growth rate data obtained for HY-180 steel at frequencies of 600,

60, and 15 cycles per minute. Note that at the high frequency of 600 cpm there is no difference between the crack growth rate in air and salt water environment. But as the frequency of the applied load decreases, the effect of corrosion on fatigue growth rate becomes more pronounced. At 15 cpm the crack growth rate in salt water is about 1.5 to 2 times that in an air environment. A similar plot for the crack growth rate of 1018 steel in corrosive environment is shown in Figure 5.17b. The tests were performed under applied cyclic frequencies of 600, 120, and 10 cycles per minute. Again it appears that the growth rate approaches that of air as the frequency increases. The crack growth law for both materials can be written as follows:

$$\frac{da}{dN} = 4.15\times10^{-12}(\Delta K)^{4.42} \qquad \text{for 1018 steel in salt water, f=10 cpm}$$

$$\frac{da}{dN} = 5.53\times10^{-8}(\Delta K)^{1.72} \qquad \text{for HY-180 steel in salt water, f=15 cpm}$$

It is reasonable to assume that the electrochemical reaction that takes place at the tip of the crack is similar for different frequencies. However, the corrosion reaction has lesser effect for high frequencies than low due to the lack of interaction time.

Since the slope of the crack growth rate (in salt water) remains approximately constant and the constant C

varies with different frequencies, the crack growth law can be formulated as:

$$\frac{da}{dN} = C(f,(\Delta K)^n$$

where C(f) is a function of cyclic frequency. Figures 5.18 and 5.19 show the plot of C(f) vs. test frequency on log-log paper for 1018 and HY-180 steels respectively. The linear behavior suggests that the data in Figures 5.18 and 5.19 can be used to predict the value of C(f) for any frequency between 10 to 600 cpm providing that the same environment-material system is studied. It is interesting to note that the slope of the graphs presented in Figures 5.18 and 5.19 are the same. It would be interesting to study if the slope of the plot of C(f) vs. test frequency, which shows the effect of frequency on crack growth rate in salt water solution, remains constant for steels regardless of the yield strength.

Also studied in this investigation was the effect of mean stress on fatigue crack growth rate in a corrosive environment. The 1018 steel specimens were tested in 3% solution of sodium chloride with a frequency of 10 cpm and an applied load ratio of 0.1 and 0.4. The HY-180 steel specimens were also tested in 3% solution of sodium chloride but with a cyclic frequency of 60 cpm and an applied load ratio of 0.2 and 0.4. The experimental results are shown in

Figures 5.20a and b. In the case of both steels, the crack propagation rate increased as the mean stress increased. This behavior could be attributed to the fact that at the higher load ratio, the region around the crack tip becomes more anodic due to the plastic deformation. Thus, a higher dissolution rate of metal takes place at the crack tip resulting in a higher crack propagation rate.

Aside from the cyclic frequency and mean stress, other factors, such as cyclic load wave-form and metallurgical variables to name a few, also influence the crack propagation rate of a steel in a corrosive environment. Therefore, due to the complexity of the situation, one cannot include the effect of all the variables in the power law expression to describe the fatigue crack growth behavior of steels in an aggressive environment. However, one can state that the crack growth rate increases as the frequency decreases and stress ratio increases. The worst case being when a specimen is tested in a corrosive environment with a high load ratio and a low applied cyclic frequency.

3 - Cathodic Protection Tests

Cathodic protection was achieved by impressing an external current through the specimen. Steels immersed in salt water usually require a current density of about 15 mA per sq. ft. for cathodic protection (Table 4.1). Using this knowledge, the current needed to sufficiently protect the

specimen was calculated to be 0.21 mA. The positive terminal of the 1.5 volt dry cell battery was connected to the corrosion chamber (used as anode) and the negative terminal connected to the specimen (cathode) through a variable resistor. Care was taken so that no part of the chamber would come in contact with the specimen. The chamber was separated from the specimen by the O-rings and insulating paint was used on the bottom of the chamber. The bolts were jacketed in plastic tubes to further assure that no connection between the chamber and the specimen was made. The freely corroding potentials were measured to be 610±20 mV and 300±20 mV for 1018 and HY-180 steels respectively. After applying the external current, the potentials were measured to be 940±10 mV and 660±20 mV for 1018 and HY-180 steels. The current and the potential were controlled by the variable resistor in the circuit. Figures 5.21a and b show the experimental results obtained for cathodically protected specimens. The results indicate that for both materials the crack propagation rate actually increased when the specimens were cathodically protected. As was explained in Section E of Chapter IV, by impressing external current to protect the metal, the reaction rate at the cathode (metal) increases. The increase in reaction rate causes hydrogen ions to evolve at a faster rate. Therefore it is reasonable to suggest that the increase in the crack growth rate of the specimens tested under cathodic protection is

caused by the more intense interaction between hydrogen and the metal at the crack tip. Since high strength steels are more susceptible to hydrogen embrittlement than low strength steels, this could explain why cathodic protection effects the crack growth rate of HY-180 steel more than the growth rate of 1018 steel.

It should be mentioned that during the cathodic protection testing, the surface of the specimen was observed to be free of corrosion deposits. This suggests that cathodic protection can be used successfully to increase the initiation life. But, the fatigue crack growth rate is actually increased when cathodic protection is applied.

The effect of cathodic protection on fatigue strength and crack propagation rate depends greatly on the material-environment system, applied external current (or voltage), and the pH of the solution. It is agreed in the literature that the fatigue endurance limit in the presence of salt water environment can be increased to that of air by protecting the metal cathodically. For example, Nishioka et al (91) showed that the endurance limit of SS41 (σ_y = 44 ksi) which was reduced in salt water was restored to the value found in air when cathodic protection was applied. But they pointed out that at very low cycles (6 cpm) the endurance limit was not completely restored to that in air in the presence of cathodic protection. However, the endurance

limit did improve from the value obtained in 3% salt water with no cathodic protection. Since about 90% of the life of the specimens was spent during the initiation stages, it can be stated that cathodic protection helps to relieve the effect of corrosion during fatigue crack initiation.

Duquette and Uhlig (92) also showed that the endurance limit can be improved in corrosive solutions of low and high pH. However, they indicated that at low pH (acidic solution) higher current density is required to achieve successful protection and that the current should be adequately distributed throughout the specimen. Therefore as the pH of a solution decreases, the applied potentials should be increased for successful cathodic protection.

In this investigation cathodic protection was found to increase the crack growth rate although not by the same amount for the two materials tested. Vosikovsky (93) tested X-65 line-pipe with yield strength of 66.5 ksi in 3.5% NaCl solution and an applied potential of -1040 mV. He observed that the growth rate increased slightly compared to that of free corrosion at 60 cycles per minute. But, at lower cyclic frequencies (6 and .6 cpm), cathodic protection caused the crack growth rate to increase dramatically. In the worst case, the growth rate was found to be 50 times that of air for applied cathodic protection as compared to 10 times that of air for free corrosion. Vosikovsky's

results seem to be beyond the range observed by others. One reason for the results could be that the specimen was over-protected. In other words, the applied potential of -1040 mV is higher than the potential of -850 to -950 mV needed for sufficient protection. The higher the potential, the higher the cathodic reaction thus resulting in evolving more hydrogen molecules. Moreover, the test frequency used was very low (.6 cpm).

Recently, Crooker (94) studied the effect of cathodic protection on the fatigue crack growth rate of several high strength marine alloys. He tested steels, titanium and aluminum specimens in natural sea water and a frequency of 30 cpm. Crooker also confirmed the results obtained in this investigation. The steel specimens showed an increase in crack growth rate at applied potentials of -1050 mV. He also tested HY-130 steel specimens at a frequency of 1 cpm with cathodic potentials applied. Crooker observed that the growth rate was 4 times that of free corrosion at 1 cpm and 2 times that of free corrosion at 30 cpm. Again one can see that the applied cyclic frequency not only effects the free corrosion growth rate but also has an effect when cathodic potential is applied. The responses of titanium and aluminum alloys to free corrosion and cathodic potentials were completely different from that of steels. Titanium alloys showed very little effect of free corrosion or applied

cathodic potentials on fatigue crack growth rate. Aluminum alloys showed a slight increase in the crack growth rate at free corrosion but the application of cathodic potentials reduced the crack growth rate back to that of air.

Jaske et al (95) also studied the effect of cathodic protection on ABS DH 32 steel tested in sea water at frequencies of 10 to 600 cpm. The applied potentials were -950 and -1000 mV. They concluded that below ΔK = 15 ksi the applied potential increases the crack growth rate but between ΔK = 15 to 20 ksi, the applied cathodic potential appears to be beneficial and decreases the crack growth rate as compared to that of free corrosion. However, all of the data reported by Jaske et al fell below ΔK = 25 ksi and if the curves are extrapolated linearly, it becomes evident that the applied potential causes the crack growth rate to increase relative to the growth rate for free corrosion.

It appears that more investigations are needed for a better understanding of the effect of cathodic protection on the crack growth rate of materials. The studies should include such factors as cyclic frequency and applied cathodic potentials. For now as a generalization for steels it seems that crack initiation (or endurance limit) benefits from cathodic protection but the crack propagation rate increases in the presence of applied cathodic potential.

VI - CRACK INITIATION PREDICTION

In this chapter two methods for predicting the number of cycles required to initiate a crack from a notch are discussed. The first method deals with the resistance of a metal to total strain cycling. The total strain can be considered as the summation of elastic strain and plastic strain. Neuber's rule is also used to account for the notch effect on crack initiation. The second method relates the number of cycles to initiate a crack to the stress intensity factor at the notch. The relationship is in the form of a power law similar to Paris' law for crack propagation.

A - Initiation Prediction Using Total Strain Approach

The fatigue resistance of a metal can be divided into three categories. 1) Long lives which can be described on a stress basis, 2) Short lives that are best described by using the plastic strain approach, and 3) Intermediate lives which can be described by using the total strain approach. The main difference between the categories mentioned above is that the cyclic stress resistance (long lives) is determined by the metal's strength while the plastic strain resistance (short lives) is dependent on its ductility. The resistance of metal to total strain cycling can be

considered as the summation of elastic strain resistance (fatigue strength) and plastic strain resistance (fatigue ductility).

1 - Stress Resistance (long lives)

The relation between stress amplitude, σ_a, and the number of cycles to failure in smooth bar tests, N_f, is given by the following equation.

$$\sigma_a = \sigma_f' (N_f)^b \tag{6.1}$$

where σ_a is the fatigue strength, σ_f' is the fatigue strength coefficient, and b is the fatigue strength exponent. Therefore, a metal's stress cycling resistance can be described by σ_f' and b which are considered fatigue strength properties. If σ_a is plotted against N_f on log-log paper, then the fatigue strength σ_f' is the intercept at one cycle, and the fatigue strength exponent b is the slope of the line.

The fatigue strength coefficient is approximately equal to the true fracture strength found in a tensile test (96). Other investigators have proposed alternative methods of approximating the fatigue strength coefficient from the true fracture strength. These methods are summarized in Table 6.1 (96-99). Figure 6.1 shows data for several representative metals which further confirms the close agreement between the fatigue strength coefficient and the true frac-

ture strength. As a rule of thumb for steels in the low and intermediate hardness range (less than 500 BHN) one can approximate σ_f' as follows.

$$\sigma_f' \approx S_u + 50000 \quad \text{(psi)}$$

where S_u is the ultimate tensile strength.

It should be noted here that the true fracture strength should be corrected for constraints due to the necking before the value of the fatigue strength coefficient is approximated. The correction can easily be made by using Bridgman's analysis of stress behavior at the neck. According to Bridgman's analysis this can be written (100):

$$\sigma_f(\text{corrected}) = \sigma_f(\text{uncorr.}) \left[\frac{1}{(1+\frac{2R}{a})\ln(1+\frac{a}{2R})} \right] \qquad (6.2)$$

where σ_f is the true fracture strength, R is the neck contour radius and 2a is the specimen diameter at the neck.

Reported values of the fatigue strength exponent b range from -0.05 for certain high strength alloys to -0.15 for annealed metals (101,102). Morrow (103) using an energy argument has shown that b is related to the cyclic strain hardening exponent, n', as follows:

$$b = -\frac{n'}{1+5n'} \qquad (6.3)$$

The experimental data are in good agreement with the values

of b found using equation 6.3 (Figure 6.2). As a general rule if the metal is in the soft condition, b is approximately -0.1, and if the metal has been hardened by cold working, b approaches the value of -0.05. For most metals the fatigue strength exponent can be approximated as follows (103):

$$b = -\frac{1}{6}\log(2\frac{\sigma_f}{S_u}) \tag{6.4}$$

where σ_f is the corrected true fracture strength and S_u is the ultimate strength.

The effect of mean stress can be introduced into the equation (6.1).

$$\sigma_a = (\sigma_f' - \sigma_m)(N_f)^b \tag{6.5}$$

where σ_m is the mean stress. A tensile mean stress thus reduces the fatigue strength coefficient, and a compressive mean stress increases the fatigue strength coefficient. Equation 6.5 can be rearranged as follows:

$$N_f = (\frac{\sigma_a}{\sigma_f' - \sigma_m})^{\frac{1}{b}} \tag{6.6}$$

2 - Plastic Strain Resistance (short lives)

Either cyclic hardening or softening can happen under cyclic plastic strain conditions, depending on the initial

state and test conditions. In general, annealed metals exhibit cyclic hardening and heavily cold-worked metals exhibit cyclic softening. The Manson-Coffin law relating the plastic strain amplitude to cycles to failure is of the form

$$\frac{\Delta\varepsilon_p}{2} = \varepsilon_f' (N_f)^c \tag{6.7}$$

where $\frac{\Delta\varepsilon_p}{2}$ is the plastic strain amplitude, N_f is the number of cycles to failure, ε_f' is the fatigue ductility coefficient, and c is the ductility exponent. The latter two quantities are considered fatigue ductility properties.

No general agreement has been found between investigators as to the relationship between ε_f' and the true fracture ductility coefficient ε_t. However for the majority of materials letting $\varepsilon_f' = \varepsilon_t$ is a good approximation. Therefore, the fatigue ductility coefficient can be approximated by using the following expression.

$$\varepsilon_f' \approx \varepsilon_t = \ln\left(\frac{100}{100-\%RA}\right) \tag{6.8}$$

where RA stands for reduction of area.

For ductile metals the value of the fatigue ductility exponent, c, is nearly a universal constant. The value of c seems to be ranging from -0.5 to -0.7, with c = -0.6 taken as a representative value. In general c tends to decrease in magnitude with increasing ductility. Morrow (103) has

related the fatigue ductility exponent to the cyclic strain hardening exponent to account for variations in c:

$$c = -\frac{1}{1+5n'} \tag{6,9}$$

where n' is the cyclic strain hardening exponent.

3 - Total Strain Resistance (intermediate lives)

In many structural components the material at the critical location (a notch root, the surface of a bending member) is subjected to essentially strain cycling conditions due to the constraint of surrounding elastic material. Therefore, it is reasonable to apply total strain approach to study the fatigue behavior of a component when both elastic and plastic strains are present.

The fatigue strength and fatigue ductility properties that have been mentioned in Sections 1 and 2 can be used to determine the total strain which depends on the combined strength and ductility of the metal. Equation 6.1 can be rewritten in terms of elastic strain.

$$\sigma_a = \varepsilon_a E = \sigma_f' (N_f)^b \tag{6.10}$$

Since $\varepsilon_a = \frac{\Delta\varepsilon_e}{2}$, the elastic strain amplitude $\frac{\Delta\varepsilon_e}{2}$ can be obtained in terms of the fatigue strength coefficient, fatigue strength exponent, and the fatigue life:

$$\frac{\Delta\varepsilon_e}{2} = \frac{\sigma_f'}{E}(N_f)^b \qquad (6.11)$$

But for total strain we have

$$\frac{\Delta\varepsilon}{2} = \frac{\Delta\varepsilon_e}{2} + \frac{\Delta\varepsilon_p}{2} \qquad (6.12)$$

where $\Delta\varepsilon_e$ and $\Delta\varepsilon_p$ are elastic and plastic strain ranges respectively. Substituting equations 6.7 and 6.11 into equation 6.12, the expression for total strain can be obtained.

$$\frac{\Delta\varepsilon}{2} = \frac{\sigma_f'}{E}(N_f)^b + \varepsilon_f'(N_f)^c \qquad (6.13)$$

Figure 6.3 shows a schematic representation of equation 6.13. It is clear that for short lives the plastic strain term dominates whereas for long lives the elastic strain term is the dominant one. Equation 6.13 is most useful in dealing with intermediate lives where the elastic and plastic strains are of the same order.

The transition life, N_t, is obtained by substituting $\Delta\varepsilon_e = \Delta\varepsilon_p$ into equation 6.13.

$$\frac{\sigma_f'}{E}(N_t)^b = \varepsilon_f'(N_t)^c$$

after simplifying

$$N_t = \left(\frac{E\varepsilon_f'}{\sigma_f'}\right)^{\frac{1}{b-c}} \qquad (6.14)$$

It is interesting to note that the transition life increases as the strength of the material decreases and visa versa.

Transition life ranges from 10^5 for low hardness metals to 10 for highest hardness.

4 - Notch Effect

The discussion in previous sections applies only to smooth components, but in most practical cases fatigue failure nearly always starts at the root of a notch. Since notches are not completely unavoidable in design their effects on fatigue behavior have to be considered.

The theoretical stress concentration factor, K_t, applies only when the material at the notch root remains elastic. To account for the local plastic deformation occurring at the notch root Neuber (104) analyzed a specific notch geometry and loading to derive an approximate rule of the form:

$$K_t = (K_\sigma K_\varepsilon)^{\frac{1}{2}} \qquad (6.15)$$

where K_σ, K_ε are stress and strain concentration factors respectively. Neuber's equation can be expressed in terms of local and nominal stresses and strains.

$$K_t = \left(\frac{\Delta\sigma}{\Delta S} \frac{\Delta\varepsilon}{\Delta e} \right)^{\frac{1}{2}}$$

where

ΔS and Δe are nominal stress and strain ranges applied

to a notched member

and

$\Delta\sigma$ and $\Delta\varepsilon$ are local stress and strain ranges at the notch root.

After yielding occurs at the notch root, the strain concentration factor K_ε increases while the stress concentration factor K_σ decreases.

5 - Prediction of Crack Initiation Using Total Strain Approach

Since the number of cycles during the crack propagation stage is very small compared to the cycles during the crack initiation stage for smooth specimens, the assumption that the total strain approach can be used to predict crack initiation seems reasonable. Of course the total strain has to be corrected for the plastic deformation that occurs at the notch root. In order to compare the theoretical curve obtained using equation 6.13 to experimental data (total strain vs. number of cycles to failure), it is convenient to express K_ε and K_σ in terms of fatigue and transition life. Neuber's rule can be rewritten as follows:

$$K_\sigma = K_t\left(\frac{K_\varepsilon}{K_\sigma}\right)^{-\frac{1}{2}}$$

where K_ε and K_σ are defined as in equation 6.15. Therefore we can write:

$$K_\sigma = K_t \left(\frac{\Delta\varepsilon/\Delta e}{\Delta\sigma/\Delta S} \right)^{-\frac{1}{2}}$$

But for most engineering cases the nominal (applied) stress is less than the yield strength. Consequently the material away from the notch behaves elastically. Therefore the above equation can be written as follows:

$$K_\sigma = K_t \left(\frac{\Delta\varepsilon}{\Delta\sigma} E \right)^{-\frac{1}{2}} \tag{6.16}$$

where E is the elastic modulus.

Substituting equations 6.13 and 6.1 into equation 6.16, we can write

$$K_\sigma = K_t \frac{\sigma_f'/E(N_i)^b + \varepsilon_f'(N_i)^c}{\sigma_f'(N_i)^b} E \Bigg)^{-\frac{1}{2}}$$

After simplifying

$$K_\sigma = K_t \left(1 + \frac{E\varepsilon_f'}{\sigma_f'} (N_i)^{c-b} \right)^{-\frac{1}{2}} \tag{6.17}$$

Introducing transition life N_t (eq. 6.14):

$$K_\sigma = K_t \left(1 + \left(\frac{N_i}{N_t} \right)^{c-b} \right)^{-\frac{1}{2}} \tag{6.18}$$

Following the same steps, the corresponding expression for K_ε is

$$K_\varepsilon = K_t \left[1 + \left(\frac{N_i}{N_t} \right)^{c-b} \right]^{\frac{1}{2}} \qquad (6.19)$$

For 1018 steel, with the tensile properties given in Table 5.2 and true fracture ductility coefficient $\varepsilon_t = 1.08$, the fatigue strength and ductility properties are as follows

fatigue strength coefficient, $\sigma_f' = 115$ ksi

fatigue strength exponent, $b = -0.09$

fatigue ductility coefficient, $\varepsilon_f' = 1.08$

fatigue ductility exponent, $c = -0.60$

Therefore, equation 6.13 becomes

$$\frac{\Delta\varepsilon}{2} = .00383(N_i)^{-.09} + 1.08(N_i)^{-.6} \qquad (6.20)$$

Table 6.2 presents the crack initiation data for 1018 steel. The nominal stress values, $\Delta\sigma_N$, for the compact tension specimen were calculated by treating the uncracked ligament as a beam subjected to bending and direct tension. The "outer fiber" stress (i.e. at the crack tip) may be shown (105) to be:

$$\Delta\sigma_N = \frac{\Delta P}{B(W-a)} \left[1 + 3 \frac{W+a}{W-a} \right] \qquad (6.21)$$

where ΔP is the applied load range, W is the specimen width measured from the centerline of loading, a is the notch depth also measured from the centerline of loading, and B is the specimen thickness. The generalized stress intensity

expression which shows the effect of blunt notches on K_I is given by (106)

$$\Delta K_I = \lim_{\rho \to 0} \Delta\sigma_{max} \sqrt{\rho} \frac{\sqrt{\pi}}{2} \tag{6.22}$$

where ρ is the notch radius.

As ρ approaches zero equation 6.22 becomes:

$$\Delta K_I = \frac{\sqrt{\rho\pi}}{2} \Delta\sigma_{max}$$

or

$$\Delta\sigma_{max} = \frac{2\Delta K_I}{\sqrt{\rho\pi}} \tag{6.23}$$

Equation 6.23 can also be obtained from equation 3.16 by substituting $\theta = 0$ and $r = \frac{\rho}{2}$. Equation 6.23 is considered exact only when ρ approaches zero. But Wilson and Gabrielse (107) used finite element analysis of blunt notches in compact tension specimens and showed that equation 6.23 is accurate within 10% for notch radius up to 0.180 inch. The accuracy approaches 4% for notches smaller than 0.04 inch.

The stress intensity range, ΔK_I, can be determined from the crack-notch stress intensity expression for a compact tension specimen (see appendix).

$$\Delta K_I = \frac{\Delta P}{B\sqrt{W}} f\left(\frac{a}{W}\right)$$

where $f(\frac{a}{W})$ is a function of specimen geometry and is described in the appendix. After calculating $\Delta\sigma$ using equation 6.23, the elastic stress concentration values (K_t) given in Table 6.2 were obtained from $\Delta\sigma_{max}$ divided by $\Delta\sigma_N$.

The total strain at the notch was determined from equation 6.19. The effect of mean stress was accounted for by correcting the fatigue strength coefficient σ_f'. Table 6.3 shows the crack initiation data for 1018 steel and the corresponding plot is presented in Figure 6.4. The solid line in Figure 6.4 represents the theoretical curve of total strain vs. number of cycles to initiate a crack. It is apparent from Figure 6.4 that good correlation exists between experimental and calculated values. To confirm this further Clark's experimental data for fatigue crack initiation (108) was also plotted against the theoretical values. Clark in his investigation used 1-inch thick compact tension specimens with various notch radii. Table 6.4 presents the experimental data for 403 stainless steel. The theoretical curve of total strain for 403 stainless steel with σ_u = 110.5 ksi and RA% = 68.4 was obtained using the following expression:

$$\frac{\Delta\varepsilon}{2} = 0.00535(N_i)^{-0.0725} + 1.15(N_i)^{-0.625}$$

The fatigue strength and ductility properties were obtained by using the equations described in the previous sections.

Figure 6.5 shows the theoretical and experimental values plotted on the same graph. Again it appears that good agreement between experimental and theoretical results exist. Therefore, the fatigue crack initiation life of a notched component can be predicted reasonably accurate by knowing the tensile properties of the material. To predict the crack initiation life using the total strain method one has to combine equations 6.13 and 6.19. The resultant equation is as follows:

$$K_\epsilon \frac{\Delta e}{2} = \frac{\sigma_f'}{E} (N_i)^b + \epsilon_f' (N_i)^c$$

or

$$K_t \left[1 + \left(\frac{N_i}{N_t}\right)^{c-b}\right]^{\frac{1}{2}} \frac{\Delta e}{2} = \frac{\sigma_f'}{E} (N_i)^b + \epsilon_f' (N_i)^c \qquad (6.24)$$

where Δe is the nominal strain range. Equation 6.24 should be solved for N_i using a trial and error method.

Applying K_ϵ directly to the smooth bar data to predict fatigue life of a notched specimen usually results in a very conservative life prediction. This could be attributed to the fact that two stages are involved in failure - crack initiation and propagation. Once the crack has started the notched and unnotched specimens behave about the same. Therefore, it seems more realistic to apply K_ϵ to smooth bar strain amplitude and then use equation 6.13 to predict

fatigue crack initiation life rather than failure life.

An interesting application of crack initiation prediction would be in problems dealing with arresting a propagating crack. An existing crack propagating through a component can be stopped by drilling a hole in front of the crack path thereby temporarily delaying the failure of the component. The total strain method explained in this section could be applied to predict the number of cycles needed to reinitiate the crack.

B - Stress Intensity Approach to Crack Initiation

Since the crack propagation rate can be expressed in terms of the stress intensity factor, it would be useful to a designer to also relate the crack initiation life to the stress intensity factor. Crack initiation at the notch is controlled by the local stress and strain. For notches, the maximum local stress is related to the stress intensity factor. This relationship is shown in equation 6.23. Therefore, it would be reasonable to relate the number of cycles to initiate a crack to the stress intensity factor and the radius of the notch. The $\Delta K/\sqrt{\rho}$ for 1018 steel were plotted against the number of cycles to initiation on log-log paper. The resulting graph is shown in Figure 6.6. The data presented in Figure 6.6 show that $\Delta K/\sqrt{\rho}$ is related to the number of cycles to initiate a crack by an expression of the

form:

$$N_i = \beta \left(\frac{\Delta K}{\sqrt{\rho}} \right)^{-\alpha} \qquad (6.25)$$

where β and α are constants for a given material. Figure 6.7 presents the plot of $\Delta K/\sqrt{\rho}$ as a function of N_i for various steels. Again it appears that the data can be expressed by equation 6.25.

For design purposes it would be helpful to obtain the behavior pattern of both α and β as a function of tensile properties. For this reason, taking data from the literature, α and β were plotted against yield strength on log-log paper as shown in Figures 6.8 and 6.9 respectively. It is interesting to note that α increases linearly as the yield strength increases to the value of 60 ksi. But for materials with yield strength greater than 60 ksi the value of α is nearly constant. Therefore, an empirical expression relating α to the yield strength of steels can be formulated as follows

$$\alpha = 0.221(S_y)^{0.82} \qquad \text{for } S_y \leq 60{,}000 \text{ psi} \qquad (6.26)$$

$$\alpha = 6.5 \text{ to } 6.8 \qquad \text{for } S_y > 60{,}000 \text{ psi}$$

The data presented in Figure 6.9 also suggests a linear variation of β with respect to yield strength. However, the graph seems to be divided into two straight lines, one for materials having yield strength below 60 ksi and the other

(higher slope) covering materials with yield strength greater than 60 ksi. As was the case with α, an empirical expression describing β in terms of the yield strength of steels can also be formed

$$\beta = 1.12\times10^{-19} (S_y)^{20.8} \qquad \text{for } S_y \leq 60{,}000 \text{ psi} \qquad (6.27)$$
$$\beta = 4.275\times10^{9} (S_y)^{4.64} \qquad \text{for } S_y > 60{,}000 \text{ psi}$$

Therefore, with tensile properties given and provided that the stress intensity can be obtained at the notch, the elapsed number of cycles to crack initiation can be determined using equation 6.25.

Both methods seem to predict crack initiation reasonably accurate, however the stress intensity approach has a disadvantage in that one has to be able to determine the value of the stress intensity factor at the notch. K_I has been tabulated for most notch geometries, but when dealing with complex components it becomes difficult to calculate the value of K_I. Once K_I has been calculated though, equation 6.25 provides a simple and quick estimation of crack initiation. Equation 6.25 however should be generalized to include the effect of mean stress on crack initiation life. The accuracy of the crack initiation prediction using the total strain approach depends on the estimated values of fatigue strength and ductility properties. Therefore, if available, the experimental values of fatigue strength and

ductility should be used in predicting crack initiation. It should be pointed out that in all of the data presented, the crack initiation length was taken to be around 0.01 inch measured either inside the notch for thick specimens or on the surface for thinner specimens.

Table 6.5 presents a comparison between crack initiation prediction methods and experimental data for 1018 steel. Three methods of prediction have been shown. The first two methods have been discussed previously - the total strain and stress intensity factor approaches. Equation 6.24 was used to predict crack initiation life for the total strain approach. For 1018 steel with yield strength of 41 ksi, α and β were obtained from equations 6.26 and 6.27. Once α and β were determined, equation 6.25 was used to obtain the crack initiation life. The third method presented in Table 6.5 utilizes the simple form of the total strain expression suggested by Manson and Coffin. The expression to obtain the crack initiation lives for notched components in Table 6.5 is as follows

$$K_t \frac{\Delta\varepsilon}{2} = \frac{\varepsilon_t}{4N_i^{\frac{1}{2}}} + \frac{S_e}{E} \qquad (6.28)$$

where S_e is the endurance limit.

Crack initiation prediction using the two methods in this section agrees reasonably well with the experimental

values. But the Manson-Coffin expression (eq. 6.28) appears to be conservative in predicting initiation life. This could be have expected since using $\frac{S_e}{E}$ for the elastic strain term is rather conservative.

C - Total Fatigue Life - Crack Initiation and Propagation

In most engineering structures a crack of a certain length can be tolerated without catastrophic failure occurring. For this reason, not only the number of cycles to initiate a crack needs to be known, but also the knowledge of the number of cycles to propagate that crack to the critical value is important. Besides, sometimes very small micro-cracks can exist and go undetected even before a component is put in service. Therefore an engineer encounters two types of crack problems. The first is a crack emanating from a stress raiser such as a notch for which both crack initiation and propagation life has to be considered. The second problem deals with cracks propagating from an existing flaw in a component when only propagation life has to be considered.

Once a crack of a certain length (a_d) has been detected, then Paris' power law can be used to determine the number of cycles required to reach the critical crack length (a_c). Therefore we have

$$\frac{da}{dn} = C(\Delta K)^n$$

or

$$N = \int_{a_d}^{a_c} \frac{1}{C} (\Delta K)^{-n} da \qquad (6.29)$$

The values of stress intensity factors have been tabulated for many crack geometries. For example, K_I for an edge crack in a semi-infinite sheet subjected to tension is given by the following expression

$$K_I = 1.12\sigma(\pi a)^{\frac{1}{2}} \qquad (6.30)$$

where σ is the applied stress and a is the crack length. Substituting equation 6.30 into 6.29, one can obtain the number of cycles to propagate the crack to the critical value.

$$N = \frac{1}{C} \int_{a_d}^{a_c} \left[1.12\Delta\sigma(\pi a)^{\frac{1}{2}} \right]^{-n} da \qquad (6.31)$$

However when a crack is initiated from a notch one has to consider both crack initiation and propagation life.

$$N_T = N_i + N_p$$

where N_i is the number of cycles to initiate a crack (assumed 0.01 inch) and N_p is the number of cycles to propagate the crack to a desired crack length. The number of cycles to initiate a crack from a particular notch can be

approximated by either of the two methods discussed in the previous sections. Therefore a general expression for the total number of cycles to reach the critical crack length including both initiation and propagation can be formulated as follows (assuming the stress intensity factor approach to predict crack initiation)

$$N_T = \beta \left(\frac{\Delta K}{\sqrt{\rho}} \right)^{-\alpha} + \int_{a+a_i}^{a_c} \frac{1}{C} (\Delta K)^{-n} da \qquad (6.32)$$

The expression for ΔK for compact tension specimens is (see appendix)

$$\Delta K = \frac{\Delta P}{B\sqrt{W}} f\left(\frac{a}{W}\right) \qquad (6.33)$$

Substituting equation 6.33 into 6.32 we have:

$$N_T = \left[\beta \frac{\Delta P}{B\sqrt{W\rho}} f\left(\frac{a}{W}\right) \right]^{-\alpha} + \frac{1}{C} \int_{a+a_i}^{a_c} \left[\frac{\Delta P}{B\sqrt{W\rho}} f\left(\frac{a}{W}\right) \right]^{-n} da \qquad (6.34)$$

where the integral in the second term has to be evaluated using numerical integration methods.

A general expression such as the one shown in equation 6.32 cannot be written for the total number of cycles when the total strain approach to predict crack initiation is used. This is due to the fact that N_i cannot be simplified and expressed in terms of fatigue strength and ductility properties. But a simple computer program can be set up to

evaluate N_i. The value of N_i is then added to the second term of equation 6.32 to obtain the total number of cycles.

In equation 6.32, the value of the lower boundary of the integral, $(a+a_i)$, becomes important in evaluating the propagation term. In the present investigation, a_i was assumed to be 0.01 inch and for the compact tension specimen, a is measured from the centerline of the applied load to the tip of the notch (1.0 inch). Therefore $a+a_i$ is of the same order of magnitude as a_c and the effect of assuming different values for a_i would be negligible on the total number of cycles obtained using equation 6.32. This holds true for other notch geometries such as edge-notched components as long as the notch depth is of the same magnitude as the critical crack length. On the other hand, dealing with thumbnail flaws (semi-circular) with small radius (0.05 to 0.2 inch), the effect of different crack initiation lengths on evaluating the integral becomes greater. Therefore it appears that the value of a_i should be standardized for consistency in evaluating and comparing crack initiation and propagation data. The selection of the crack initiation length as 0.01 inch resulted in good agreement between theoretical and experimental data in the present tests.

VII - CONCLUSIONS

The fatigue crack propagation rate in air and salt water environments is described by the power law, $da/dN = C(\Delta K)^n$, for the steels tested in this investigation at cracking rates of 10^{-6} to 10^{-4} inch/cycle. It is interesting to note that the crack propagation rate of HY-180 steel in air is higher than that of ordinary steel (1018) for low values of the stress intensity factor range ($\Delta K < 30$ ksi-in$^{\frac{1}{2}}$). The value of the exponent n for 1018 steel ($n = 4.45$) is two times higher than that of HY-180 steel ($n = 2$) in an air environment. It appears that the exponent n is dependent on the fracture toughness of the material. As the fracture toughness of 1018 steel is improved (higher test temperature), the value of the exponent n decreases ($n = 3$ for test temperature of 185° F).

Some investigators have pointed out that the crack propagation rates of all steels fall within a narrow band in region B (for intermediate values of ΔK). In reference to the studies done in this investigation, which showed a completely different crack propagation rate for HY-180 and 1018 steels, a clarification of such a statement is needed. It is reasonable to state that for steels with fracture toughness greater than 50 ksi-in$^{\frac{1}{2}}$, crack propagation rates for

all steels fall within a narrow band. On the other hand, steels with low fracture toughness show different crack propagation behavior and each case has to be studied individually.

Test frequency and mean stress appear to have negligible effect on the crack propagation rate of HY-180 and 1018 steels tested in an air environment.

In general, corrosive environment (3% NaCl solution) tends to increase the crack propagation rate. The amount of increase depends on the cyclic frequency and the applied mean stress. As the frequency increases, the effect of the salt water solution on the crack propagation rate decreases. As the cyclic frequency is decreased from 600 to 10 cpm, the crack growth rate increases by a factor of 1.5 for 1018 steel and by as much as 2.5 for HY-180 steel. In the case of HY-180, not only the constant C in the growth law varies from that of air but the exponent n decreases from 2 found in air to 1.72 in salt water. Thus the effect of salt water on the crack growth rate of HY-180 decreases as the ΔK increases. On the other hand, the exponent n remains the same in air and salt water for 1018 steel. The variation of C with respect to cyclic frequency is linear on log-log paper.

Mean stress also has an effect on the crack propagation rate in the presence of salt water. The crack propagation

rate for 1018 steel is increased by a factor of 2 when the load ratio is increased from 0.1 to 0.4 at a frequency of 10 cpm. The same behavior is observed for HY-180 steel. Therefore, in designing parts against fatigue in a salt water environment, the applied mean stress should be kept as small as possible.

The applied negative potentials (cathodic protection) appear to have an adverse effect on the crack propagation rate of steels. Both steels show an increase in the crack propagation rate in salt water with cathodic protection. The effect is more severe in the case of HY-180 steel. The cathodic protection has a more pronounced effect on the crack growth rate in the middle range of the ΔK values as compared to the low and high ΔK values in region B. However, applied negative potentials appear to prevent the formation of corrosion deposits on the surface of a metal. Therefore one can state that cathodic protection has a beneficial effect on crack initiation but an adverse effect on crack propagation. If cathodic protection is used to prolong the crack initiation life, a minimum amount of negative potentials should be applied. In this way, once the crack has started, the crack propagation rate will be effected less due to the minimal amount of hydrogen generated at the crack tip.

The number of cycles to initiate a fatigue crack in a

notched specimen can be estimated using the total strain approach, with Neuber's rule applied to the strain amplitude to account for the notch effect. The total strain is considered as the summation of elastic and plastic strains. The accuracy of the total strain approach compared to experimental results ranges from 5% for low crack initiation lives to 19% for high crack initiation lives. On the other hand, since crack propagation rates are related to the range of the stress intensity factor, there is an advantage in a unified treatment of also relating initiation to this quantity.

The number of cycles required to initiate a fatigue crack in a notched specimen can be related to the ratio of stress intensity factor range to the square root of the notch radius, $N_i = \beta(\Delta K/\sqrt{\rho})^{-\alpha}$. The values of α and β are dependent on the tensile properties of a material. The dependence of α and β on the yield strength appears to be divided into two regions - 1) materials with a yield strength lower than 60 ksi, and 2) materials with a yield strength greater than 60 ksi. α increases from 6.5 to 6.8 for materials with yield strength greater than 60 ksi. A representative value for α of 6.65 can be selected for these materials. Both α and β are related linearly to the yield strength of a material on log-log paper. The accuracy of the stress intensity factor approach to crack initiation

prediction is about the same as that of the total strain approach. However the stress intensity factor method is empirical and has to be modified to include the effect of mean stress.

Both of the fatigue crack initiation prediction methods mentioned in this investigation can be combined with the existing crack propagation laws to describe the total fatigue life of a notched part in an air environment. The same crack initiation prediction methods may be used when designing against fatigue in salt water but only if sufficient cathodic protection is applied. However, after the crack has been detected, there may be an advantage in reducing or removing cathodic protection to avoid accelerating the crack growth. Then the total life can be estimated by combining the predicted crack initiation life and the experimentally determined propagation life. If cracks already exist in a part, such as welded structures, then only propagation laws should be used to determine the fatigue life and cathodic protection should be considered with caution.

The arbitrary selection of 0.01 inch as the crack length separating the crack initiation and propagation stages appears to be reasonable. The experimental crack initiation results are in agreement with theoretical results when the initiation crack length is considered as 0.01 inch. However, for crack initiation from blunt notches, other

values for the "initiation crack length" may be more appropriate. From the results of Novak and Barsom (53) it is seen that fracture mechanics can only be applied to cracks growing from blunt notches when they have reached a length $a_i \geq (a\rho)^{\frac{1}{2}}/4$ where a is the notch depth, ρ the notch radius and a_i the length of the initiated crack. In such situations it might be more realistic to take this value for a_i.

REFERENCES

1. Beevers, C.J. and M.D. Halliday, Czech. Journal of Physics 19, Section B, p.343, 1969.

2. Ewing, J.A. and J.E.W. Humphrey, Philosophical Transactions A200, p. 241, 1903.

3. Thompson, N., N.J. Wadsworth, N. Louat, Philosophical Magazine 1, p. 113, 1956.

4. Mott, N.F., Acta Metallurgica 6, p. 195, 1955.

5. Kennedy, A.J., Philosophical Magazine 6, p. 49, 1961.

6. Cottrell, A.H. and D. Hull, Proc. Royal Society A242, p. 211, 1957.

7. McEvily, A.J. and E.S. Machlin, FRACTURE, John Wiley & Sons, Inc., New York, p. 450, 1959.

8. Thompson, N., Int'l. Conference on Atomic Mechanisms of Fracture, Swempscott, Mass., John Wiley & Sons, Inc., New York, 1959.

9. Fujita, F.E., Acta Metallurgica 6, p. 543, 1958.

10. Grosskreutz, J.C., Surface Science 8, p. 173, 1967.

11. McNeil, M.B. and J.C. Grosskreutz, Journal of Applied Physics 38, p. 3310, 1967.

12. Wood, W.A., Int'l. Conference on Atomic Mechanisms of Fracture, Swempscott, Mass., John Wiley & Sons, Inc., New York, 1959.

13. May, A.N., Nature 185, p. 303, 1960.

14. Neuman, P., Acta Metallurgica 17, p. 1219, 1969.

15. Wood, W.A. and H.M. Bendler, Transactions of AIME 224, p. 18, 1962.

16. Kemsley, D.S., Philosophical Magazine 2, p. 131, 1957.

17. Laird, C. and G.C. Smith, Philosophical Magazine 8, p. 1915, 1963.

18. Laird, C., Ph. D. Thesis, University of Cambridge, 1963.

19. Laute, K., Oberfalchentech. 10, p. 281, 1933.

20. Simnad, M.T. and U.R. Evans, Proc. Royal Society A188, p. 372, 1947.

21. Hoar, T.P., Corrosion Science, CRRSA, Vol. 7, p. 341, 1967.

22. Rohni, H. and H.H. Uhlig, Journal of Electrochemical

Society, JESOA, Vol. 116, p. 906, 1970.

23. McAdam, D.J., Jr. and G.W. Gail, Proc. ASTM 41, p. 696, 1928.

24. Simnad, M.T. and U.R. Evans, JISI 156, 1947.

25. Duquette, D.J. and H.H. Uhlig, Transactions of ASM 62, p. 839, 1969.

26. Neuber, H., THEORY OF NOTCH STRESSES, J.W. Edwards, Ann Arbor, Michigan, 1946.

27. Evans, U.R., THE CORROSION OXIDATION OF METALS, Edwards Arnold Ltd., London, p. 681, 1960.

28. Rebunder, P., V. Liktman, and E. Shchukin, Physicochemical Mechanics of Metals, Academy of Sciences, USSR, Israel Program for Scientific Translations, Jerusalem, p. 12, 1964.

29. Benedicks, C., Pittsburgh Int'l. Conference on Surface Reactions, p. 196, 1948.

30. Thompson, N., N.J. Wadsworth, and N. Louat, Philosophical Magazine 1, p. 113, 1956.

31. Shen, H., S.E. Podlaseck, and I.R. Kramer, Acta Metallurgica 14, p. 341, 1966.

32. Bennett, J.A., Journal of Research NBS 68C, p. 91,

1964.

33. Broom, T. and A. Nicholson, Journal of Inst. Metals 89, p. 183, 1960.

34. Wadsworth, N.J. and J. Hutchings, Philosophical Magazine 3, p. 1154, 1958.

35. Hordon, M.J., Acta Metallurgica 14, p. 1173, 1966.

36. Wohler, A., English Abstract in Engineering 11, p. 199, 1871.

37. Weibull, W., FATIGUE TESTING AND ANALYSIS OF RESULTS, p. 174, 1961.

38. Valluri, S.R., GAL CITSM611, 1961.

39. Stulen, F.B., H.N. Cummings and W.C. Schulte, Machine Design, Vol. 33, p. 161, 1961.

40. Juvinall, R.C., STRESS, STRAIN AND STRENGTH, McGraw-Hill, 1967.

41. Miner, M.A., Trans. of ASME, Journal of Applied Mechanics, Vol. 12, p. A159, 1945.

42. Henry, D.L., Trans. of ASME, Vol. 77, p. 913, 1955.

43. Low, A.C., Int'l. Conference on Fatigue, Instr. Mechanical Engineers, p. 206, 1956.

44. Kooistra, L.F., Welding 36, 1957.

45. Coffin, L.F., Applied Material Research 1, p. 129, 1962.

46. Manson, S.S., U.S. National Advisory Committee on Aeronautics, Technical Note 2933, 1954.

47. Griffith, A.A., Philosophical Transactions, Royal Society, London, 221A, p. 163, 1920.

48. Inglis, C.E., Trans. Inst. Naval Architecture, London, 55, part 1, p. 219, 1913.

49. Irwin, G.R., Journal of Basic Engineering, Trans. ASME, Series D, Vol. 82, No. 2, p. 417, 1960.

50. Irwin, G.R., Journal of Applied Mechanics 21, 1957.

51. Creager, M., M.S. Thesis, Lehigh University of Bethlehem, Pa., 1966.

52. Paris, P.C. and G.C. Sih, FRACTURE TOUGHNESS TESTING AND ITS APPLICATION, ASTM STP 381, 1965.

53. Novak, S.R. and J.M. Barsom, CRACKS AND FRACTURE, ASTM STP 601, p. 409, 1976.

54. Laird, C. and G.C. Smith, Philosophical Magazine 8, p. 1945, 1963.

55. Laird, C. and G.C. Smith, Philosophical Magazine 7, p. 847, 1962.

56. Lindley, T.C., C.E. Richards, and R.O. Ritchie, U.S. ERDA Contract W-7045 ENG-48, 1974.

57. Richards, C.E., Acta Metallurgica 19, p. 583, 1971.

58. Ryder, D.A. and P.J.E. Forsyth, Metallurgia 63, p. 117, 1961.

59. Ritchie, R.O. and J.F. Knott, Acta Metallurgica 21, p. 639, 1973.

60. Cooke, R.J., P.E. Irving, G.S. Booth, and C.J. Beevers, Engineering Fracture Mechanics 7, 1975.

61. Cooke, R.J., C.J. Beevers, J.F. Knott and R.O. Ritchie, Metal Science 9, p. 119, 1975.

62. Pelloux, R.M.N., Trans. American Society of Metals 57, p. 511, 1964.

63. Pearson, S., Engineering Fracture Mechanics 4, p. 9, 1972.

64. Ritchie, R.O. and J.F. Knott, Proc. R.S.C. Conference on the Mechanics and Mechanisms of Crack Growth, Cambridge, April 1973.

65. Ritchie, R.O., Ph. D. Thesis, University of Cambridge,

1973.

66. Griffiths, J.R. and C.E. Richards, Material Science Engineering 11, p. 305, 1973.

67. Richards, C.E. and T.C. Lindley, Engineering Fracture Mechanics 4, p. 951, 1972.

68. Garrett, G.G., Ph. D. Thesis, University of Cambridge, 1973.

69. Barsom, J.M., MTS Closed Loop Magazine, Spring 1972.

70. Head, A.K., Philosophical Magazine, Vol. 44, No. 7, p. 925, 1953.

71. Frost, N.E. and D.S. Dugdale, Journal of the Mechanics and Physics of Solids, Vol. 6, No. 2, p. 92, 1958.

72. Irwin, G.R., Journal of Basic Engineering, Trans. ASME, Series D, Vol. 82, No. 2, p. 417, June 1960.

73. Liu, H.W., Journal of Basic Engineering, Trans. ASME, Series D, Vol. 85, p. 116, 1963.

74. Paris P.C., M.P. Gomez, and W.E. Anderson, The Trend in Engineering, Vol. 1, No. 2, p.33, May 1961.

75. Barsom, J.M., Trans. of the ASME, Journal of Engineering for Industry, Series B, Vol. 93, No. 4, Nov. 1971.

76. Frost, N.E. and J.R. Dixon, Int'l. Journal of Fracture Mechanics 3, p. 301, 1967.

77. Frost, N.E. and L.P. Pook, Int'l. Journal of Fracture 9, p. 53, 1973.

78. Forman, R.G., et al, Journal of Basic Engineering 10, p. 459, 1967.

79. Barsom, J.M., ASTM STP 595, p. 217, 1976.

80. Heald, P.T., T.C. Lindley, and C.E. Richards, Material Science Engineering 10, p. 235, 1972.

81. Hoar, T.D. and J.M. West, Proc. Royal Society A268, p. 304, 1962.

82. Kramer, I.R., Trans. AIME 239, p. 520, 1967.

83. Kramer, I.R., ENVIRONMENT SENSITIVE MECHANICAL BEHAVIOR OF MATERIALS, Breach and Gordon, p. 127, 1967.

84. Wadsworth, N.J. and J. Hutchings, Philosophical Magazine 3, p. 1154, 1958.

85. Dahlberg, E.P., Trans. American Society of Metals 58, p. 46, 1956.

86. Mantel, E.R., G.H. Robinson and R.F. Thompson, Metals Engineer Quarterly, American Society of Metals 1, p.

57, 1961.

87. Spitzig, W.A., P.M. Talda and R.P. Wei, Engineering Fracture Mechanics 1, p. 155, 1968.

88. Wei R.P., Journal of Engineering Fracture Mechanics 1, p. 633, 1970.

89. Bradshaw, F.J., N.J.F. Nunn and C. Wheeler, RAE Technical Memo. MAT 93, July 1970.

90. Gallagher, J.P., Journal of Materials, Vol. 6, p. 941, 1971.

91. Nishioka, K., K. Hirakawa, and I. Kitaura, Sumitomo Metal Industries, Ltd., Osaka, Japan, 1976.

92. Duqutte, D.J. and H.H. Uhlig, Trans. of ASM, Vol. 62, p. 839, 1969.

93. Vosikovsky, O., Trans. of the ASME, p. 298, Oct. 1975.

94. Crooker, T.W., F.D. Boger, and W.R. Cares, Naval Research Lab, Aug. 30, 1976.

95. Jaske, C.E., D. Brock, J.E. Slater, D.A. Utah, and C.J. Martin, Battelle, Columbus Labs, Columbus, Ohio, Feb. 11, 1977.

96. Halford, G.R. and J.D. Morrow, Proc. American Society for Testing and Materials, ASTEA, Vol. 62, p. 695,

1962.

97. Manson, S.S., Machine Design, MADEA, p. 153, June 23, 1960.

98. Manson, S.S., Machine Design, MADEA, p. 165, Nov. 23, 1961.

99. Manson, S.S. and M.H. Hirschberg, in FATIGUE: AN INTERDISCIPLINARY APPROACH, Syracuse Univ. Press, Syracuse, N.Y., p. 133, 1964.

100. Polakowski, N.H. and E.J. Ripling, STRENGTH AND STRUCTURE OF ENGINEERING MATERIALS, Princeton-Hall, Inc., Englewood Cliffs, N.J., 1966.

101. Smith, R.W., M.H. Hirschberg, and S.S. Manson, NASA TN-D-1574, April 1963.

102. Endo, T. and J.D. Morrow, Journal of Materials, JMLSA, Vol. 4, No. 1, p. 159, March 1969.

103. Morrow, J.D., in INTERNAL FRICTION, DAMPING, AND CYCLIC PLASTICITY, ASTM STP 378, p. 45, 1965.

104. Neuber, H., Journal of Applied Mechanics, p. 544, Dec. 1961.

105. Wessel, E.T., W.G. Clark, Jr., and W.K. Wilson, DDC Report AD-801001, 1966.

106. Paris, P.C. and G.C. Sih, in FRACTURE TOUGHNESS TESTING AND ITS APPLICATIONS, ASTM STP 381, p. 30, April 1965.

107. Wilson, W.K. and S.E. Gabrielse, unpublished Westinghouse Research Laboratories data.

108. Clark, W.G., Jr., FRACTURE TOUGHNESS AND SLOW-STABLE CRACKING, ASTM STP 559, p. 204, 1974.

109. Roberts, R. and G. Irwin, Journal of the Structural Division, ASCE, p. 337, Feb. 1976.

110. Radon, J.C. and L.E. Culver, Experimental Mechanics, p. 105, 1973.

111. Pook, L.P., Journal of Strain Analysis, Vol. 10, No. 4, p. 242, 1975.

112. Bilby, B.A. and Heald P.T., Proc. Royal Society A305, p. 429, 1968.

113. Lankford, J., Engineering Fracture Mechanics, Vol. 9, p. 617, 1977.

114. PROGRESS IN FLAW GROWTH AND FRACTURE TOUGHNESS TESTING, Proc. 1972 National Symposium on Fracture Mechanics, Phila., Pa., Aug. 1972, ASTM STP 536, 1973.

115. EFFECTS OF ENVIRONMENT AND COMPLEX LOAD HISTORY ON

FATIGUE LIFE, Proc. 1968 Fall Meeting American Society for Testing and Materials, Atlanta, Ga., Sept. 1968, ASTM STP 462, 1970.

116. LOCALIZED CORROSION-CAUSE OF METAL FAILURE, Proc. 74th Annual Meeting American Society for Testing and Materials, Atlantic City, N.J., June 1971, ASTM STP 516, 1972.

117. Osgood, C.C., *FATIGUE DESIGN, John Wiley and Sons* Inc., New York, 1970.

118. Wood, W.A., THE STUDY OF METAL STRUCTURE AND THEIR MECHANICAL PROPERTIES, Pergamon Press, New York, 1971.

119. Hertzberg, R.W., DEFORMATION AND FRACTURE MECHANICS OF ENGINEERING MATERIALS, John Wiley and Sons Inc., New York, 1976.

120. Morgan, J.H., CATHODIC PROTECTION, The Macmillan Company, New York, 1960.

121. Jelinek, R.V., CORROSION, Syracuse University, Syracuse, N.Y., McGraw-Hill Publishing Co., Inc., N.Y., 1959.

122. Hertzberg, R.W., DEFORMATION AND FRACTURE MECHANICS OF ENGINEERING MATERIALS, John Wiley and Sons, Inc., New York, 1976.

123. Barsom, J.M. and S.T. Rolfe, FRACTURE AND FATIGUE CONTROL IN STRUCTURES, Prentice-Hall, Inc., Englewood Cliffs, New Jersey, 1977.

TABLE 3.1 - Modifying factor, k_c, for various survival rates (40).

Survival rate, per cent	k_c
90	0.896
95	0.872
99	0.816
99.9	0.752
99.99	0.704

TABLE 4.1 - Order of magnitude of protective currents for steel (121).

Environment	Amp./Sq. Cm.
Well-cured halogen-free concrete	7×10^{-8}
Sterile, anerobic neutral soil water	5×10^{-7}
Halogen-containing concrete	5×10^{-7}
Aerated neutral soil water	4×10^{-6}
Deaerated hot water	4×10^{-6}
Moving fresh water	6×10^{-6}
Moving sea water	1.5×10^{-5}
Oxygen-saturated hot water	1.5×10^{-5}
Anaerobic soil with active sulfate reducing bacteria	5×10^{-5}
Hot sulfuric acid	4×10^{-2}

TABLE 5.1 - Chemical composition of 1018 steel and HY-180, percent.

	C	Mn	P	S	Si	Ni	Cr	Mo	Co	Al
HY-180	0.11	0.12	0.004	0.005	0.04	10.0	2.0	1.0	8.0	0.005
1018	0.18	0.75	0.01	0.03	0.05	-	-	-	-	-

TABLE 5.2 - Mechanical properties of 1018 and HY-180 at room temp.

	0.2% Yield Strength (ksi)	Tensile Strength (ksi)	Elongation %	Reduction of Area %
HY-180	180	198	18	71
1018	40	65.5	40.8	67

TABLE 5.3 - Crack initiation data for 1018 steel.

Applied Load lb	Maximum Nominal Stress ksi	Number of Cycles to Initiation
140-1400	15	50000
400-2000	19	14400
220-2200	23.5	7100
300-3000	32	1950
1800-4500	32	1650

TABLE 6.1 - Proposed methods for predicting σ_f' (96-99).

Investigators	Proposed Correlation	σ_f'
Manson	$\sigma_a=\sigma_f$ at 1/4 cycle	$\sigma_f'=0.92\sigma_f$ (b=-0.12)
Manson	$\sigma_a=\sigma_f$ at 1 cycle	$\sigma_f'=1.09\sigma_f$ (b=-0.12)
Manson and Hirschberg	$2\sigma_a=2.5\sigma_f$ at 1/4 cycle	$\sigma_f'=1.15\sigma_f$ (b=-0.12)
Halford and Morrow	$\sigma_a=\sigma_f$ at 1/2 cycle	$\sigma_f'=\sigma_f$

TABLE 6.2 - Fatigue crack initiation data for 1018 steel.

Notch Radius (in)	K_t	Applied Load (lb)	$\Delta\sigma_N$ (ksi)	$\Delta\sigma_{max}$ (ksi)	ΔK_I	$\frac{\Delta K_I}{\sqrt{\rho}}$	N_i
.015	10.25	140-1400	15	153	16.6	135.5	51000
.015	10.25	400-2000	19	194	21.1	172.3	14400
.015	10.25	220-2200	23.5	240	26	212	7100
.015	10.25	300-3000	32	328	36	294	1950
.015	10.25	1800-4500	32	328	36	294	1600

TABLE 6.3 - Total strain calculations for 1018 steel.

Notch Radius (in)	K_t	σ_{mean} (ksi)	$\Delta\sigma_N$ (ksi)	$\frac{\Delta\epsilon}{2}$	N_i
.015	10.25	9.12	15	.00466	51000
.015	10.25	14.2	19	.0055	14400
.015	10.25	14.34	23.5	.0078	7100
.015	10.25	19.55	32	.014	1950
.015	10.25	37.3	32	.0163	1600

TABLE 6.4 - Fatigue crack initiation data for 403 stainless steel (108).

Notch Radius (in)	K_t	Applied Load (lb)	$\frac{\Delta K_I}{\sqrt{\rho}}$	$\frac{\Delta\epsilon}{2}$	N_i
.01	11	200-3000	140	.00309	92000
.01	11	200-4000	190	.00486	24300
.01	11	200-5000	240	.00753	6600
.01	11	200-6000	300	.00968	4800
.038	5.6	250-5000	122	.00262	133800
.038	5.6	200-4500	110	.00233	180000
.038	5.6	200-7000	174	.0041	50700
.038	5.6	200-8000	200	.0058	11150
.189	2.6	200-11000	124	.00311	45000
.189	2.6	200-10000	113	.00256	120000

TABLE 6.5 - Comparison between crack initiation prediction methods and experimental data for 1018 steel.

Nominal Stress $\Delta\sigma$ (psi)	Total Strain Approach (psi)	$\Delta K/\sqrt{\rho}$ Approach N_i	Manson-Coffin Method N_i	Experimental Data N_i
15000	41000	50370	20100	51000
19000	12600	16520	7745	14400
23500	6700	6312	4400	7100
32000	1850	1400	1600	1950
32000	1400	1400	530	1650

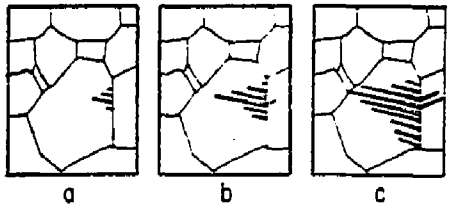

FIGURE 2.1 - Persistent slip band development from a grain boundary.

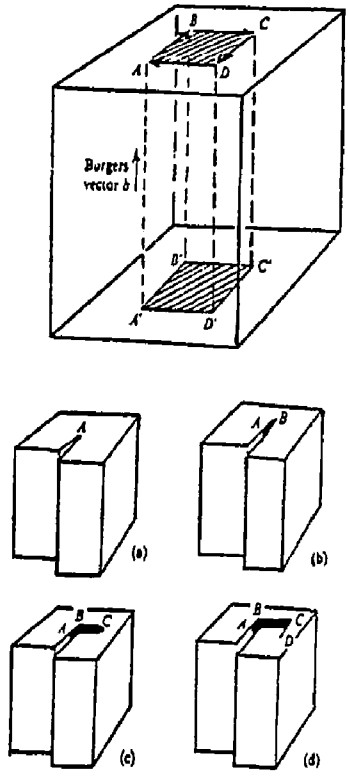

FIGURE 2.2 - Mott's slip mechanism for fatigue crack nucleation. (4)

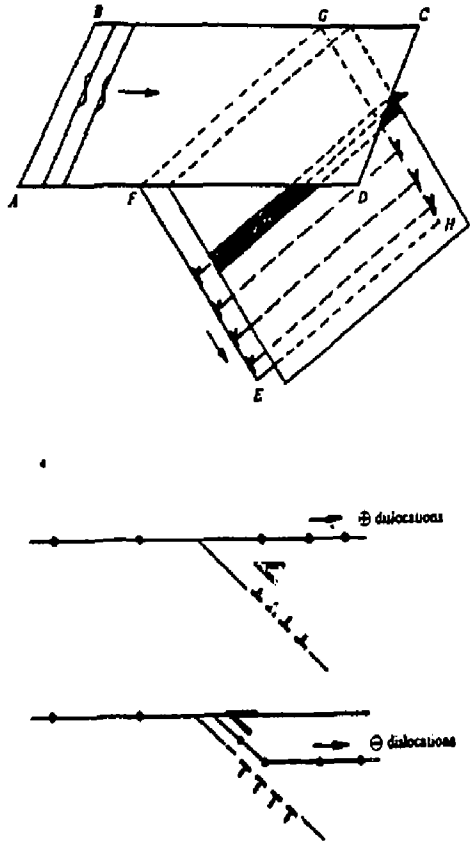

FIGURE 2.3 - A Kennedy mechanism for extrusion-intrusion formation. Lomer-Cottrell barrier is situated at the intersection of slip planes ABCD and EFGH. (5)

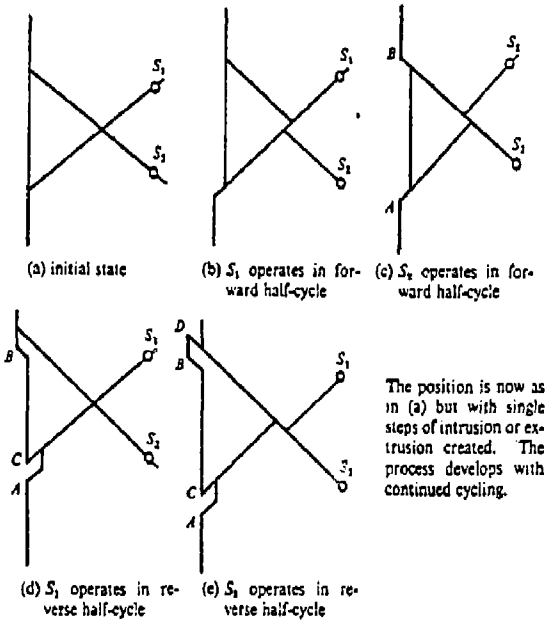

FIGURE 2.4 - The Cottrell-Hull mechanism for extrusion-intrusion formation. (6)

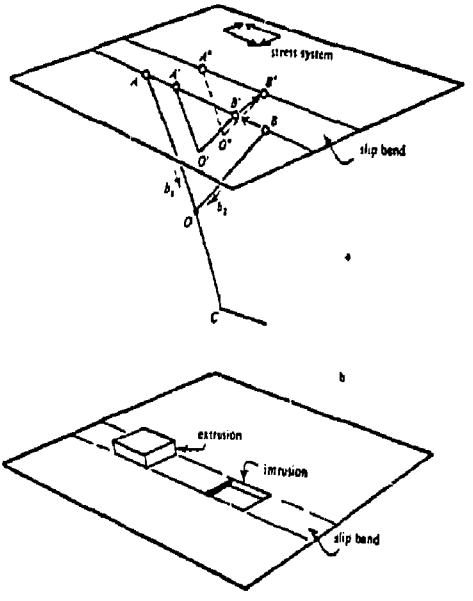

FIGURE 2.5 - The McEvily-Machlin model of extrusion-intrusion formation. (7)

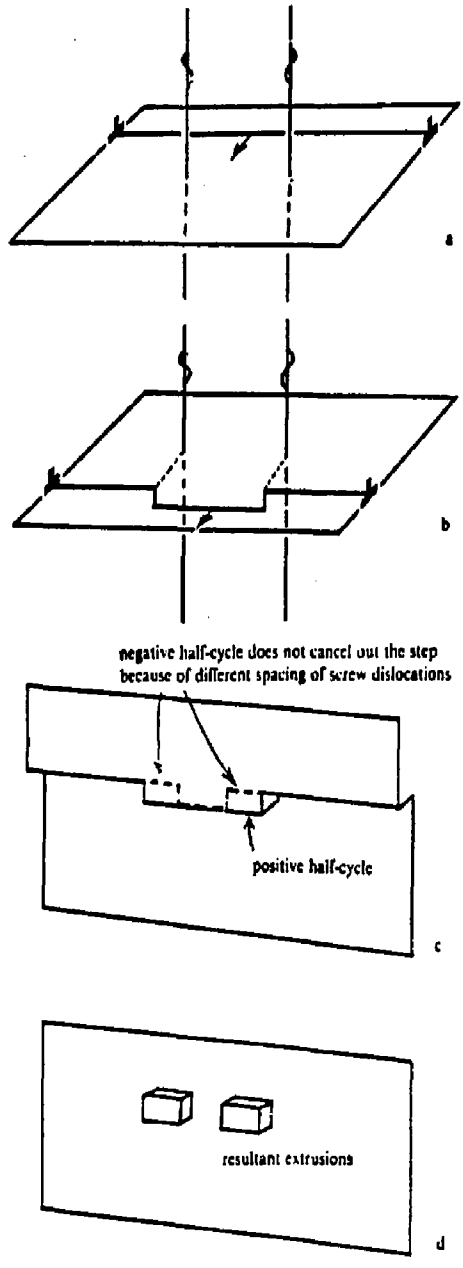

FIGURE 2.6 - The Thompson fatigue extrusion-intrusion mechanism (8)

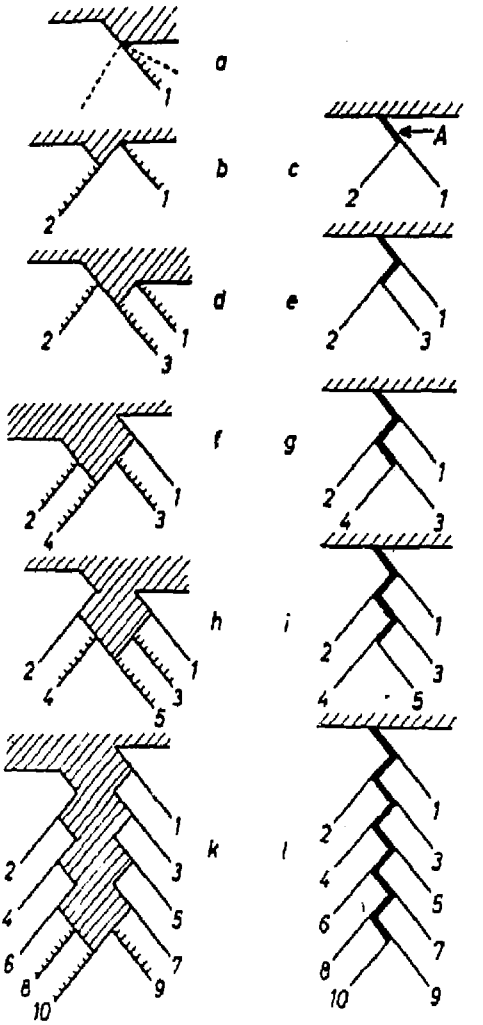

FIGURE 2.7 - Neumann's model for the formation of cracks by coarse slip. (14)

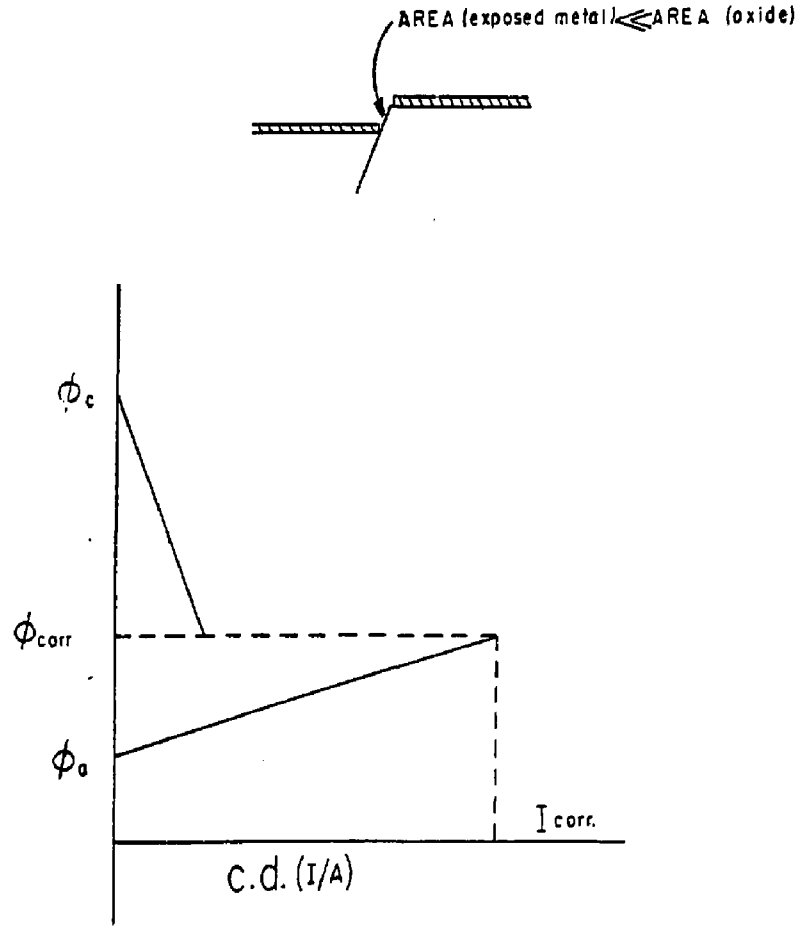

FIGURE 2.8 - Model of slip band penetration of oxide film and resultant polarization diagram in aqueous environment (electrochemical potentials vs. current). (19)

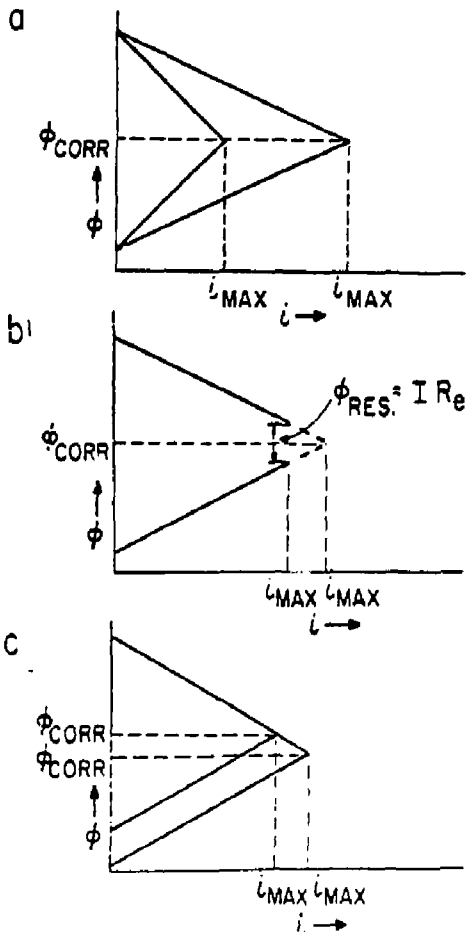

FIGURE 2.9 - Models for preferential dissolution of deformed regions in cyclically deformed metals (electrochemical potentials vs. current). (20)

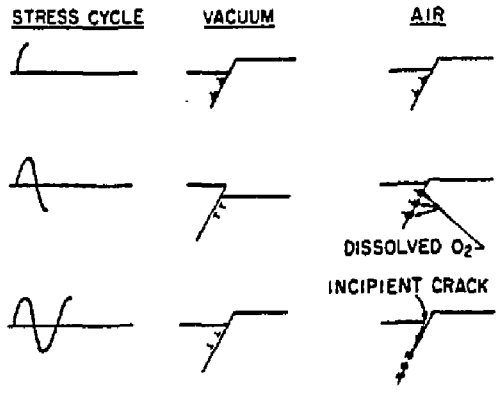

FIGURE 2.10 - Thompson and Wadsworth model for oxygen slip band interaction to affect fatigue crack nucleation. (30)

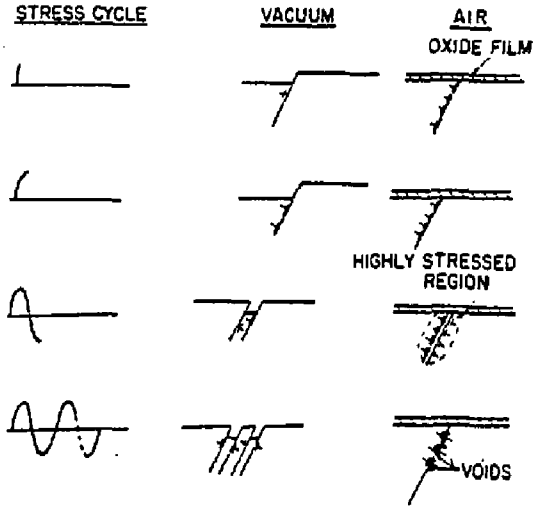

FIGURE 2.11 - Shen model of oxide film dislocation interaction to accelerate fatigue crack nucleation. (31)

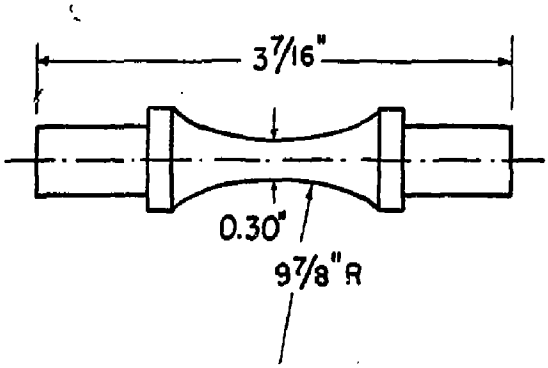

FIGURE 3.1 - Test specimen for R.R. Moore rotating beam machine. (40)

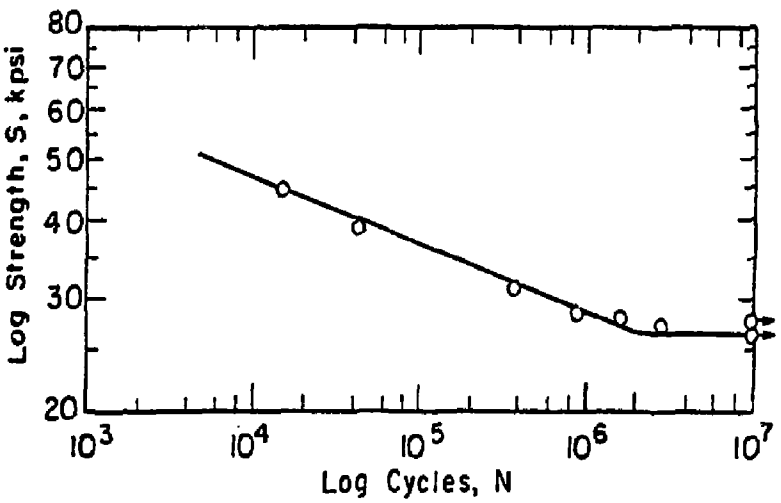

FIGURE 3.2 - S-N curve for annealed 1040 steel. (40)

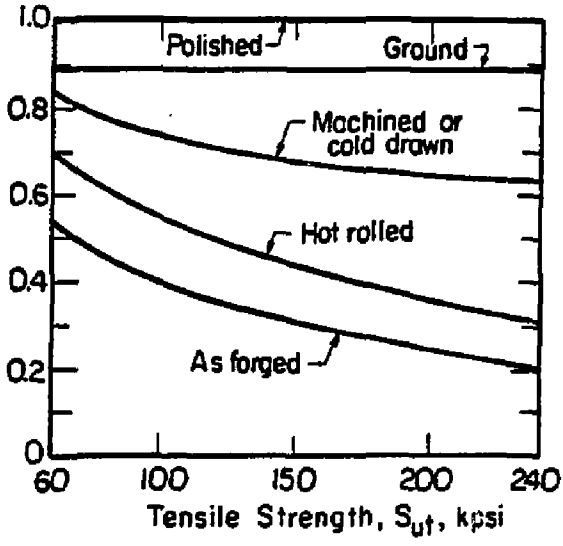

FIGURE 3.3 - Modifying factor, k_a, for surface finish. (40)

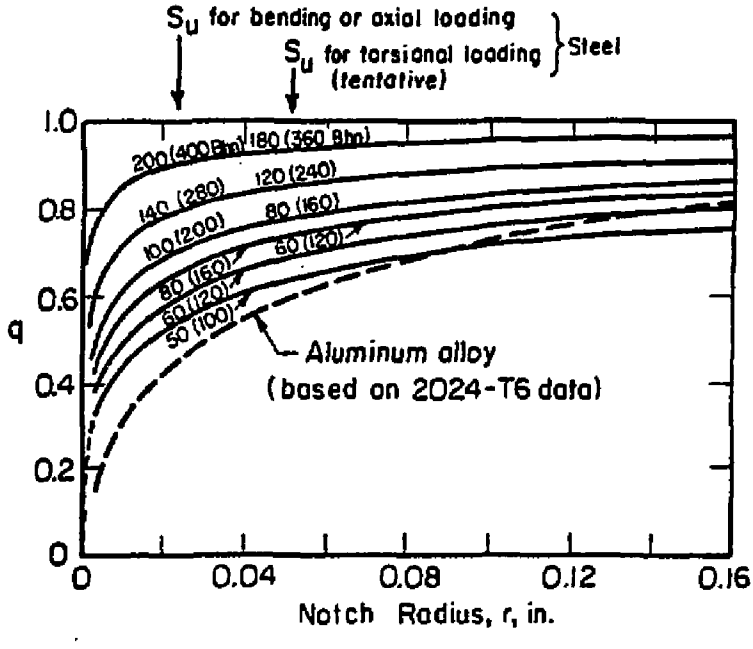

FIGURE 3.4 - Notch sensitivity curves for steel and aluminum alloy in bending, axial and torsional loading. (40)

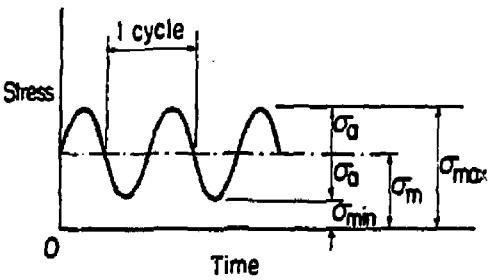

FIGURE 3.5 - Fatigue stress components. (40)

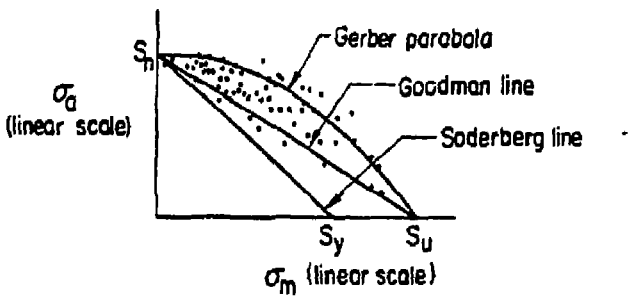

FIGURE 3.6 - Three proposed diagrams of constant fatigue life for steel and aluminum. (40)

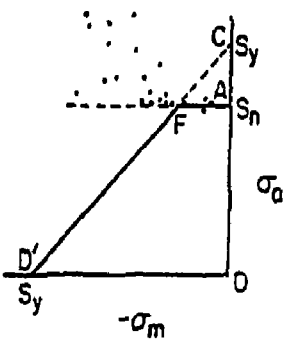

FIGURE 3.7 - σ_m - σ_a diagram for compressive mean stress (steel and aluminum). (40)

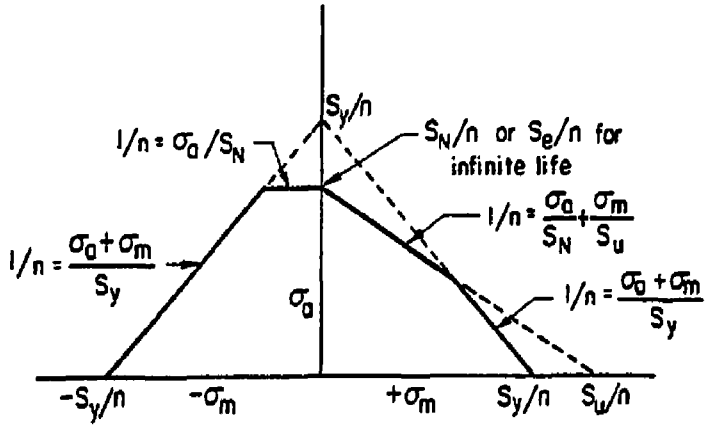

FIGURE 3.8 - Design diagram for fatigue failure.

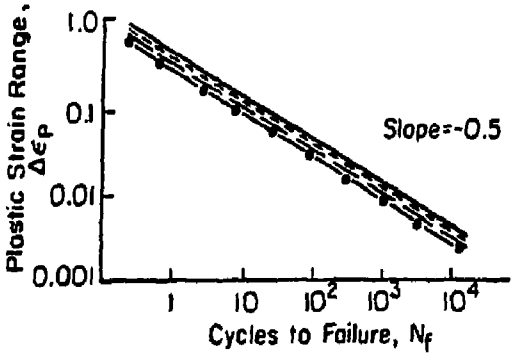

FIGURE 3.9 - Coffin-Manson relationship for Ni/Cr/Mo alloy steel, C/Mn steel, Al-Mg alloy, and Al-Cu alloy. (45,46)

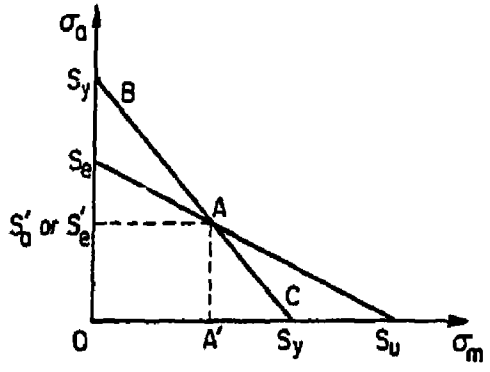

FIGURE 3.10 - Modified Goodman diagram.

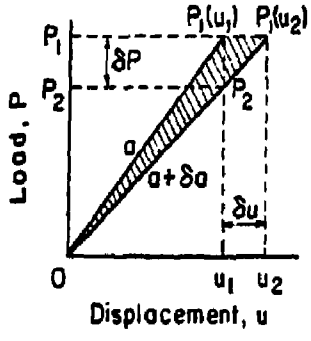

FIGURE 3.11 - Load-displacement curve for crack length a and (a + δ a).

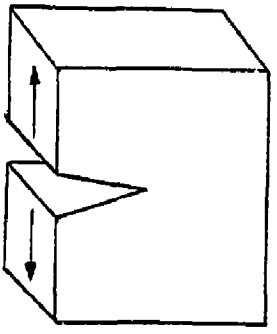

Mode I

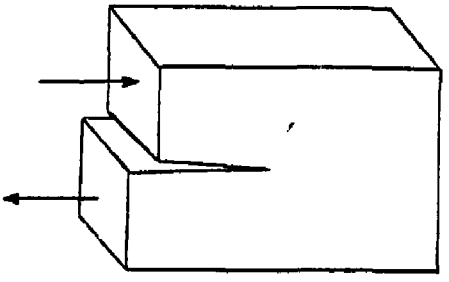

Mode II

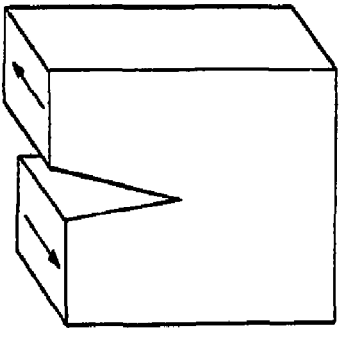

Mode III

FIGURE 3.12 - Modes of crack tip deformation.

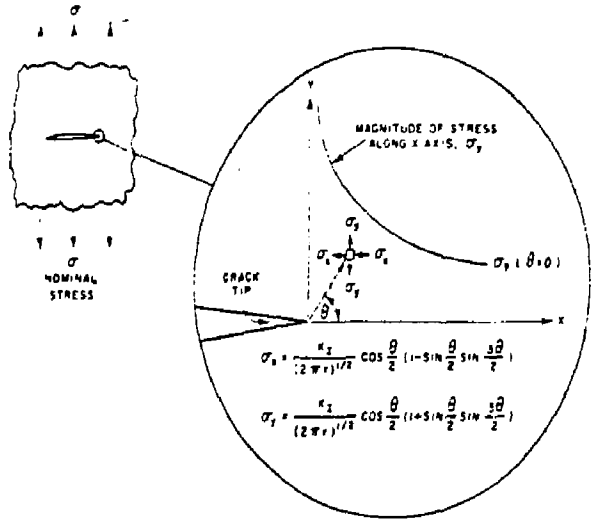

FIGURE 3.13 - Schematic drawing of the elastic stress field distribution near the tip of a sharp crack (Mode I deformation).

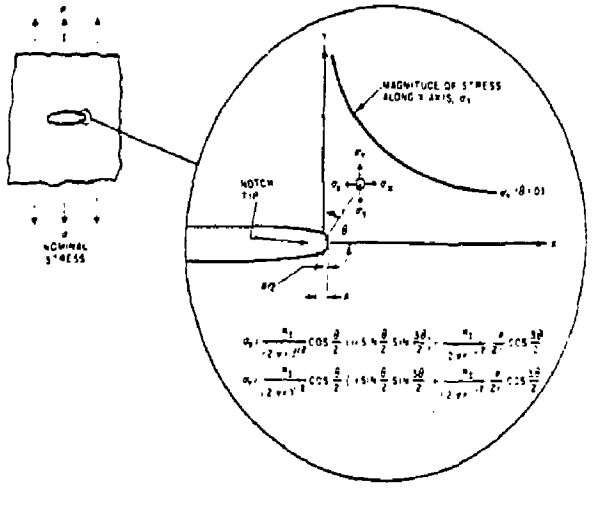

FIGURE 3.14 - Schematic drawing of the elastic stress field distribution near the tip of an elliptical notch (Mode I deformation).

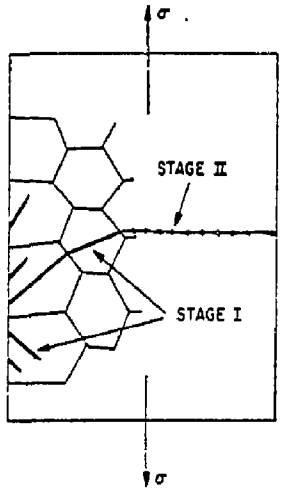

FIGURE 4.1 - Schematic representation of the two stages of crack propagation. (54)

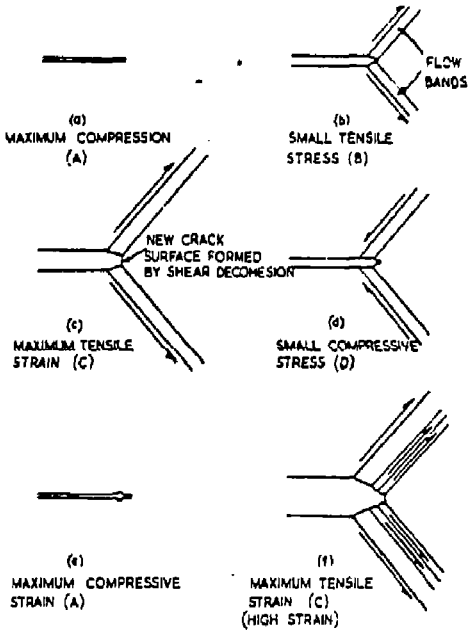

FIGURE 4.2 - Plastic blunting process for stage II crack propagation. (55)

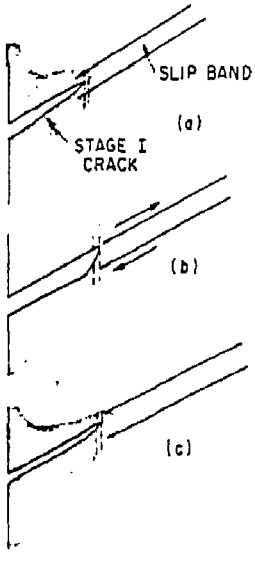

FIGURE 4.3 - The plastic blunting process for stage I crack propagation - a) zero stress, b) maximum tensile stress, and c) compressive stress. (55)

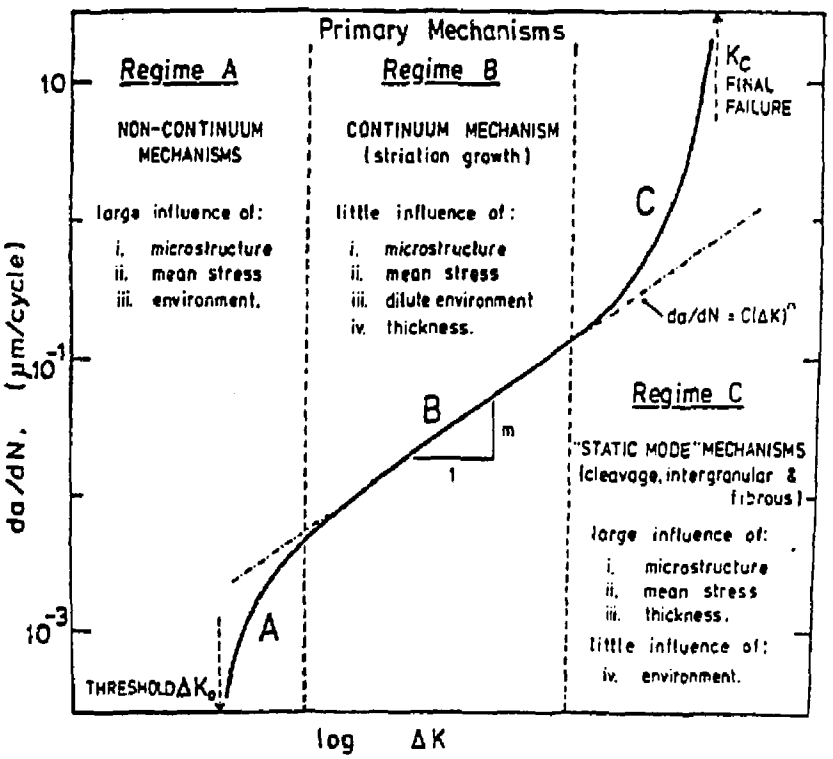

FIGURE 4.4 - Summary diagram showing the primary fracture mechanisms and the effect of microstructure and test variables on fatigue crack propagation. (56)

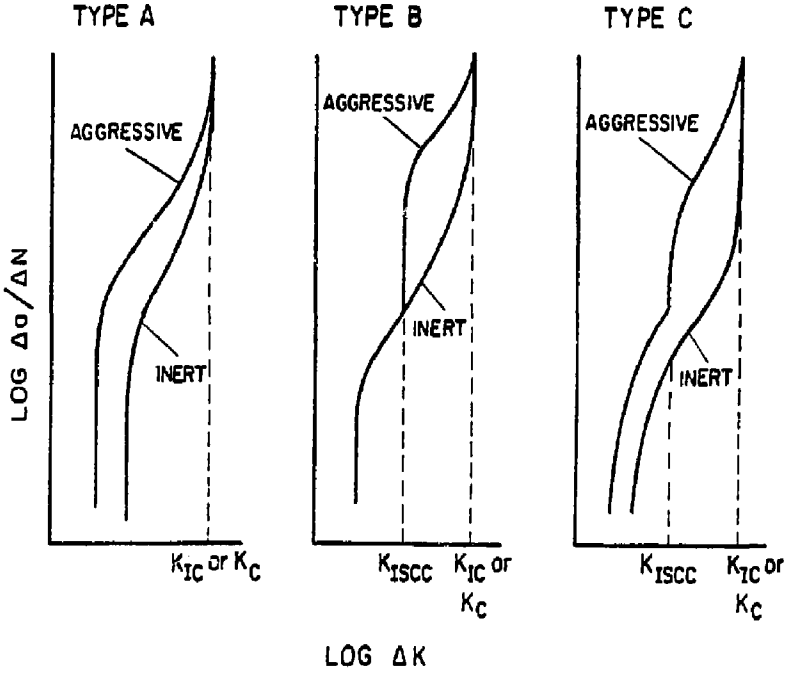

FIGURE 4.5 - Types of fatigue crack growth behavior.

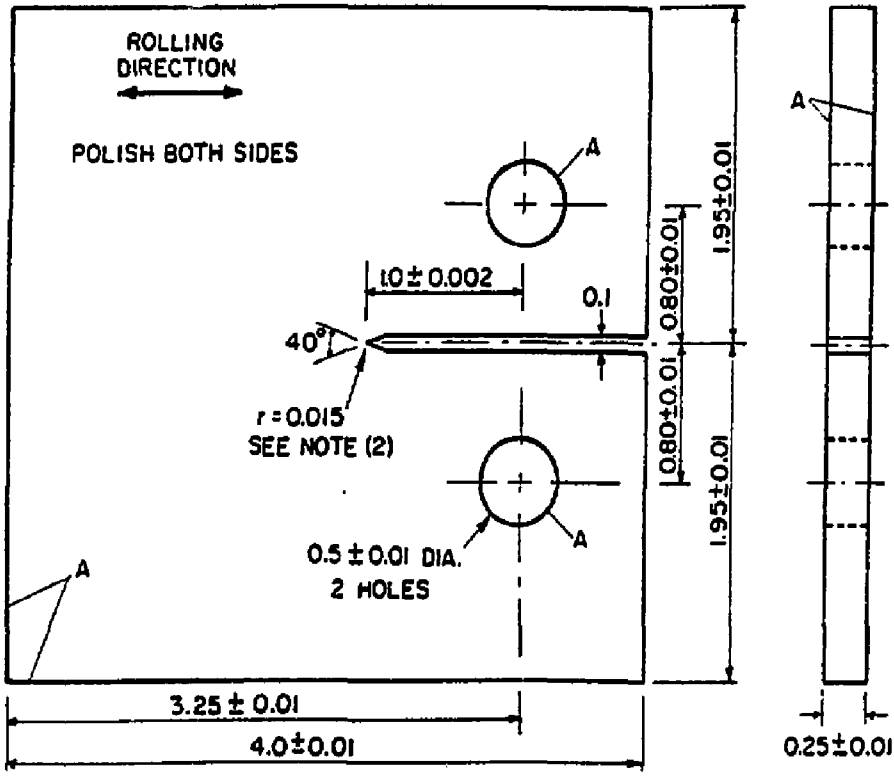

NOTES: 1 - "A" surfaces shall be perpendicular and parallel as applicable to within ±0.005 tir.
2 - Notch radii r=0.015 must be honed to a finish of at least 16 micro inch.

FIGURE 5.1 - Compact tension specimen.

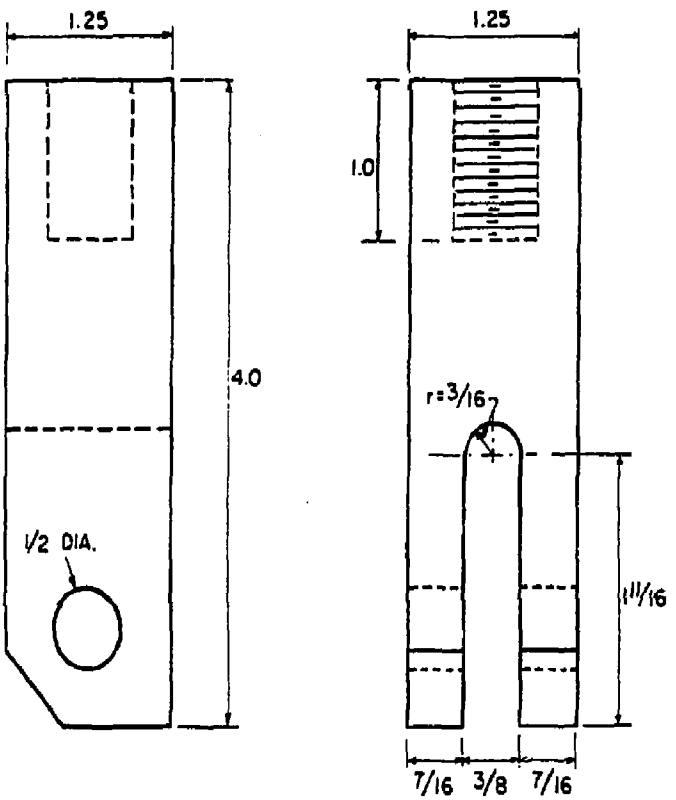

FIGURE 5.2 - Loading fixture.

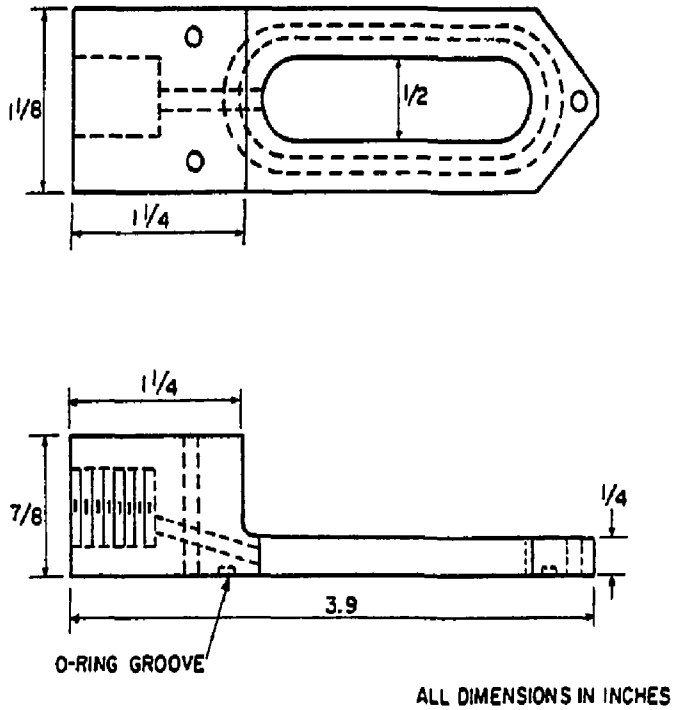

STAINLESS STEEL

FIGURE 5.3 - Corrosion chamber.

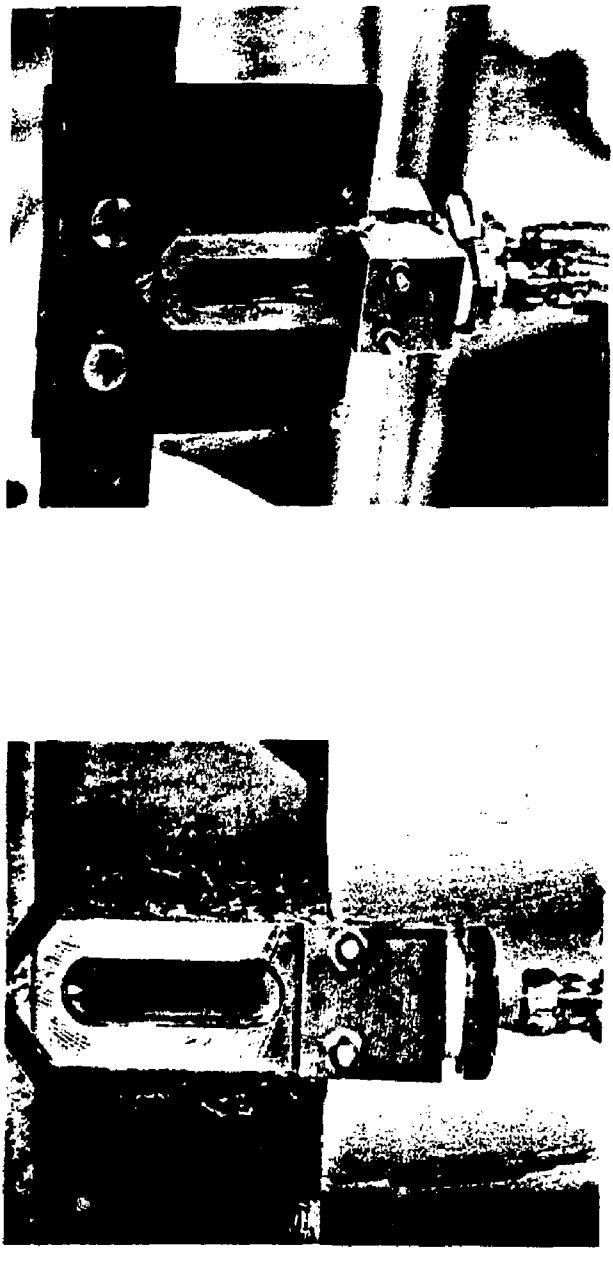

FIGURE 5.4 - Photographs of corrosion chamber mounted on the specimen.

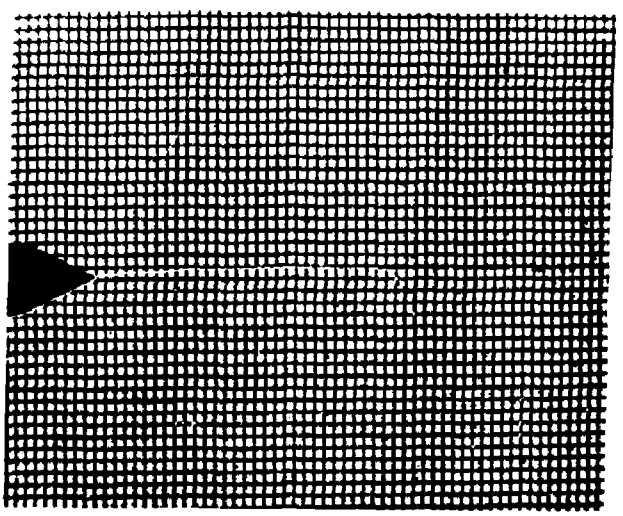

FIGURE 5.5 - Photograph of the crack propagating through the grid lines (0.02 inch) printed on the specimen.

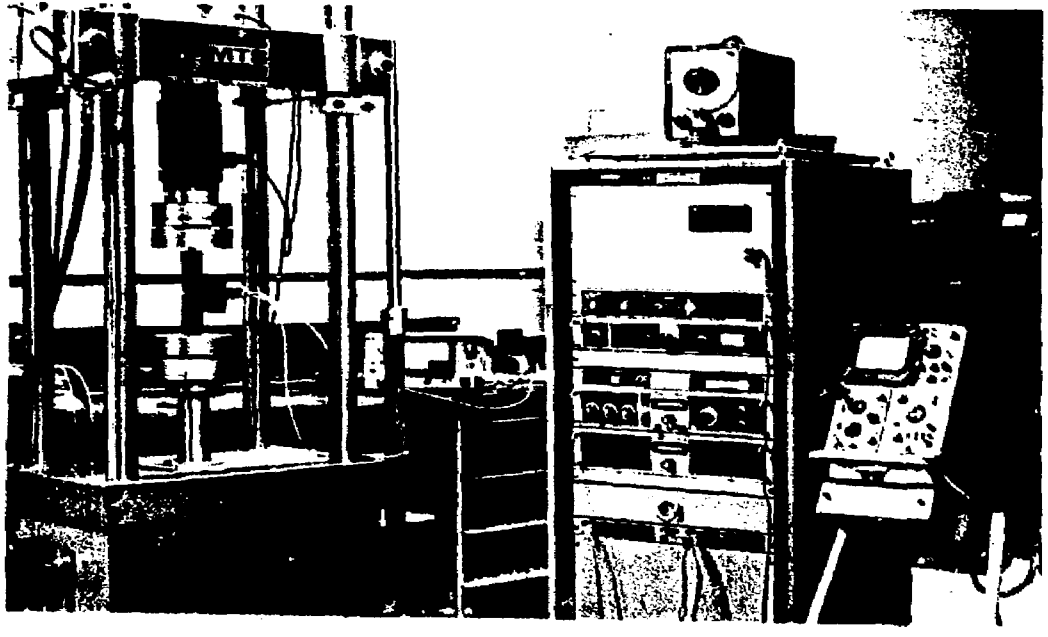

FIGURE 5.6 - Testing apparatus used for fatigue experiments in air and salt water environments.

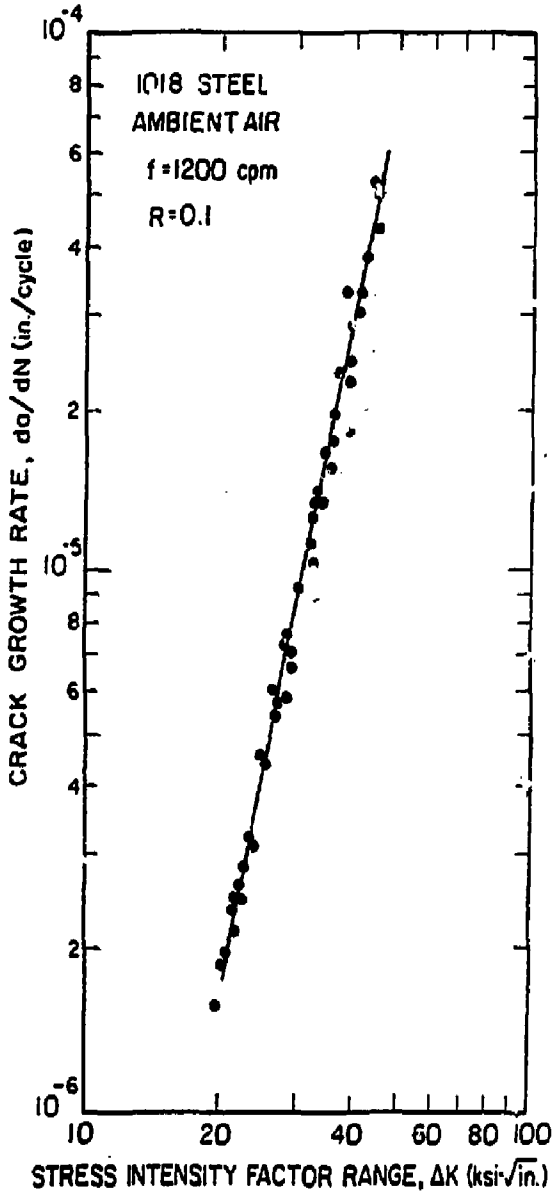

FIGURE 5.7 - Fatigue crack growth rates for 1018 steel in ambient air (60 percent humidity).

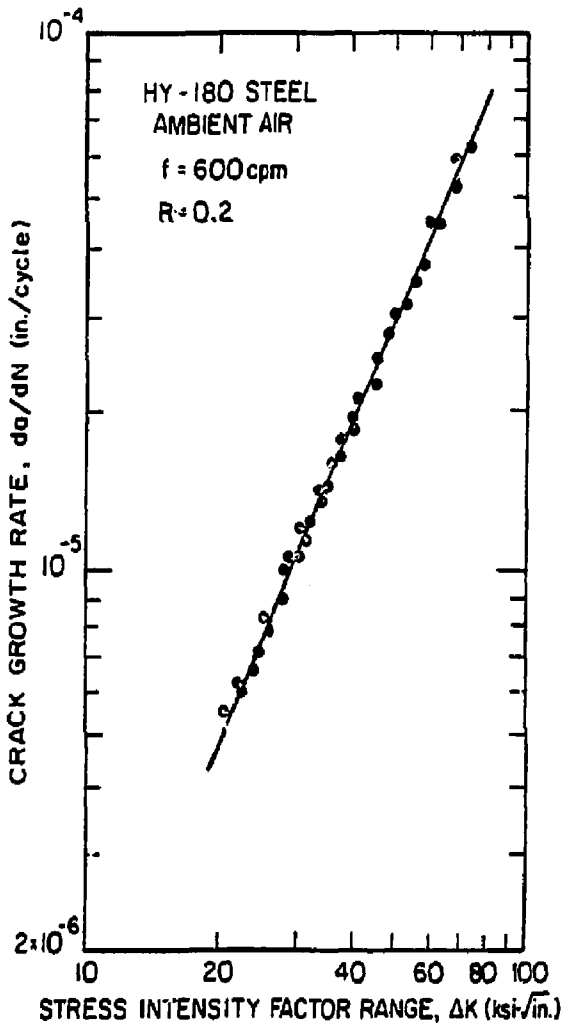

FIGURE 5.8 - Fatigue crack growth rates for HY-180 steel in ambient air (60 percent humidity).

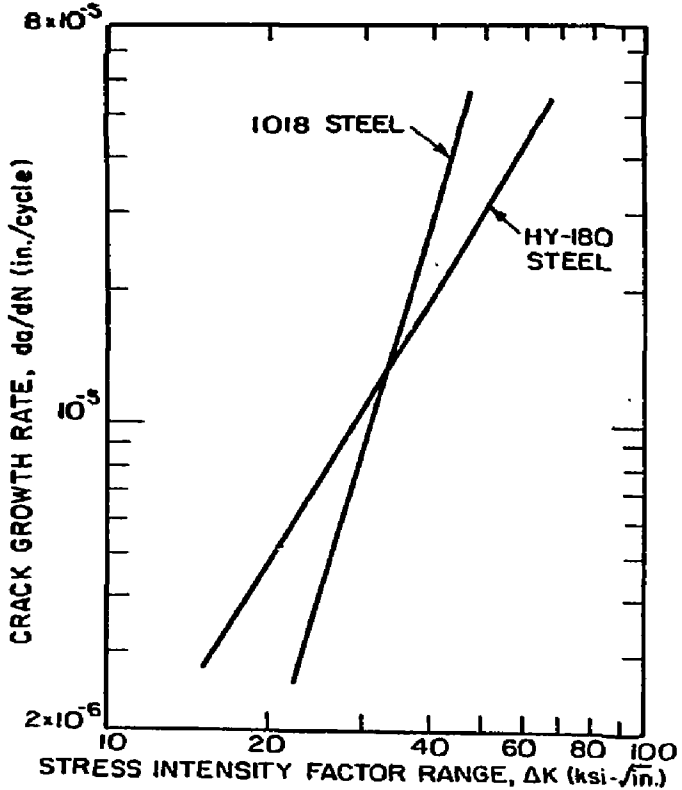

FIGURE 5.9 - Comparison of fatigue crack growth rates for 1018 and HY-180 steels.

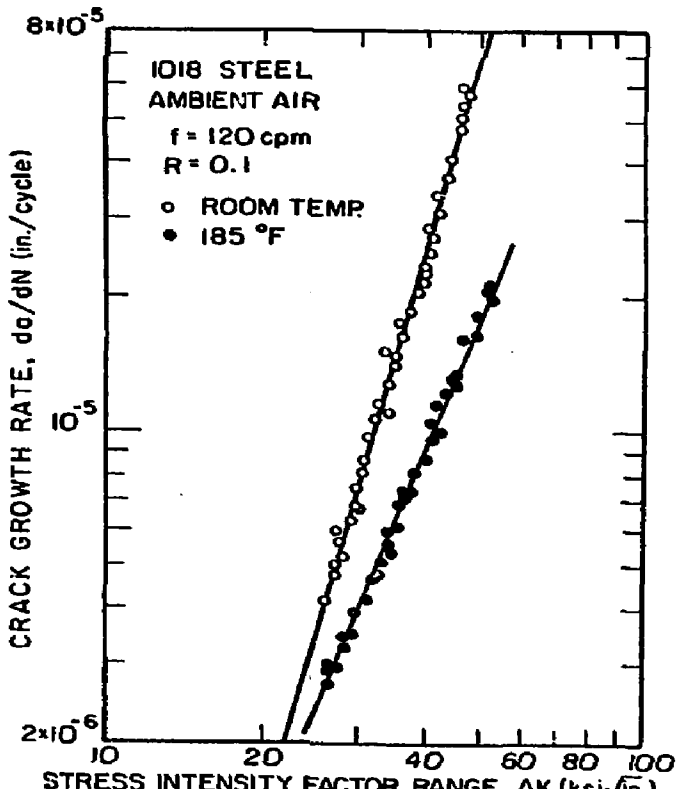

FIGURE 5.11- Effect of temp. on fatigue crack growth rates of 1018 steel.

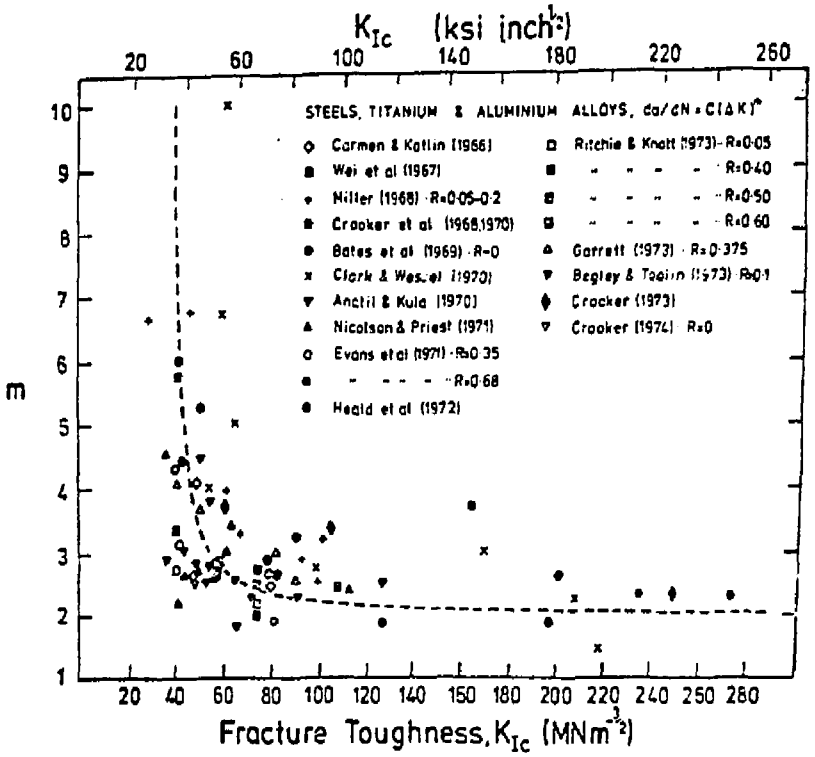

FIGURE 5.10 - The variation of exponent n with fracture toughness for several materials. (56)

(a)

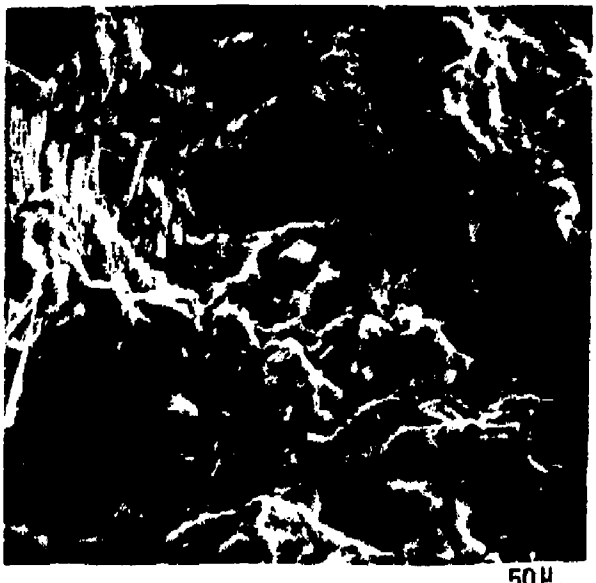

(b)

FIGURE 5.12 - Ductile striation growth during fatigue of 1018 steel in room temp. (a) at ΔK=20 ksi-$\sqrt{in}$ and 5000X, (b) at ΔK=25 ksi-$\sqrt{in}$ and 2000X.

FIGURE 5.13 - Ductile striation growth during fatigue of 1018 steel at 185°F and 3000X (a) ΔK=28 ksi-$\sqrt{in}$ and (b) ΔK=45 ksi-$\sqrt{in}$.

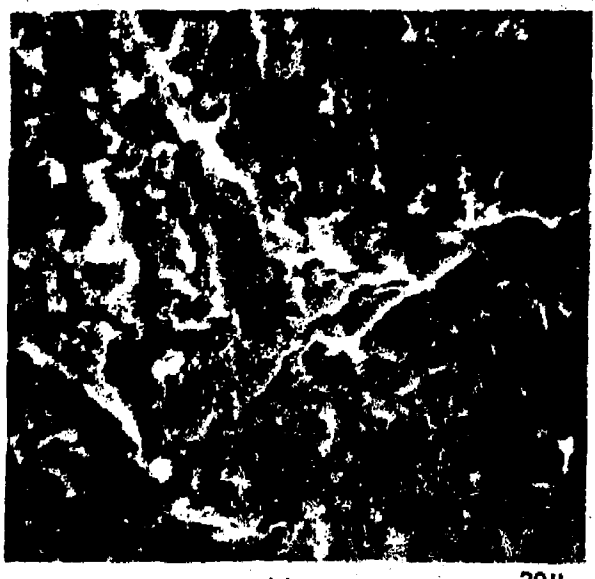

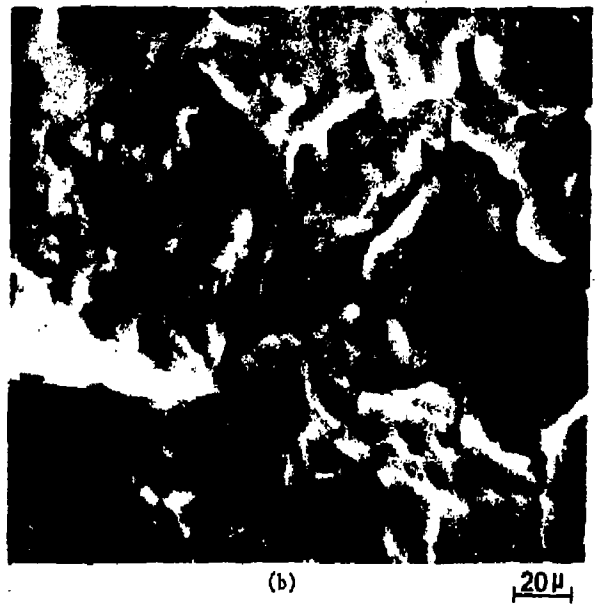

FIGURE 5.14 - Fatigue fracture surface of HY-180 steel at room temp.
(a) no clear striations visible at 3000X and ΔK=35 ksi-$\sqrt{in}$,
(b) region of ductile striation at 5000X and ΔK=65 ksi-$\sqrt{in}$.

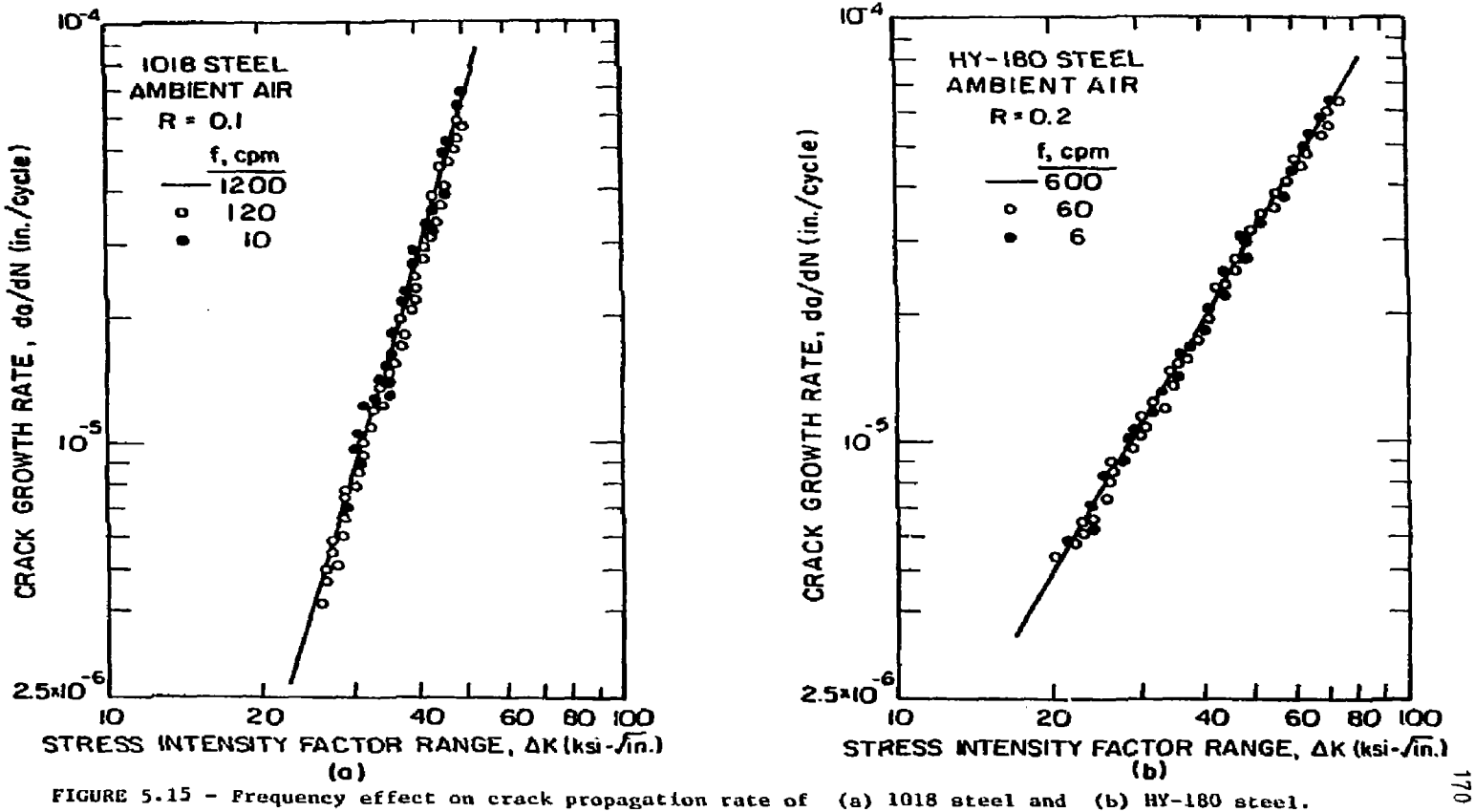

FIGURE 5.15 - Frequency effect on crack propagation rate of (a) 1018 steel and (b) HY-180 steel.

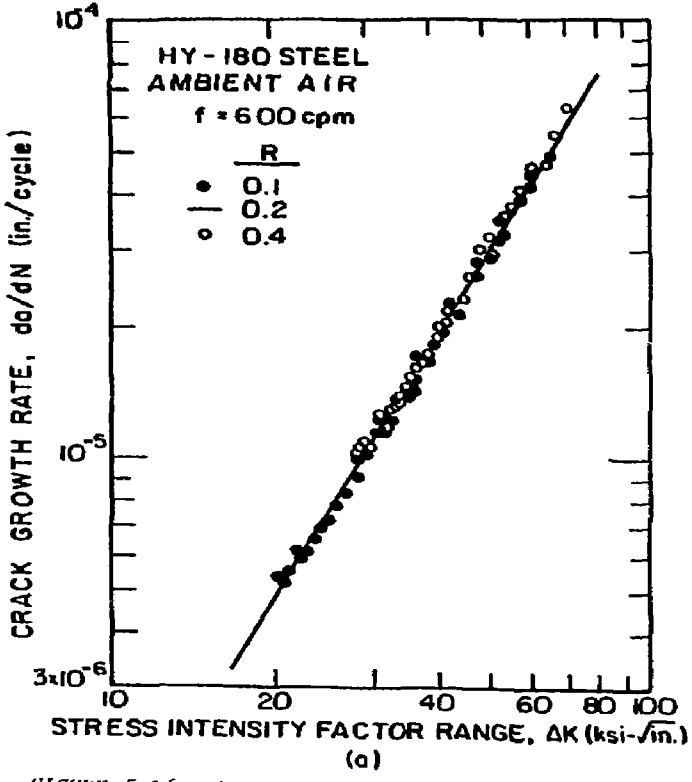

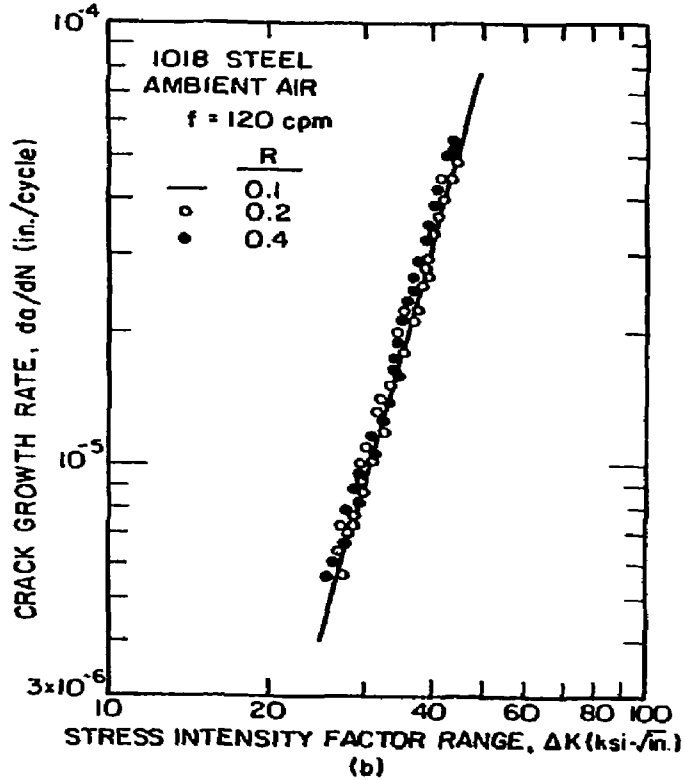

FIGURE 5.16 - Load ratio effect on crack propagation rate, (a) HY-180 steel, and (b) 1018 steel.

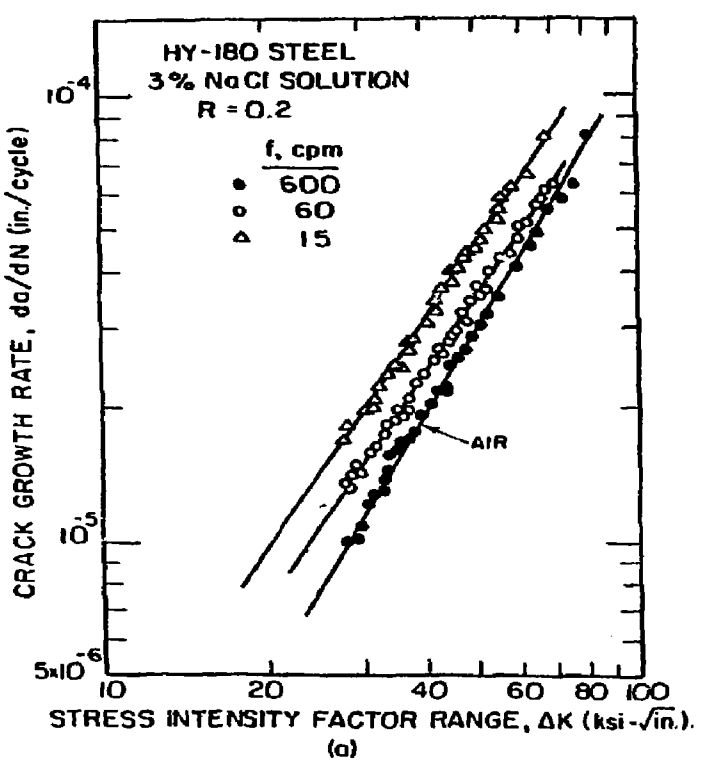

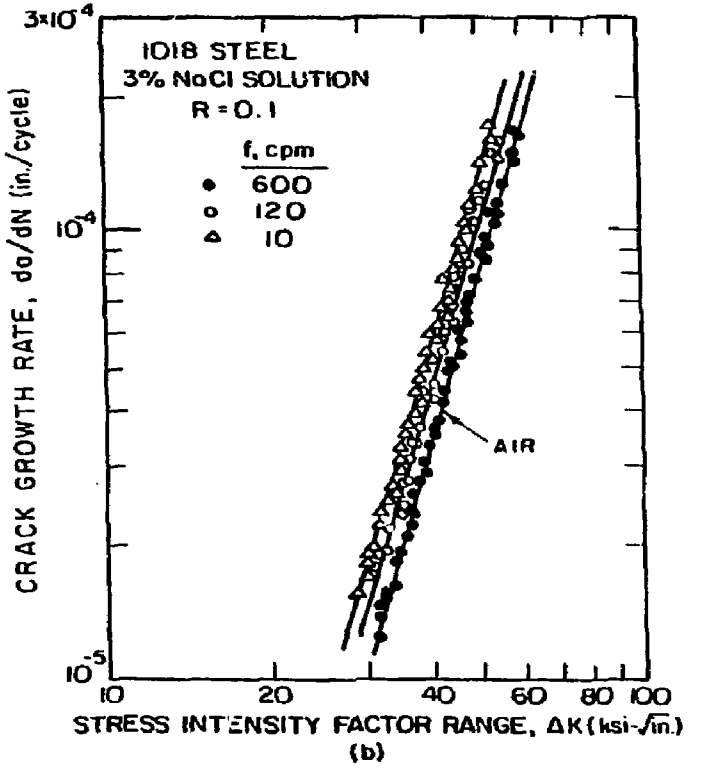

FIGURE 5.17 - Corrosion-fatigue crack growth data as a function of test frequency (a) HY-180 steel, (b) 1018 steel.

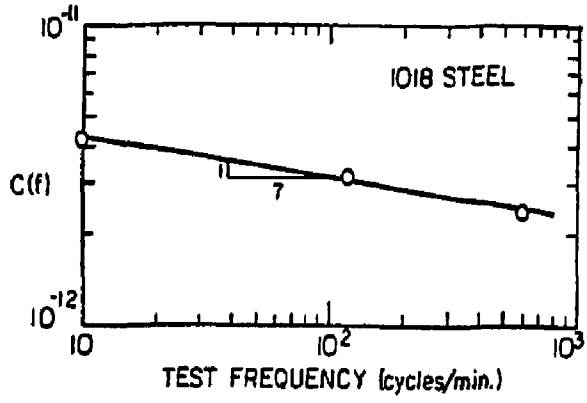

FIGURE 5.18 - Relationship between C(f) and test frequency for 1018 steel in 3% NaCl solution.

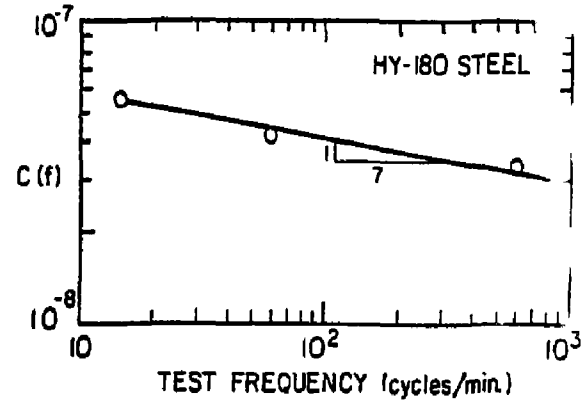

FIGURE 5.19 - Relationship between C(f) and test frequency for HY-180 steel in 3% NaCl solution.

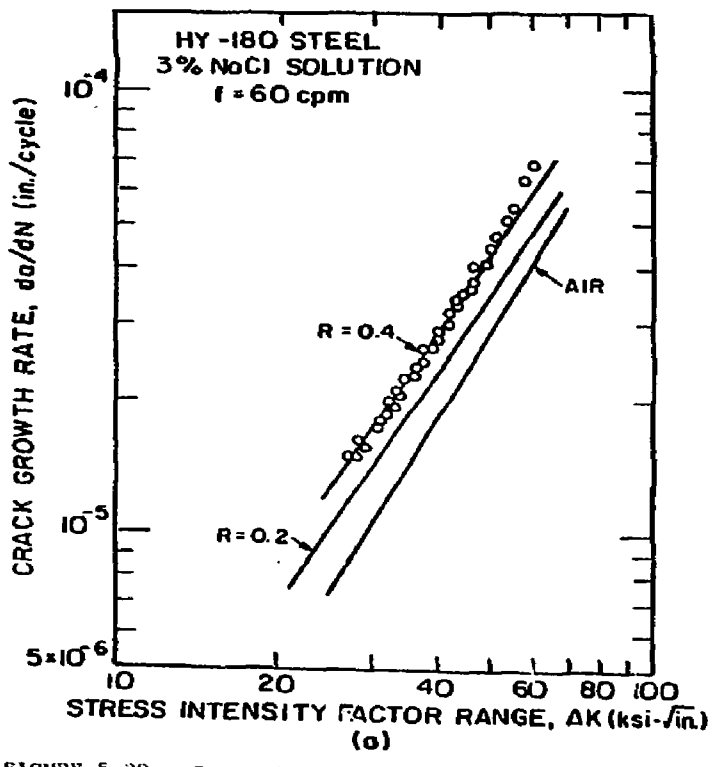

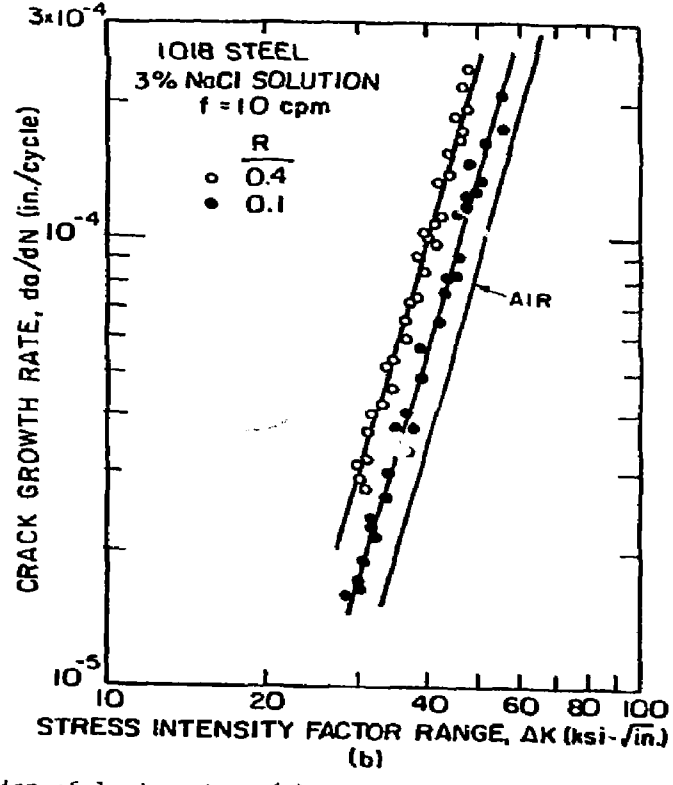

FIGURE 5.20 - Corrosion-fatigue crack growth data as a function of load ratio - (a) HY-180 steel, (b) 1018 steel.

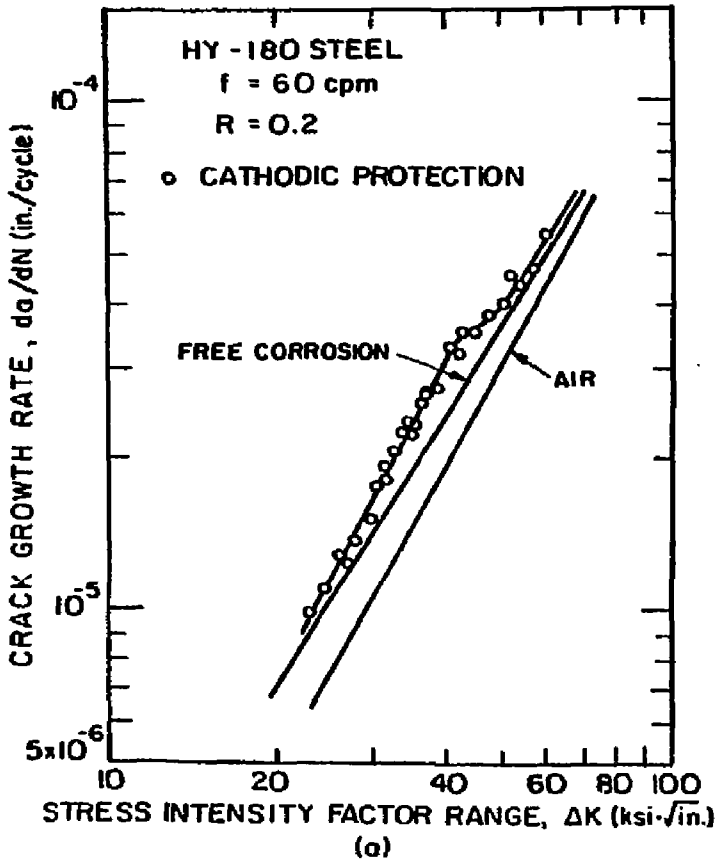

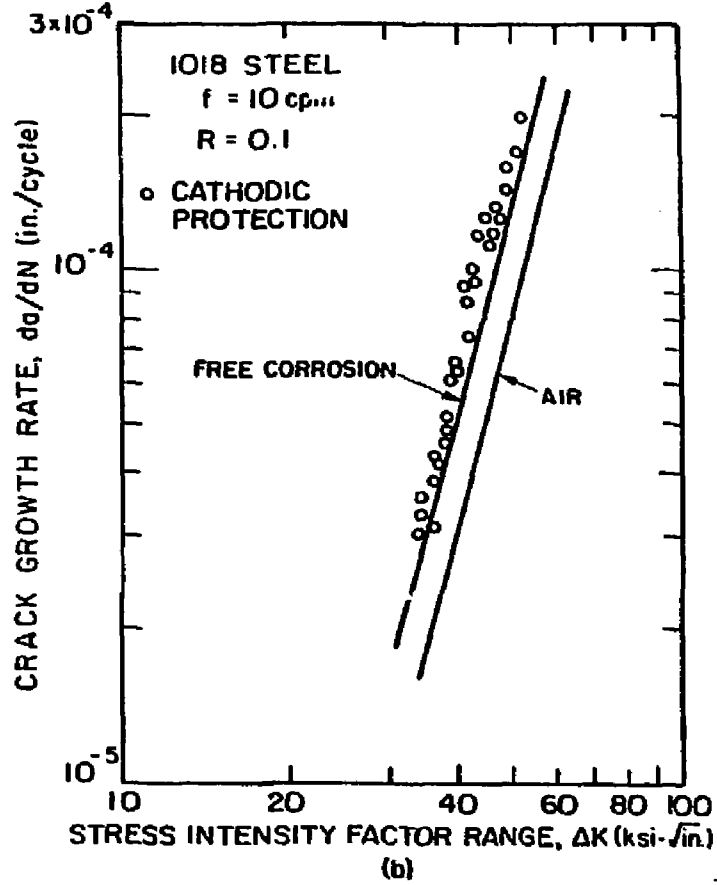

FIGURE 5.21 - Effect of cathodic protection on corrosion-fatigue crack growth rate, (a) HY-180 steel, (b) 1018.

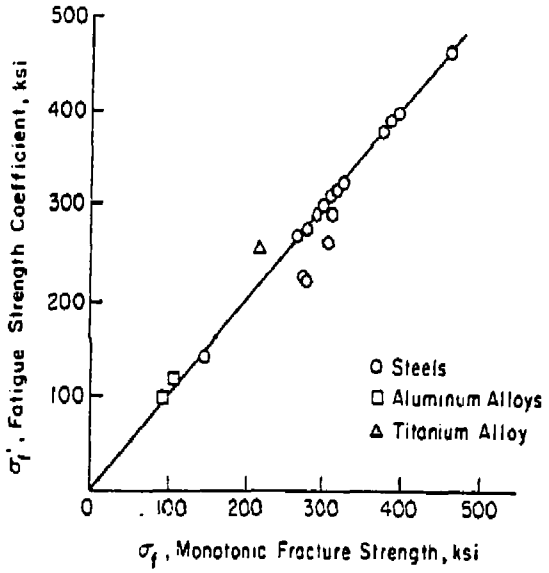

FIGURE 6.1 - Relationship between the fatigue strength coefficient and true fracture strength. (122)

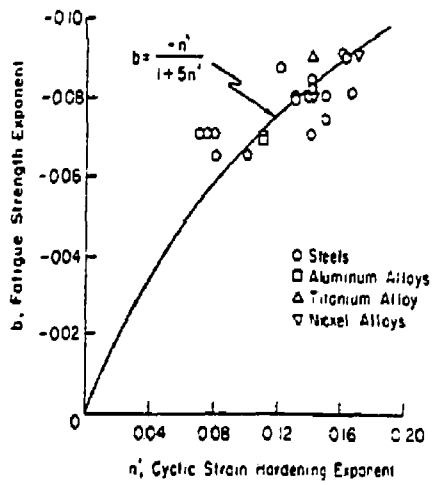

FIGURE 6.2 - Correlation between b and n' of equation 6.3. (103)

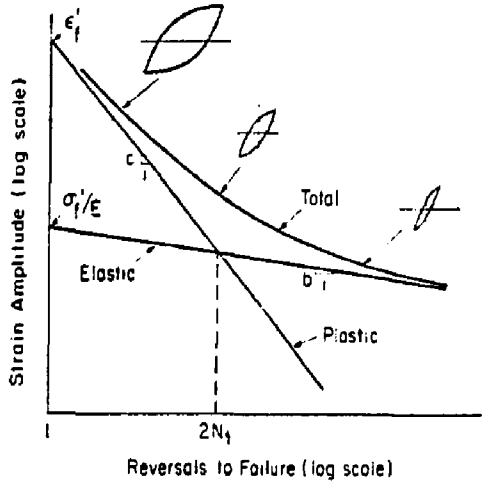

FIGURE 6.3 - Schematic representation of elastic, plastic and total strain. (122)

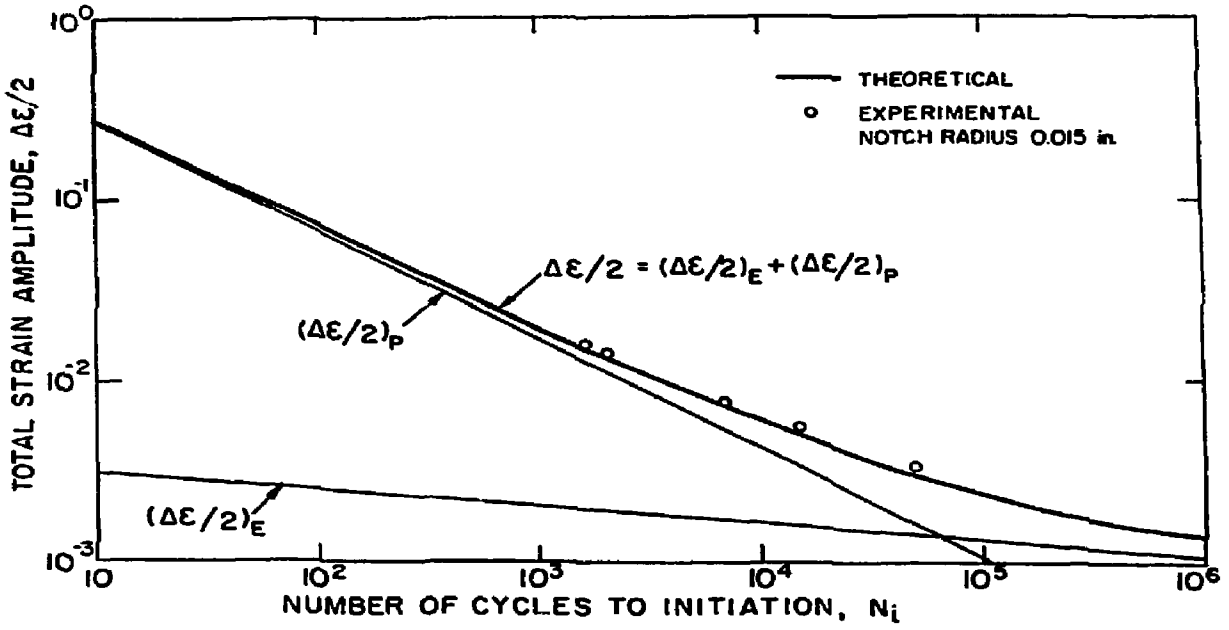

FIGURE 6.4 - Relationship between total strain amplitude and crack initiation data for 1018 steel.

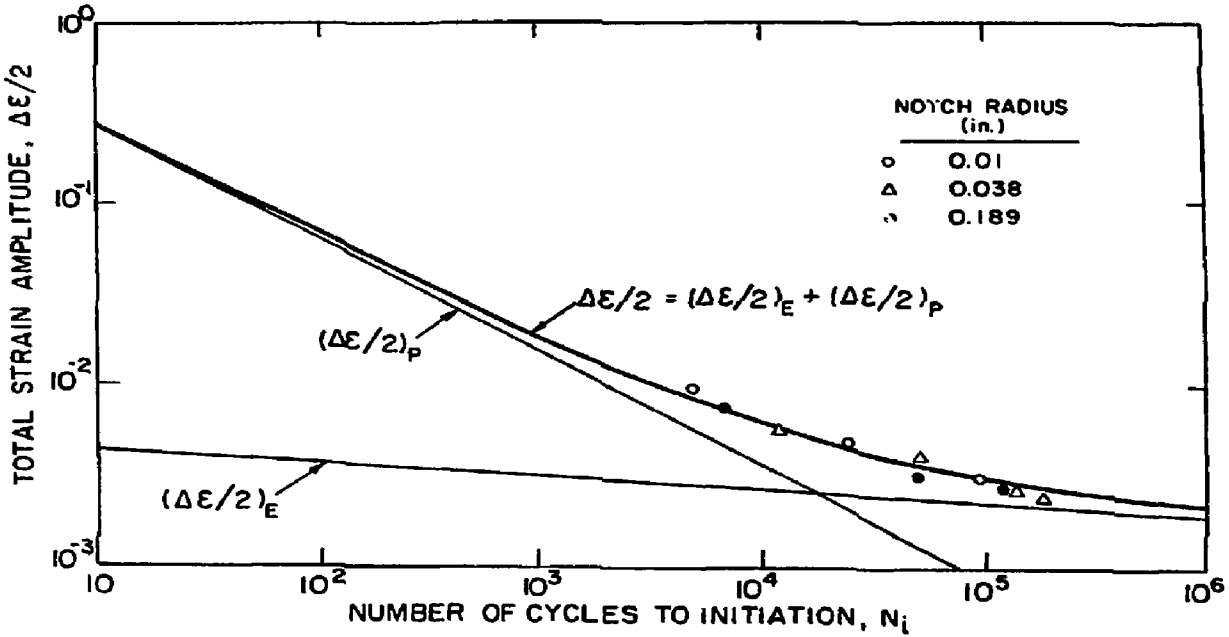

FIGURE 6.5 - Relationship between total strain amplitude and crack initiation data for 403 stainless steel.

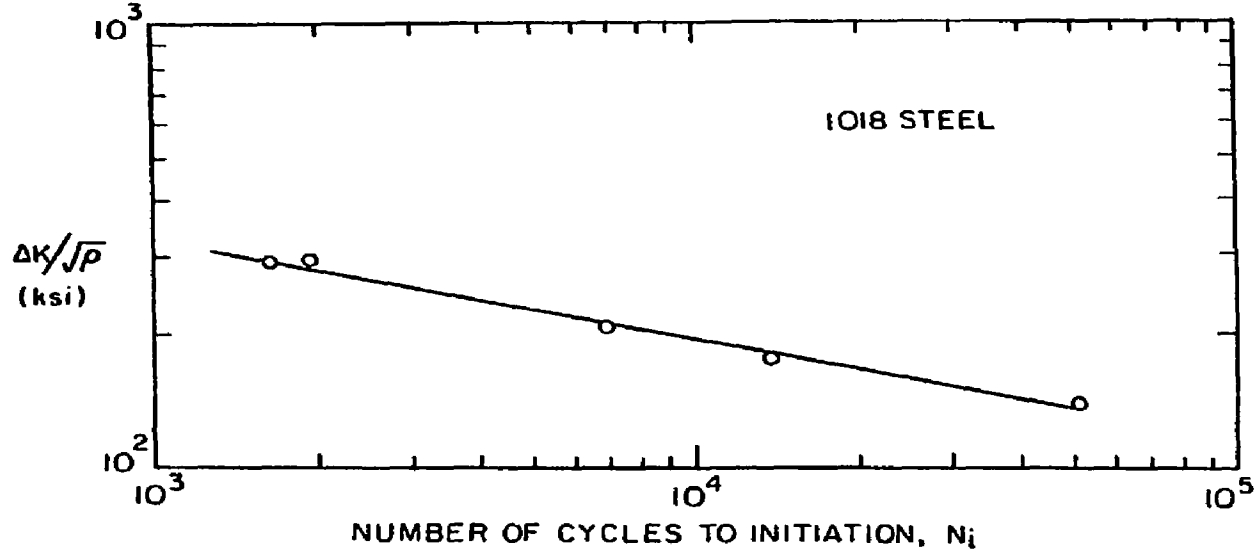

FIGURE 6.6 - Relationship between $\Delta K/\sqrt{\rho}$ and N_i for 1018 steel.

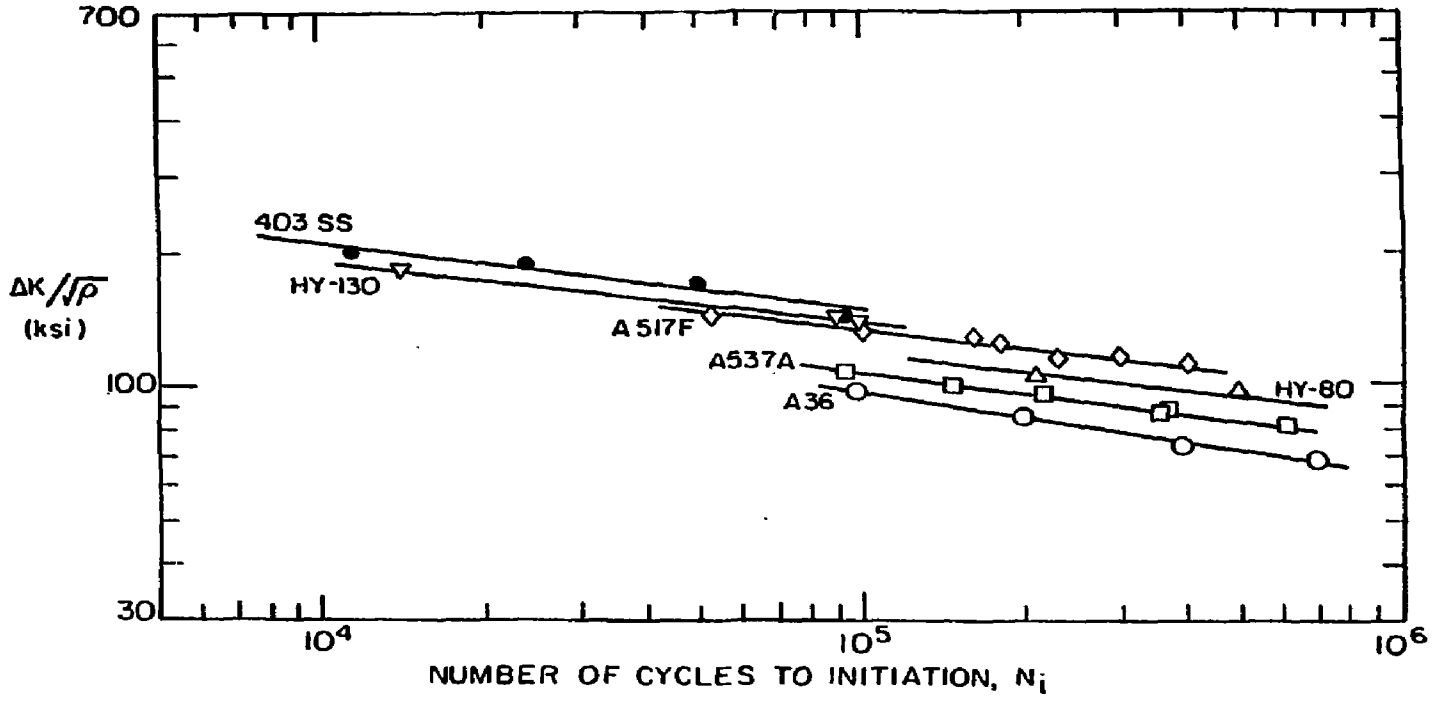

FIGURE 6.7 - Relationship between $\Delta K/\sqrt{\rho}$ and N_i for various steels. (123)

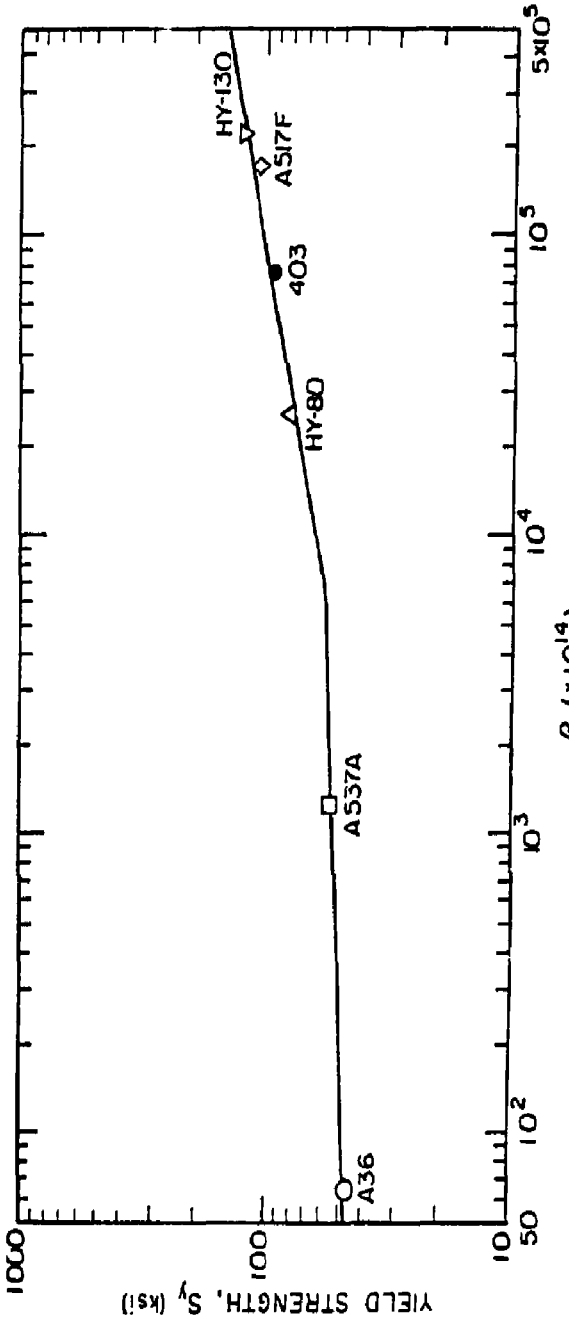

FIGURE 6.9 - Relationship between yield strength and β for various steels.

APPENDIX

K_I Calculations for Compact Tension Specimens

For a compact tension test specimen (Figure A.1), the expression for evaluating K_I is as follows:

$$K_I = \sigma\sqrt{a}\, F_1(a/b, h/b, d/h)$$

where $\sigma = P/bB$ and B is the thickness of the specimen. Or in terms of the nominal stress, we have:

$$K_I = \sigma_N \sqrt{b-a}\, F_2(a/b, h/b, d/h)$$

where

$$\sigma_N = \sigma_{N(\text{Tension})} + \sigma_{N(\text{Bending})}$$

$$\sigma_N = \frac{P}{b-a} + \frac{6P(a + \frac{b-a}{2})}{(b-a)^2}$$

After simplifying

$$\sigma_N = \frac{2P(2b+a)}{(b-a)^2}$$

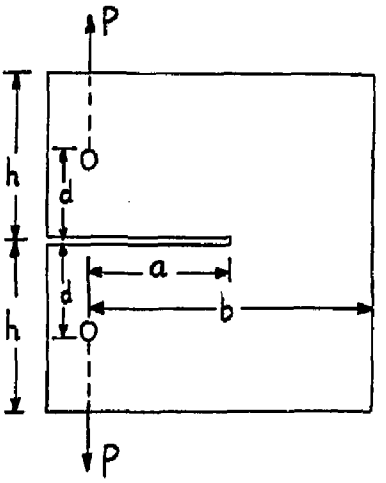

FIGURE A.1. Compact tension specimen.

Note that the relationship between F_1 and F_2 is given by the following expression

$$F_1 = \frac{2(2+a/b)}{(1-a/b)} \frac{1}{\sqrt{a/b}} F_2$$

The numerical values of F_2 have been calculated using the boundary collocation method. Figure A.2 shows the plot of F_2 vs. a/b for different specimen geometry. The accuracy of the F_2 values is about 1%. Figure A.3 shows the geometry of the standard compact tension specimen.

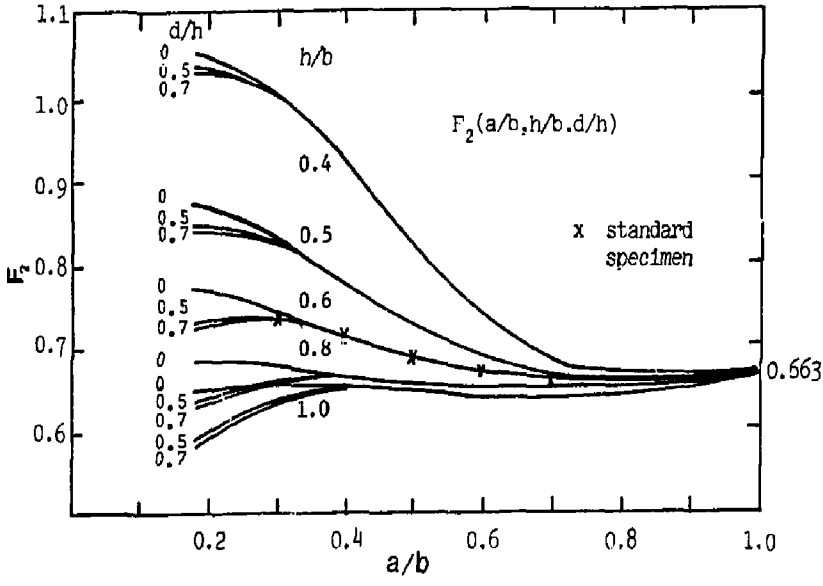

FIGURE A.2. The relationship between F_2 and a/b for different specimen geometry.

h = 0.6 b

h_1 = 0.275 b

D = 0.25 b

c = 0.25 b

(Thickness = b/2)

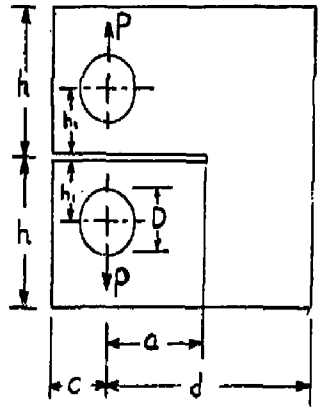

FIGURE A.3. Standard compact tension specimen.

An empirical expression can be formulated to calculate F_1 for the standard compact tension specimen. The following formula has 0.5% accuracy for $0.3 \leq a/b \leq 0.7$.

$$F_1\left(\frac{a}{b}\right) = 29.6-185.5\left(\frac{a}{b}\right)+655.7\left(\frac{a}{b}\right)^2-1017.0\left(\frac{a}{b}\right)^3+638.9\left(\frac{a}{b}\right)^4 \qquad (A.1)$$